HONEYCOMB IN HYBRID COMPOSITE ARMOR

RESISTING DYNAMIC IMPACT

By

ADVAIT BHAT

Bachelor of Science in Mechanical Engineering
University of Mumbai
Mumbai, Maharashtra, India
2007

Master of Science in Mechanical and Aerospace Engineering
Oklahoma State University
Stillwater, Oklahoma
2009

Submitted to the Faculty of the
Graduate College of the
Oklahoma State University
in partial fulfillment of
the requirements for
the Degree of
DOCTOR OF PHILOSOPHY
JULY 2015

HONEYCOMB IN HYBRID COMPOSITE ARMOR

RESISTING DYNAMIC IMPACT

Dissertation approved:

Dr. Jay C. Hanan
Dissertation Adviser

Dr. Sandip P. Harimkar

Dr. Raman P. Singh

Dr. Semra Peksoz
Outside Committee Member

ACKNOWLEDGEMENTS

I thank financial support for this work by MetCel LLC and the Helmerich Research Center through grants to the Oklahoma State University Foundation. Funding from the Oklahoma Center for Advancement and Technology - Oklahoma Applied Research Support (OCAST-OARS Award Nos. AR12.-041, AR 131-037) and the National Science Foundation (NSF Award No: 1214985) was critical for the project success. I thank my adviser Dr. Jay Hanan for his guidance and supervision during the entire span of this project. I express my deepest gratitude for his continuous motivation and patience during my academic endeavor at Oklahoma State University. I thank my outside committee member Dr. Semra Peksoz for being my mentor on body armor and familiarizing me with their design principles and prevalent test procedures. I gratefully thank Dr. Raman Singh and Dr. Sandip Harimkar for being on my dissertation committee. I extended my appreciation to the personnel from DSM Dyneema, The Safariland group, US Shooting Academy, and Leading Technology Composites for their assistance on ballistic tests. I owe individual and collective acknowledgements to all the colleagues in my research group for their support. I specially thank Balaji Jayakumar, Nathaniel Evans and Trisha Buck for their help during the ballistic tests. Last but not the least; I owe utmost gratitude and regards to my wife Lopeeta and my family for their continuous motivation and blessings.

Name: ADVAIT BHAT

Date of Degree: JULY, 2015

Title of Study: HONEYCOMB IN HYBRID COMPOSITE ARMOR RESISTING DYNAMIC IMPACT

Major Field: MECHANICAL AND AEROSPACE ENGINEERING

Abstract: Behind Armor Blunt Trauma (BABT) is an emerging problem in body armor due to excessive deformation resulting from projectile impact. A potential to reduce BABT has been identified by incorporating a honeycomb layer in a Hybrid Composite Armor (HCA). Honeycombs along with other cellular solids have been used primarily for low velocity impact absorption and in some cases for vehicle mounted armor. Their role in body armor remains unexplored and is the focus of this study. A new HCA with aluminum honeycomb was designed and evaluated using ballistic testing in compliance with the level III NIJ 0101.06 body armor standard. Performance improvement of the armor was verified from these tests using Back Face Signature (BFS) and V_{50} metrics. Effects of honeycomb attributes on ballistic performance were successfully correlated using an analytical scheme that showed good agreement with the experimental results. HCA was found to qualify for the standard, while demonstrating a maximum BFS reduction of 40.8% (and hence BABT) in comparison to a baseline of the same weight. Limitations to the use of honeycombs in armor were also identified. Performance benefits of honeycomb inclusion in armor observed experimentally were supplemented by numerically derived results from FEA in ABAQUS®. This HCA design has the highest known propensity to reduce injury both due to the light weight and improved trauma performance compared to existing designs. A selection methodology was demonstrated to further extend this advantage by inclusion of other commercially available honeycombs.

TABLE OF CONTENTS

LIST OF TABLES

Table Page

LIST OF FIGURES

Figure Page

CHAPTER 1. PROBLEM DESCRIPTION AND MOTIVATION

The science of developing structures and systems for protection against impacting projectiles is one of the oldest known to man. Evolution of these structures (shields, barriers, armors, and clothing) will continue as long as the impending threats they protect against improve in their lethality. Advancement in penetration capacity and impact velocities of projectiles renders contemporary solutions obsolete over time and new methods of protection have to be sought.

The majority of current projectile impact protection structures utilize both reversible and irreversible modes of energy conversion to maximize dissipation upon impact. Weight sensitive applications like those in the defense and aerospace sectors involve constraints that necessitate thinner, more flexible protection offering better stability with strength and ease of handling per unit mass. In such cases, an irreversible mode of conversion is predominant as it positively ensures that damages sustained through intense impact loads are minimal. The extent of irreversible energy conversion is governed by the material properties and mechanical behavior of the components in the protective system. The design geometry and structural constitution of the components in turn determine the mechanical behavior. It is thus vital to find ways to quantify and compare

each of these aspects while designing any protection system that suits a particular application. Over the past few decades, review publications have summarized the factors that affect the ballistic impact resistance of materials through combined use of experimental and numerical, analytical or micromechanical evaluation methods to gauge the performance of materials and protective system designs [1-5].

Table 1 A list of review publications summarized by Ben-Dor *et al*. [1] that highlights the materials that gained research focus for use in protection plates against ballistic impact by projectiles.

Reference	Year	Material	Publication Type
Kennedy	1976	Concrete	Survey
Backman and Goldsmith	1978	Metal, soil	Survey
Jonas and Zukas	1978	Metal, soil	Survey
Zukas	1982	Metal	Book
Brown	1986	Metal, soil, concrete	Survey
Anderson and Bodner	1988	Metal, soil	Survey
Heuzé	1989	Geological materials	Report
Recht	1990	Metal	Book
Zukas and Walters	1990	Metal, soil, concrete	Book
Abrate	1991	Composites	Survey
Abrate	1994	Composites	Survey
Dancygier and Yankelevsky	1996	Concrete	Article
Corbett *et al*.	1996	Metal, soil, concrete	Survey
Abrate	1998	Composites	Book
Teland	1998	Concrete	Report
Børvik *et al*.	1998	Metal	Report
Kasano	1999	Fiber Composites	Survey
Goldsmith	1999	Metal, soil	Survey
Cheeseman and Bogetti	2003	Fiber Composites	Survey
Phoenix and Porwal	2003	Fiber Composites	Article

It can be seen from the list presented in Table 1 that metals, fiber-based composites, and concrete-based materials dominate investigative focus on protection against ballistic projectile impact. Since most current commercially used protective systems are multilayered composite structures, research attention in the last decade has consequently adapted from a single-component single-material analysis to a simultaneous investigation

of involved materials, their behavior and inter-dependence under impact, and the cumulative effect on the overall protective performance. Cellular solids are a relatively new class of materials in the multilayered protective structures domain. Their primary use has been as cores or fillers in sandwich designs that protect against low velocity impacts [5]. Their role in high velocity impact protection applications like armor has seen limited research attention.

1.1 Research problem, hypothesis, and objectives

Behind Armor Blunt Trauma (BABT) covers a range of non-penetrating injuries to the human torso resulting from projectile impacts on personal armor. Even when the armor prevents complete penetration of the impacting projectile, the energy imparted to the armor backing and body wall can be high. This can cause serious injury to the wearer by damaging thoracic and abdominal contents behind the armor plate and even result in fatality [6]. BABT manifests itself due to stress wave transfer from the local point of impact on the armor to the underlying tissue. The rear of the armor deforms at high velocities and accelerates underlying viscera locally, which is then followed by distributed load on the thorax by movement of the whole plate. Current armor standards like the National Institute of Justice (NIJ) 0101.06 quantify this deformation in terms of Back Face Signature (BFS) measured on a Roma Plastilina® #1 clay backing. The problem of BABT is prominent in high strength fabric composite armors (classified as level III by the NIJ). Fiber volume percentage in these composites is kept high for maximum utilization of the fiber properties in projectile defeat mechanisms. The low resin content aids in pliability at relatively high thicknesses, which although this improves the wearer's mobility and comfort, it increases the BFS and chances of BABT.

This problem can be solved by coupling these composites with stiffer armor materials like ceramics and metals (hybrid armor) but not without a significant weight penalty. A new solution lies in pairing armor composites with cellular solids in a sandwich construction.

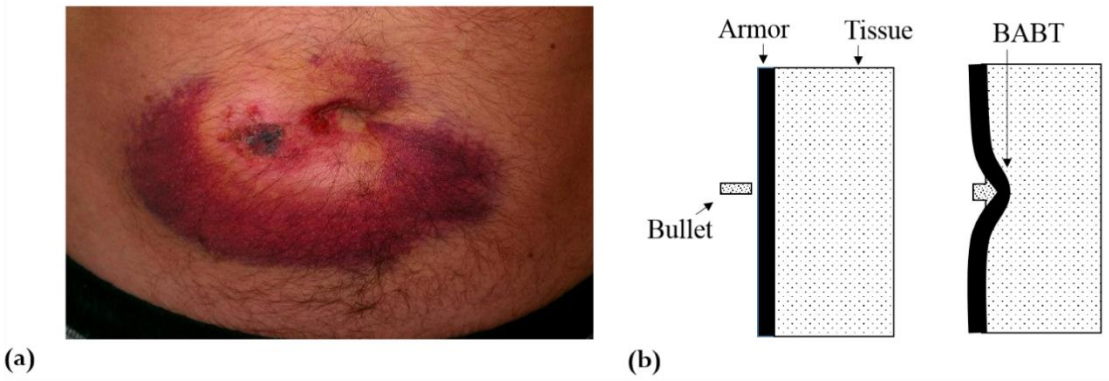

Figure 1 (a) Behind Armor Blunt Trauma[1] (b) side view schematic showing how it occurs.

Cellular solids have high specific stiffness and strength-to-weight ratio due to porosity. When used in a sandwich construction, the cellular solid layer creates a bending axis offset between the composite face layers. This increases the cumulative moment of inertia of the sandwich, thereby improving the flexural stiffness and rigidity, while keeping the weight addition to a minimum. Such a design also allows for maximum reduction in stress wave energy transfer due to acoustic impedance[2] by the cellular solid (giving gradual dissipation of shock loads). These benefits have been successfully proven by integrating aluminum-based cellular solids in vehicle mounted

[1] Image courtesy: http://co-ironwill.blogspot.com/2012/02/bullet-proof-vests.html.

[2] Acoustic impedance directly depends on density and elastic modulus difference between materials. The difference is high between contemporary armor composites and cellular solids due to porosity.

multilayered armor [7-9]. Other advantages include reduction in individual layer de-bonding, and BFS bulge velocity.

These advantages can also achieve BABT reduction in body armor—an overall research objective of the present study. This is an extension to earlier research efforts where Hybrid Composite Armor (HCA) with an amorphous metal based honeycomb was ballistic tested [10]. A *hypothesis of this research is: inclusion of a minimum thickness honeycomb in multilayered body armor improves ballistic performance compared to the same areal density armor without honeycomb. The minimum honeycomb thickness depends on the face material and material properties of the honeycomb and here will be identified for a subset of the possible material combinations.*

Objective 1: Experimental evaluation of the performance influence of honeycomb inclusion in level III body armor.

Attributes and constraints for vehicle mounted armor and body armor are markedly different. Body armors are more weight-sensitive. Tolerances on allowable areal densities of constituent materials in the armor are stringent. Similarly, thickness limitations in body armor are higher due to smaller deployment volumes available in the carrier vest pockets. Proximity of armor to the human body makes propensity of injury more likely. If enough space is allowed, deformed vehicle armor would not contact occupants. Hence, strict armor BFS limits, as stated by the NIJ body armor standard for example, may not be required in vehicle mounted armor[3]. These factors eventually affect the armor design and in turn govern the functionality of any included cellular solids. Hence, a first objective of this study is to identify the role of the honeycomb in body

[3] Refer NIJ standard 0108.01.

armor and its contribution to projectile defeat mechanisms with the imposed constraints of the NIJ standard.

This objective demonstrates a fabrication process that allows integration of honeycomb cellular solids in body armor. Ballistic performance of the aluminum honeycomb included body armor was compared with the current state-of-the-art material used in level III body armor as a baseline: Dyneema® HB50 fabric cross-ply laminate composite. This study is the first to present detailed ballistic test data for HB50, not currently available in published literature. Similarly, it is the first to verify the influence of honeycomb attributes like base material, strength, height, location in the multilayered armor on armor ballistic performance. The method used for design, testing, and obtaining data can serve as a guideline for the inclusion of other cellular solids in hybrid armor and related protective structures. The experimental investigation of the aluminum honeycomb included in HCA is presented in Chapter 3.

Objective 2: Numerical modeling of the Hybrid Composite Armor under ballistic impact.

Experimental ballistic tests and results give a macro-mechanical insight in the behavior of the HCA and its potential to reduce BABT. Evaluation of micro-mechanical data for BABT characterization through *in-situ* observation of the projectile defeat mechanism, identifying individual layer performance, and armor time dependent properties (armor rear face velocity, its acceleration and stress wave impedance) are difficult to conduct experimentally. Numerical modeling or finite element analysis (FEA) is an effective tool to address these issues. Along with corroborating and supplementing experimentally observed results, FEA allows for rapid design

modifications and to simulate multiple ballistic impact scenarios that are cost and time prohibitive to conduct experimentally.

Prior attempts to conduct FEA of high velocity ballistic impact on composite armor have seen limited success. Several deficiencies exist in the modeling of constituent materials involved in FEA. Successful completion of this objective primarily provided valuable insights on honeycomb behavior in HCA under ballistic impact. It also set a precedent in FEA methodology that can be adopted for similar research. Numerical investigation of HCA is presented in Chapter 4 and 5.

Objective 3: Selection criteria for honeycombs

No specific selection criteria has been presented for cellular solids used in multilayered armor [7-9]. This information is vital to distinguish between cellular solid parameters (base material, density and cell size) and identify those that have a significant influence on the ballistic behavior. Gibson and Ashby have presented a selection method for foam-based energy absorption structures in their text [11]. The process considers direct contact of the cellular solid with the impacting object. A similar method was also presented for flexural stiffness improvement of sandwich beams. Here, theories were adapted to develop selection criteria for honeycombs used in high velocity impact applications including HCA.

Literature pertaining to armor is often restricted. A review is presented in Chapter 2 to familiarize the reader with their basic concepts and provide more details on the scientific background leading to this thesis.

CHAPTER 2. BACKGROUND AND LITERATURE REVIEW

2.1 Review of published literature and concepts pertaining to body armor

Any impact protection application demands a specific design and material choice that will provide maximum efficiency and the desired level of safety. It demands a design selection that enables energy dissipation at a predetermined rate and controlled manner. As described by Lu *et al.* [12], the most fundamental principles that act as guidelines for designing any impact protection system can be briefly outlined as follows:

- The energy conversion by the structure should be irreversible by plastic deformation and other dissipation processes, rather than storing it elastically.
- The peak reaction force should be kept below a threshold and an ideally constant reaction force should be maintained throughout the deformation process.
- The displacement by deformation or the stroke in the structure should be sufficiently long to absorb the large amount of input energy.
- The deformation mode and energy absorption capacity of the designed structure should be stable and repeatable to ensure reliability during service.
- The structure should be as light as possible with high specific energy absorption capacity.

- Manufacturing, installation and maintenance should be easy and cost effective.

For body armor, safety of the human user is of utmost importance. Body armor designs have to provide this safety without being bulky or restricting mobility. Their close proximity to the torso requires curvature for a comfortable fit. As a result, the principles of high specific energy absorption capacity, reliability, manufacturing and handling ease gain prominence. Thickness limitations and issues like BABT restrict the maximum allowable stroke or deformation displacement.

Over the years, the need for high specific energy absorption capacity has led to the development of body armor made from high strength fabrics and ceramic materials [13]. They are lightweight and perform better than their metal predecessors. As described by Hazell [13], these materials can be further categorized as disruptors or absorbers. This classification is based on the material property that is specifically utilized to deal with the projectile kinetic energy. Disruptors function as the first impact layers of protective systems that erode the projectile in to fragments and thus disperse the energy. In order to successfully erode the projectile, disruptors are made from materials that have high strength and high hardness compared to the threat (for example: ceramics). In contrast, absorbers work by absorbing the kinetic energy through plastic deformation modes. These systems also serve as spall liners to prevent unwanted projectile fragments from penetrating and inflicting damage post impact (high strength fabric composites).

Modern body armor systems are multilayered and combine the advantages of both high strength fabric composites and ceramics. Extensive failure in ceramics due to brittle cracking can be reduced when combined with a fabric composite backing, giving increased multi-hit capability. Also, fabric composite based armor by themselves are not

efficient in defeating armor piercing threats. They need ceramic face layers to delocalize the concentrated forces. General projectile defeat mechanics utilized in modern multilayered body armor can be described as follows. Upon initiation of ballistic impact, the ceramic face layer erodes the projectile tip and absorbs some kinetic energy. Most of the structural loads during this period are sustained by the fabric composite backing. After the blunted projectile penetrates the ceramic layer (which will typically fail and fragment by reflected tensile waves), it is slowed down to a stop by the fabric composite backing via kinetic energy absorption through plastic deformation modes. A portion of the structural loads and kinetic energy in this stage is then transferred to the wearers' body wall as the composite backing deforms.

Ultimately, parameters for body armor designs (material choice and areal density for example) are based on the performance requirements set by the threat specific body armor standards. The most commonly used standards are from the National Institute of Justice (NIJ), MIL specifications, and similar European designations (DIN, CEN, and STANAG).

2.1.1 Contemporary materials used in body armor applications

2.1.1.1 High strength fabrics used in body armor

The first fabrics introduced in armor applications were Nylon based which were used in Flak vests designed to protect against shrapnel [14]. The invention of Kevlar in 1969, by DuPont, lead to the first patented use of fabrics in body armor as a protection against bullet threats (K-15 vests) [15]. Since then, several other fabrics have been introduced for commercial use in armor similar to Kevlar in woven and non-woven form. Namely: Aramids like Twaron, Gold Flex, and Zylon; and Ultra High Molecular Weight Poly

Ethylenes (UHMWPE) like Spectra and Dyneema. Other similar fibers as listed by Machalaba *et al.* [16] are Terlon, SVM, Armos, and Technora. The high fiber tenacity exhibited by these materials was used to improve in-plane properties of woven and non-woven composite laminates or fabric bundles.

Table 2 Comparison of mechanical properties of fabrics used in body armor [17-18].

Material	Density (g/cc)	Modulus (GPa)	Tensile Strength (GPa)	Failure Strain (%)
Generic properties				
Aramid	1.39-1.44	60-115	2.8-3.2	1.5-4.5
HWMPE	0.97-0.98	90-140	2.8-4.0	2.9-3.8
LCP	1.40-1.42	64-66	2.7-2.9	3.3-3.5
PBO	1.54-1.56	270-290	5.4-5.6	2.4-2.6
PIPD	1.69-1.71	320-340	3.9-4.1	1.1-1.3
Specific properties				
1500 den Kevlar 29	1.39-1.44	74	2.90	3.38
1140 den Kevlar 49		120	3.04	1.20
840 den Kevlar 129		99	3.24	3.25
850 den Kevlar KM2		74	3.34	3.80
Spectra 1000	0.97	120	2.57	3.50
E-Glass	2.47-2.67	74	3.50	4.70
S-Glass	2.47-2.49	87	4.65	5.3-5.5
Nylon	1.07-1.17	10	0.91	1.5-2.5
Twaron	1.44	80	2.8	3.3
Dyneema	0.96	172	3.1	4.5
Carbon Fiber-IM7	1.8	304	6.1	1.9

Fabric based body armor functions well against deformable threats by distributing the kinetic energy through the high strength fibers with dissipation modes including fiber shear or fracture, fiber tensile failure, or straining and associated delamination or pullout [19]. Other factors that affect their ballistic performance have also been discussed in the overview presented by Cheeseman *et al.* [20]. The ballistic performance of these composites is quantified with respect to their ability to: (a) absorb the projectile's kinetic

energy locally; and (b) spread out the absorbed energy fast before local conditions for the failure are met [21-22]. Energy absorption capacity per unit mass (E_{sp}) of armor is directly proportional to failure stress (σ_{fail}) and strain (ε_{fail}) and inversely proportional to density (ρ). Mathematically, it is expressed as:

$$E_{sp} = \frac{0.5\ \sigma_{fail}\varepsilon_{fail}}{\rho} \tag{2.1}$$

Also, the ability to spread out the absorbed energy is directly proportional to the speed of sound in the material and in turn to the material stiffness (E) and inversely to its density (ρ).

$$v_{sound} = \left(\frac{E}{\rho}\right)^{1/2} \tag{2.2}$$

Hence, the fibers used in the composite are required to have high specific tenacity, rupture strain, and in-plane stiffness to achieve maximum performance. A comparison of ballistic grade fibers using these material property values (Table 2) suggests UHMWPE is the best material. Fine fiber diameter UHMWPE laid in [0°/45°] or [0°/90°] cross-ply layups of unidirectional plies provides a high number of yarn crossover points that facilitate stress dissipation by transverse waves in primary yarns, improving ballistic performance. The layup also provides orthotropic properties to the laminate. UHMWPE further benefits from the lack of kinks typically observed in woven fabrics that lead to stress reflections and yarn failure.

Commercial brands of UHMWPE are Dyneema® by DSM Dyneema and Spectra Shield® by Honeywell. Mechanical energy absorption capacity and the tensile strength of Dyneema is higher than Spectra Shield [23-24]. Ballistic test data for hard laminate

variants of Dyneema available in the public domain are shown in Table 3. Since different types of projectiles have been used to test armor of different densities while carrying out V_{50} evaluations, an effective performance comparison can be achieved by calculating the Specific Energy Absorbed (SEA) for each Dyneema type. SEA (J m^2/kg) is the ratio of the kinetic energy corresponding to the V_{50} velocity with the laminate areal density. Comparison of SEA values presented in Table 3 indicates Dyneema HB50 has the highest propensity to defeat small arms threats. HB50 is a $[0°/90°]_s$ cross-ply hard laminate fabricated by hot pressing monolayer plies. Each ply has 82% volume fraction of gel spun SK76 Dyneema fibers mated with a styrene-isoprene-styrene triblock copolymer matrix known commercially as Kraton®.

Table 3 Ballistic test data for hard laminate variants of Dyneema®.

Dyneema type	Projectile	V_{50} (m/s)	Areal Density (kg/m^2)	SEA (Jm^2/kg)	Reference
HB2	7.62 NATO ball	885	17	223	[22]
	AK47 steel core	769	17	140	
HB2	AK47 steel core	848	19	153	[25]
HB25	AK47 steel core	878	19	164	
HB2	7.62 NATO ball	920	17	241	[26]
	AK47 steel core	773	17	141	
HB50	7.62 NATO ball	1010	16	309	
	AK47 steel core	830	16	172	

Again, the performance of ballistic fabrics against non-deformable material projectiles (armor piercing) is limited since the concentration of force over a small area causes penetration. Attempts to retain the flexibility and strength of these fabric systems along with high deformation capability of disruptors have been made. Inter-laminar strength of fabric laminates have been improved using 3D weave patterns instead of conventional 2D weaves, resulting in better ballistic performance [27]. Impregnation of

woven Kevlar fabrics with colloidal shear thickening fluid have also been used as a method of improving strength of ballistic fabrics without affecting their flexibility [28].

2.1.1.2 Ceramics used in body armor

Ceramics are the class of materials most resistant to compressive stresses. They have been increasingly used in armor applications [29-32]. They show high compressive hardness and high stiffness with low bulk density compared to metals like steels, titanium, and aluminum alloys. These properties make ceramics an excellent choice as disruptors against armor piercing projectiles. The most common non transparent ceramics for armor are tungsten carbide (WC), silicon carbide (SiC), silicon nitride (Si_3N_4), boron carbide (B_4C), titanium diboride (TiB_2), and alumina (Al_2O_3).

As summarized in [13, 33], the choice of a ceramic material for a specific armor application is usually based on performance to cost appraisal. SiC and B_4C are harder materials with lower densities than alumina but cost more. However, their ability to defeat more tenacious threats with lower weight penalties results in their favor. Si_3N_4 and alumina have similar performance, but the higher availability of alumina gives it a reduced cost. TiB_2 is a high performing ceramic but is one of the most expensive ceramics due to processing limitations. WC, owing to its high mass is primarily used in projectile cores instead of armor. The mode of manufacture is essentially what dictates the properties of the final ceramic product (density, hardness, grain size, amount of minor phase, phase stability, fracture mode ─ all of which in turn affect performance) and also determines its end cost [33]. Performance was also found to vary with different manufacturers who may utilize the same manufacturing process [13]. A comparison of ceramic armor plates is illustrated in Table 4. This comparison is based on their

calculated Mass Efficiency Factor (E_m) which represents the factor by which the areal density of the Rolled Homogenous Armor witness material (of thickness t_c) has to be multiplied to provide the same protection. In brief, higher E_m represents better performance.

Table 4 Comparison of Ceramic armor materials against Level IV 7.62 mm x 51 mm FFV AP (WC – Co core) threat [13].

Ceramic	Manufacturer	t_c (mm)	Calculated E_m	Witness Material
HP SiC	Ceradyne Inc.	6.5	5.0	Al 6082-T651 YS = 250 MPa Depth of penetration: 75 mm without ceramic.
HP B_4C		6.5	2.5	
RS Si_3N_4		6.5	2.2	
HP TiB_2		6.6	3.4	
Sintered SiC	Morgan AM&T	5.9	3.7	
Sintered SiC	Wacker-Chemie	6.1	4.8	
LPS SiC	AME	6.1	3.3	
RB SiC	Morgan AM&T	7.2	1.3	
RB SIC	Haldenwanger	6.2	1.2	
RB SiC	Schunk	6.0	1.5	
RB B_4C	M-Cubed	7.0	1.2	

HP: Hot Pressed, RB: Reaction Bonded, RS: Reaction Sintered, LPS: Liquid Phase Sintered

2.1.2 Multilayered armor and the use of cellular solids

Stress waves tend to lose energy when they encounter materials of different mechanical properties. This is due to acoustic impedance which directly depends on density and elastic modulus of the material. Hence, most modern armors tend to be multilayered armor systems (hybrid composite/integral armors) with ceramics and high strength fiber composites forming their adhesively bonded layered components. The choice of materials suitable for armor relies on factors like permissible areal density, multi-hit capability, impact velocity, and the maximum allowable BFS for the expected projectile threat. The order of layering of these materials and their chosen areal densities

are optimized to maximize the energy absorption capacity of the armor system during each stage of the projectile impact with consideration of wave propagation effects.

Mahfuz *et al*. [34] investigated the stress distributions and damage modes in an integral armor concept to conclude that the structural integrity of multilayered armors depended extensively on inter-laminar shear stresses between individual layers. The study showed stress wave reflections at interfaces caused complete delamination of ceramic and composite layers on impact. In-plane stresses combined with high compressive through-thickness stress resulted in severe damage to the ceramic layer. A way to prevent complete delamination of layers could be to increase inter-laminar bond strength by use of more adhesive. The effect of adhesive and its thickness on ballistic performance of armor has been investigated [35]. The study showed that although a thicker adhesive layer helped in widening the area of plastic deformation in the backing (thus absorbing more kinetic energy), it exacerbated the damage in the ceramic layer due to stress wave reflection. It recommended the thickness of the adhesive layer should be reduced as far as possible so as to delay ceramic fragmentation. Another way to minimize inter-laminar stresses at the ceramic-composite interface is by increasing the obliquity of the projectile impact [36]. An oblique impact causes increased area of contact between the projectile and the ceramic as well as offers a higher ceramic thickness in the projectile path. It results in higher erosion of the projectile improving the ballistic performance. The mechanism of ceramic face obliquity to improve ballistic performance has been used in armor design as early as 1984 [37]. Individual layer areal density in the integral armor system is the most critical factor governing the ballistic performance of the unit. Grujicic *et al.* [38] confirmed that the ratio of composite

backing to facing ceramic areal densities for a fixed overall density was a critical design parameter. Results from the study showed that there is an optimal composite areal density at which the ballistic performance of the unit peaks. Any further increase in composite areal density for the same total areal density of the unit adversely affected its performance.

Collapsible energy absorbers like honeycombs and foams have also been incorporated in armor systems to improve energy dissipation and attenuation of stress wave propagation. The use of such porous/cellular solid materials can be particularly effective as they allow maximum acoustic impedance due to their high elastic modulus difference compared to contemporary armor materials. Also, their gradual cell collapse allows designers to control the rate of deformation via regulation of the geometric parameters of the material.

The impact absorbing armor design by Dunn in 1994 is likely the first published reference to use of honeycombs in multilayered armors [7]. The honeycomb layer was used as a spacer between layers to improve the ballistic performance of the unit. Its function was to minimize energy transfer and the propagation of stress waves that prematurely failed successive armor layers upon impact. This thereby isolated these successive layers from initial stages of impact and helped in gradual dissipation of shock. In process, the honeycomb also helped in absorbing some portion of the kinetic energy. A study by Senf *et al.* [8] showed that aluminum honeycomb helped in reducing back face bulging in a multilayered armor. Results also showed the honeycomb assisted in reducing the bulging velocity. This decrease in bulging velocity was found to be proportional to the increase in the honeycomb layer thickness. Benefits of the

honeycomb were found to be more prominent against deformable projectiles than armor piercing ones. Alavi Nia *et al.* [39] concluded ballistic performance of honeycombs can be improved by increasing the panel thickness and the cell wall thickness or by reducing the cell size. This way, energy dissipation through cell wall folding and shearing can be increased. A summary of research efforts to incorporate aluminum foams as a constituent material in integral armors has been presented in a review by David *et al.* [9]. The review states that aluminum foams attenuated stress waves of ballistic impact by undergoing densification under dynamic nonlinear deformation. The time lapse for complete densification corresponds to the time delay in stress transfer to the backing layer. Armors with foam layers were found to perform better than baselines without foam of the same areal densities. Apart from acting as a stress wave filter, the foam also helped to reduce individual layer debonding and back face bulging. Other significant developments pertaining to body armor, similar to those discussed in this section, have also been summarized in this review.

2.1.3 Finite Element Analysis (FEA) of armor ballistic tests

The study of energy absorption modes and failure patterns observed in armor first prompted the use of numerical codes that could predict their ballistic performance. Similar to analytical modeling of an impact problem, FEA codes can also be used to combine the various energy dissipation modes in one analysis and predict the ballistic resistance and impact worthiness of armor. This method is far more effective than actual testing, as making variations in design is easy and time effective. Failure modes and deformations from FEA also can be visually inspected to compare accuracy with

experimental results. This comparison is a necessary validation step as accuracy of results from FEA is variable since there are no standards to the way FEA is conducted.

The Material model selection and assigned property values govern the nature of the final output result. Evolution in simulation codes and material failure models has improved the efficiency of FEA, leading up to the development of commercial simulation codes and software options (LS DYNA®, AUTODYN®, ABAQUS®) to carry out the numerical investigations. Errors in model selection and assigned properties reflect in incorrect visual and numerical response from the simulations. Property assignment for any material can be segregated into four basic inputs: (a) elastic property inputs, (b) plastic property inputs, (c) damage initiation input, and (d) damage evolution inputs. Each input conforms to the desired material model that best represents the actual material behavior when under impact. The following sub-sections will categorize references according to the primary materials involved in armor FEA and discusses material models.

2.1.3.1 Material modeling of metals in armor FEA

In the earliest FEA attempts, simple material models were used to model the material properties of metal objects undergoing impact. Energy conservation equations and dimensional analysis were the primary modes for evaluation which were later replaced by specific numerical models. Elastic modulus, density, plastic stress-strain relationship, shear, and tensile limits were considered as relevant material inputs. However, the material in its entire sense was not considered, as strain rate dependent and adiabatic effects were largely excluded. To incorporate strain rate effects and adiabatic heating, a material model by Johnson and Cook was proposed in 1983 [40]. The model was an extension of the Von Mises criteria where in the flow stress was defined by:

$$\sigma_{eq} = [A + B\varepsilon^{n}][1 + C\varepsilon^{\cdot *}][1 - T^{*m}] \quad (2.3)$$

where *A, B, C, n* and *m* are material constants, $T^{*m} = (T - T_0)/(T_m - T_0)$ is the homologous temperature, where T_0 is the room temperature and T_m is the melting temperature. ε is the strain, and $\varepsilon^{\cdot *} = \varepsilon^{\cdot}/\varepsilon^{\cdot}_0$ is a dimensionless strain-rate given by the ratio of instantaneous strain rate $\varepsilon^{\cdot}$ and a user-defined reference strain-rate $\varepsilon^{\cdot}_0$. Chamacho *et al*. [41] then modified the strain-rate sensitivity term in the above equation to avoid unwanted effects if $p^{\cdot} * < 1$. The modified version of the Johnson–Cook model can be written as:

$$\sigma_{eq} = [A + B\varepsilon^{n}][1 + \varepsilon^{\cdot *}]^{C}[1 - T^{*m}] \quad (2.4)$$

In 1985, a fracture model was proposed by Johnson and Cook which estimated the failure strain (ε_f) for materials under different stress states, strain rate and temperature [42]. The model equation was a five parameter based expression given by:

$$\varepsilon_f = [D_1 + D_2 exp(D_3\sigma^*)][1 + \varepsilon^{\cdot *}]^{D_4}[1 + D_5 T^*] \quad (2.5)$$

where the stress triaxiality ratio is defined as $\sigma^* = \sigma_H/\sigma_{eq}$, σ_H being the hydrostatic stress, σ_{eq} being the total equivalent stress and D_1 to D_5 are material constants. A combination of these two equations can predict the onset and evolution of plasticity with failure initiation in a variety of metals.

Steels, aluminum alloys, lead, and copper or brass are the most often encountered metals in numerical analysis of armors. Tool steel and lead are the constituents of the bullet projectile core while the outer gliding jacket is copper or brass. Other metals are typically found in the target plates. A range of Johnson-Cook material parameters have been chosen by research groups for modeling the steel core, lead, and the gliding jacket

[43-52]. A summary of these parameters is presented in Table 5. The stress versus strain plots derived from the Johnson-Cook strength model (equation 2.3) parameters for the steel core are shown in Figure 2. It highlights the significant variations in material properties used by research groups for numerically simulating the same type of 7.62 APM2 bullet core. This makes the numerically obtained results subjective to the chosen inputs. As pointed out by Kilic and Ekici [52], material data for the bullet materials is generally not disclosed in literature and the process to experimentally evaluate it from actual rounds is difficult. Most research groups get around this problem by considering APM2 ammunition as a rigid body. This, however, is not a realistic assumption against hard targets as core fracture is excluded leading to higher penetration depths. It is also not possible to neglect the lead filler and the jacket material as it has a proven influence on the penetration capacity of the bullet [53].

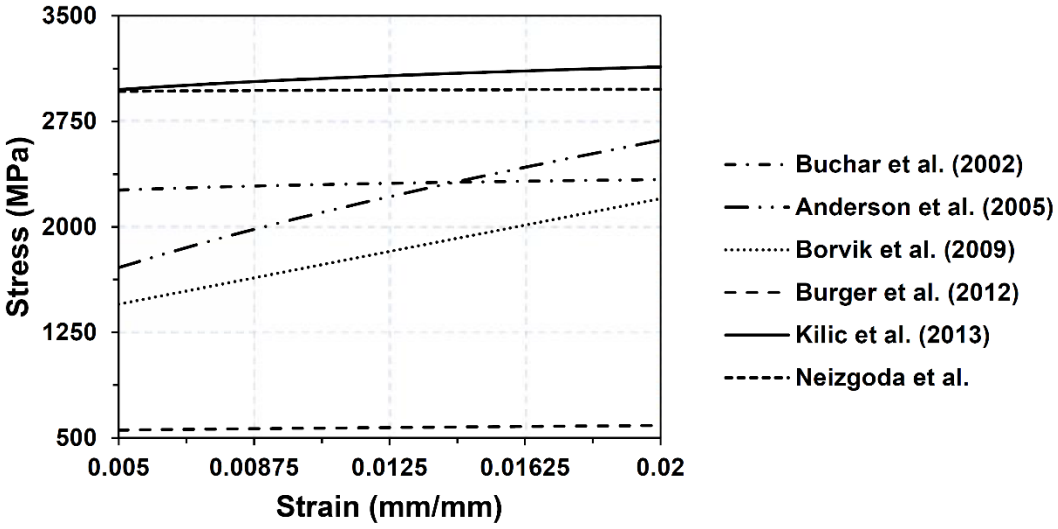

Figure 2 Stress - Strain plots for steel core derived from Johnson-Cook strength model parameters used by research groups in armor FEA.

Table 5 Material parameters of metal constituents of bullets used in armor FEA

	Elastic		Johnson-Cook strength model									Johnson-Cook fracture model						EOS		
	Modulus E, (GPa)	Poisson's ratio, ν	A (MPa)	B (MPa)	β	*C*	m	n	ε'_0 (/s)	T_{melt} (K)	T_{ref} (K)	D1	D2	D3	D4	D5	εf	Bulk speed, C_0 (km/s)	S	Γ_0
Material parameters for steel core																				
Kilic, Ekici [52]	-	-	1900	1100	0.579	0.05	1	0.3	0.001	-	-	-	-	-	-	-	2-3%	4.57	1.49	1.93
Niezgoda *et al.* [49]	-	-	2700	211	0.078	0.005	1.17	0.065	-	-	-	0.4	0	0	0	0	-	4.57	1.49	1.93
Burger *et al.* [51]	200	0.33	490	807	1.647	0.012	0.94	0.73	0.0005	1800	300	0.071	1732	-0.54	-0.012	0	-	-	-	-
Borvik *et al.* [48]	210	0.33	1200	50000	41.67	0	1	1	0.0005	1800	293	-	-	-	-	-	2%	-	-	-
Anderson *et al.*[46]	210	0.29	1034	18095	17.5	0.005	1	0.64	1	1790	300	-	-	-	-	-	10%	4.5	-	-
Buchar *et al.*[44]	-	-	1650	807	0.489	0.008	1	0.1	-	-	-	0.051	0.018	-2.44	0.0001	0.55	-	-	-	-
Material parameters for gliding jacket																				
Burger *et al.* [51]	124	0.34	440	150	0.341	0.025	1.09	0.31	1	1357	300	0.3	0.28	-3.03	0.014	1.12	-	-	-	-
Hazell *et al.*[47]	-	-	575	0	0	0	1.09	1	-	1323	-	-	-	-	-	-	5%	3.94	1.49	2.02
Borvik *et al.[48]*	115	0.31	206	505	2.45	0.01	1.68	0.42	0.0005	1189	293	-	-	-	-	-	-	-	-	-
Anderson *et al.* [46]	140	0.35	500	0	0	0.025	1	1	-	1360	300	-	-	-	-	-	-	3.94	-	-
Preece, Berg [45]	120	0.33	70	-	-	-	-	-	-	-	-	-	-	-	-	-	-	3.94	1.49	1.99
Material parameters for lead core																				
Krishnan *et al.*[50]	17	0.4	8	-	-	-	1	-	-	-	-	-	-	-	-	-	-	-	-	-
Hazell *et al.*[47]	-	-	40	0	0	0	1	1	-	525	-	-	-	-	-	-	20%	2.006	1.43	-
Borvik *et al.* [48]	1	0.42	24	300	12.5	0.1	1	1	0.0005	760	293	-	-	-	-	-	-	-	-	-
Anderson *et al.*[46]	-	0.44	27.6	3036	110	0.116	0.00116	0.52	-	760	300	-	-	-	-	-	-	2.05	-	-
Preece, Berg [45]	16	0.44	5	-	-	-	-	-	-	-	-	-	-	-	-	-	-	2.051	1.46	2.77

Similarly, material modeling of the 7.62 mm lead core round has proven to be a difficult task for the scientific community. A wide range of values have been chosen with minimal effort dedicated to verification through mechanical testing. This is evident from the data in Table 5. Lead is a relatively soft metal that behaves fluid-like at high strain rates. The high density, low modulus of lead results in low wave velocities whose magnitude during high speed impacts can be even lower than the deformation progression velocities. This manifests in FEA as excessive contact overclosures, mesh distortions from unresolved large deformations, and unrealistic strains leading to premature failure of the Lagrangian scheme. Adaptive meshing (described by Camacho and Ortiz [41]) was used by Borvik *et al.* [48] to tackle this problem. The authors observed limited success on its implementation. Attempts were made to use Arbitrary Lagrangian Eulerian integration codes in GRALE software to model fluidity of the lead core. It was found that even this method did not give a good description of the perforation process as global target deformation was too large. The authors also point out that similar difficulties were faced by Schwer [54] with a Smooth Particle Hydrodynamics approach for modeling lead cores. Owing to these difficulties, the majority of the scientific community preferred numerical analysis of APM2 rounds instead [55].

The Mie-Grüneisen Equation of State (EOS) model that defines the pressure-volume relationship depending on whether the material is compressed or expanded has also been used in conjunction with the Johnson-Cook model [45, 47, 49, 52, 55]. This model has been used in it linear and non-linear forms to provide a hydrodynamic governing model for a material's volumetric strength. In the linear form, the shock velocity U_s and particle velocity U_p are related by the expression:

$$U_s = c_0 + sU_p \tag{2.6}$$

where, c_0 is the bulk sound speed and s is the slope of the U_s - U_p curve. This expression can be further represented in a Hugoniot form as:

$$P = \frac{\rho_0 c_0^2 \eta}{(1-s\,\eta)^2}\left(1 - \frac{\Gamma_0\,\eta}{2}\right) + \Gamma_0 \rho_0 E_m \tag{2.7}$$

where, P is the pressure, ρ_0 is reference density, Γ_0 is material Grüneisen constant, E_m is internal energy per unit mass and η is the nominal volumetric compressive stress. A summary of these parameters is presented in Table 5.

Material models need to be robust to capture effects like fragmentation, petal and plug formation, stripping of the gliding jacket along with core bulging, and fractures that occur during ballistic impact. Numerical modeling has been close in predicting gross performance like penetration depths and ballistic limits. However, it has not been able to perfectly replicate all abovementioned ballistic impact effects. A part of making the models robust would be to use precise material parameters. The process of evaluating these material parameters is extensive [40]. Few research groups have tried to obtain their values using material taken from actual bullets or by fabricating test samples [43-44, 56-57].

2.1.3.2 Material modeling of ceramics in armor FEA

Ceramics are brittle materials that exhibit a high compressive strength, but poor tensile behavior. Ceramics are known to show pressure-hardening ability and this response is typically non-linear. Hence, a polynomial expression relating the pressure and strain response is more appropriate for ceramics [13].

$$P = K_1\mu + K_2\mu^2 + K_3\mu^3 \tag{2.8}$$

where, P is the pressure and μ is the volumetric strain. Johnson and Holmquist developed a model to for simulating dynamic impact response of ceramics considering this pressure-hardening law [58]. Similar to metals, a scalar damage parameter D is used to regulate failure based on accumulated plastic strains. As damage initiates, an additional pressure term is added to account for dilation or bulking and its value is calculated by energy considerations. Johnson and Holmquist proposed two variants of the model (JH-1 and JH-2). JH-1 has an instantaneous transition from intact strength curve to the failed strength curve, for the ceramic when it fails. While, JH-2 allows for a more gradual change in strength response as failure progresses. The P-μ relationship for the JH-2 model is given by:

$$P = K_1\mu + K_2\mu^2 + K_3\mu^3 + \Delta P \qquad \text{if } \mu \geq 0 \text{ (compression)} \tag{2.9A}$$

$$P = K_1\mu \quad \text{if } \mu \leq 0 \text{ (tension)} \tag{2.9B}$$

The strength of the material is expressed in terms of the normalized von Mises equivalent stress as:

$$\sigma^* = \sigma_i^* - D(\sigma_i^* - \sigma_f^*) \tag{2.10}$$

$$\sigma_i^* = A(P^* + T^*)^N (1 + C \ln p^{\cdot *}) \tag{2.10A}$$

$$\sigma_f^* = B(P^*)^M (1 + C \ln p^{\cdot *}) \tag{2.10B}$$

where, σ_i^* is the normalized intact equivalent stress and σ_f^* is the normalized fractured equivalent stress. Stress normalizations are done using the stress at the Hugoniot Elastic Limit (HEL). P^* is the normalized actual pressure and T^* is the normalized maximum

tensile hydrostatic pressure the material can withstand. Again, pressure normalizations are done using the pressure at the HEL. *A*,*B*,*C*,*M* and *N* are material constants. The JH-2 model can account for strain rate effects similar to the Johnson-Cook model using a $p^{\cdot *}$ term. Plastic strain required to estimate the scalar damage parameter, *D*, for simulating failure is calculated by:

$$\varepsilon_f = D_1(P^* + T^*)^{D2} \tag{2.11}$$

where, D_1 and D_2 are material constants.

Table 6 Summary of JH-2 parameters from published literature for ceramics [59].

	B_4C	**SiC**	**AlN**	**Al_2O_3**	**Glass**
Density (kg/m^3)	2510	3163	3226	3700	2530
Shear modulus (GPa)	197	183	127	90.16	30.4
Strength Constants					
A	0.927	0.96	0.85	0.93	0.93
B	0.7	0.35	0.31	0.31	0.088
C	0.005	0	0.013	0	0.003
M	0.85	1	0.21	0.6	0.77
N	0.67	0.65	0.29	0.6	0.77
$p^{\cdot *}$	1	1	1	1	1
Tensile strength (GPa)	0.26	0.37	0.32	0.2	0.15
Normalized fracture strength	0.2	0.8	-	-	0.5
HEL (GPa)	19	14.567	9	2.79	5.95
HEL Pressure (GPa)	8.71	5.9	5	1.46	2.92
HEL Volumetric Strain	0.0408	-	0.0242	0.01117	-
HEL Strength (GPa)	15.4	13	6	2	4.5
Damage Constants					
D_1	0.001	0.48	0.02	0.005	0.053
D_2	0.5	0.48	1.85	1	0.85
Equation of State					
Bulk Modulus, K_1 (GPa)	233	204.785	201	130.95	45.4
K_2 (GPa)	-593	0	260	0	-138
K_3 (GPa)	2800	0	0	0	290
Beta	1	1	1	1	1

A summary of JH-2 parameters from published literature for alumina (Al_2O_3), boron carbide (B_4C), silicon carbide (SiC), and aluminum nitride (AlN) have been presented [59]. They are listed in Table 6. Similar to metals, evaluating material parameters for ceramics is complicated since many cannot be determined directly and have to be inferred. The JH-2 model is able to balance accurate representations of the physical phenomenon while maintaining computational efficiency. Validation tests of the model by Johnson and Holmquist showed a correct prediction of the final-buckling pressure and the stress-pressure history. However, phase changes at elevated pressures may not be adequately described by the model.

2.1.3.3 Material modeling of composites in armor FEA

Composites exhibit anisotropy in mechanical properties, meaning their values are directionally dependent. The stress-strain relationship in this case will be represented by a thirty six constant second-order stiffness tensor. Based on the inherent symmetry the material may possess, fewer constants can generally describe this relationship (orthotropic materials require only nine constants). A detailed explanation on the mechanics of composites is available [60]. The damage in laminated composites results from matrix cracking, fiber-matrix debonding, fiber fracture and delamination. The onset of damage causes a reduction in load carrying capacity of the plies and numerically this is computed by estimating the corresponding reduction of the stiffness matrix components. Classical laminate analysis can then calculate the overall resulting mechanical properties of the laminate, post stiffness reduction.

Ballistic impact on layered composite armor involves a three-dimensional stress state which needs failure prediction models that can capture both in-plane and inter-laminar

stress components. These models also need to allow for interaction of various damage modes to act simultaneously to closely resemble the actual event. Failure modeling is done on a ply to ply basis when the objective is to predict the failure behavior of the entire laminate. Failure is assumed to initiate when any of the stress components for the ply equal or exceed the nominal values. This is therefore a direct comparison between normal stress components (σ_1, σ_2, σ_3) with ply normal strengths (*X*, *Y*, *Z*) in tension (subscript *T*) or compression (subscript *C*) along the (1,2,3) directions. Similarly, shear stress components (σ_4, σ_5, σ_6) are compared with ply shear strengths (*R*, *S*, *T*) in the (23, 13, 12) planes (subscript: longitudinal *L*, transverse *T*), respectively. Typically, when a failure criterion is met, stiffness reduction within a ply is done point wise ensuring gradual degradation of properties. Composite failure models are tensor polynomial criteria involving these normal and shear stress comparison terms. Most models use: the maximum stress criterion, the Tsai-Hill criterion, the Tsai-Wu criterion, the Azzi-Tsai-Hill criterion, or the Hoffman's criterion (detailed theory and expressions available in [60]). These criteria essentially predict failure initiation without regard to the failure mode. Hashin put forth a criterion that had the ability to predict failure modes as well [61]. Four failure modes are considered in this criterion: tensile and compressive failure of the fibers and matrix. Failure is controlled by a quadratic interaction between stress components in the tensor polynomial for each mode.

As mentioned in [62], Hashin criteria does not consider a delamination mode of failure and can be supplemented with the Hou criterion [63] to include this mode in the analysis. Authors of [62] consider Hashin and Hou criterion as a three-dimensional version of the Chang-Chang model [64], which has also been used for failure prediction

in composites. Hashin's criteria has also been used in combination with Puck's criteria for simulating matrix failure [65]. Puck's criterion is based on the assumption that fracture occurs only on fracture planes inclined at a fixed angle to the material plane. The normal and shear stresses acting on this plane are calculated by stress tensor rotation from the material co-ordinate system to the fracture plane system.

Table 7 Polynomial expressions of Hashin and Hou criteria [62].

Failure mode	Hashin criterion	Hou criterion	
Fiber tension	$d_{ft}{}^2 = \left(\frac{\sigma_{11}}{X_T}\right)^2 + \left(\frac{\sigma_{12}{}^2 + \sigma_{13}{}^2}{S_L{}^2}\right)$	$d_f{}^2 = \left(\frac{\sigma_{11}}{X_T}\right)^2 + \left(\frac{\sigma_{12}{}^2 + \sigma_{13}{}^2}{S_L{}^2}\right)$	(2.12A)
Fiber compression	$d_{fc}{}^2 = \left(\frac{\sigma_{11}}{X_C}\right)$		(2.12B)
Matrix cracking	$d_{mt}{}^2 = \left(\frac{\sigma_{22} + \sigma_{33}}{Y_T}\right)^2 + \left(\frac{\sigma_{12}{}^2 + \sigma_{13}{}^2}{S_L{}^2}\right) + \left(\frac{\sigma_{23}{}^2 - \sigma_{22}\sigma_{33}}{S_T{}^2}\right)^2$	$d_{mt}{}^2 = \left(\frac{\sigma_{22}}{Y_T}\right)^2 + \left(\frac{\sigma_{12}}{S_L}\right)^2 + \left(\frac{\sigma_{33}}{S_T}\right)^2$	(2.13)
Matrix crushing	$d_{mc}{}^2 = \frac{1}{Y_C}\left[\left(\frac{Y_C}{2S_T}\right)^2 - 1\right](\sigma_{22} + \sigma_{33}) + \left(\frac{\sigma_{22} + \sigma_{33}}{2S_T}\right)^2 + \frac{(\sigma_{23}{}^2 + \sigma_{22}\sigma_{33})}{S_T{}^2} + \frac{(\sigma_{12}{}^2 + \sigma_{13}{}^2)}{S_L{}^2}$	$d_{mc}{}^2 = \frac{1}{4}\left(\frac{-\sigma_{22}}{S_T}\right)^2 + \frac{Y_C{}^2\sigma_{22}}{4S_T{}^2 Y_C} - \frac{\sigma_{22}}{Y_C} + \left(\frac{\sigma_{12}}{S_L}\right)^2$	(2.14)
Delamination	-	$d_{del}{}^2 = \left(\frac{\sigma_{33}}{Z_T}\right)^2 + \left(\frac{\sigma_{23}}{S_T}\right)^2 + \left(\frac{\sigma_{31}}{S_L}\right)^2$	(2.15)

Delamination can also be simulated by use of a Cohesive Zone Model (CZM) which considers a separate constitutive law for the interlayer matrix material between laminate layers [65]. CZM theory relates the tractions to the displacement jumps at the interface where a crack may occur. The strength of the interface governs the damage initiation

whereas damage evolution is related to the critical strain energy release rate. Residual traction force by the interface is reduced to zero when the total area under the traction-separation curve becomes equal to its critical fracture toughness. CZM considers a linear elastic traction-separation law for the undamaged material and a stress based criterion for damage initiation.

2.1.4 Behind Armor Blunt Trauma (BABT), NIJ 0101.06 standard and Injury Tolerance Criteria

2.1.4.1 Behind Armor Blunt Trauma (BABT)

BABT covers a range of non-penetrating injuries to the human torso resulting from projectile impacts on personal armor. Even if the armor prevents complete penetration, the energy imparted to the armor backing and body wall can be high enough to cause serious injury to the thoracic and abdominal contents behind the armor plate. This may even result in fatality. BABT has gained prominence since the 1970s for two principal reasons. First, increases in projectile caliber and energy over time, and second the success of armor designers in developing working armor solutions with less areal density in order to reduce the gross gear weight carried by personnel in the field [6].

BABT manifests itself due to stress wave transfer from the local point of impact on the armor to the underlying tissue. The rear of the armor deforms at high velocities and accelerates underlying viscera locally causing tissue shearing. This is then followed by distributed load on the thorax by movement of the whole plate resulting in organ stretching and contusion. The type and extent of BABT injuries depend on the magnitude of body wall deflection and the rate at which it occurs. Evidence collected from survey of known BABT cases with hard armor shows that it occurs for projectile

caliber of 7.62 mm or higher. No known cases of BABT from 5.56 mm caliber exist [66].

2.1.4.2 National Institute of Justice (NIJ) 0101.06 body armor standard

Current armor standards like the NIJ 0101.06 quantify armor rear face deformation in terms of Back Face Signature (BFS) measured on a Roma Plastilina® clay backing. BFS is the perpendicular distance between two tangential planes of the deformation indent, both of which are parallel to the front surface of the clay backing material. The standard permits a maximum allowable BFS of 44 mm for armor against 7.62 mm caliber rifle rounds. V_{50} is another ballistic parameter that defines the armor performance. It is the velocity at which the armor panel can stop 50% of the bullets. It is calculated by plotting the measured velocity values for complete and partial penetration against probability of penetration (complete penetration value assigned: 0, partial penetration value assigned: 1) in a Sigmoidal or Logistic function plot. NIJ standard recommends V_{50} values to be equal or higher than the conditioned armor test velocities listed in Table 8.

Table 8 Threat specifications and requirements of NIJ 0101.06 standard.

Armor type	Test bullet	Bullet mass	Conditioned armor test velocity	Normal hits per panel	Maximum BFS depth
Level III	7.62 mm NATO FMJ	9.6 g 147 gr	847 m/s 2780 ft/s	4 - 6	44 mm 1.73 in
Level IV	.30 Cal. M2 AP	10.8 g 166 gr	878 m/s 2880 ft/s	1 - 6	44 mm 1.73 in

NIJ 0101.06 is a part of The Standards and Testing Program as a basic and applied research effort to set minimum performance standards for specific devices, commercially available equipment nationally and internationally, that form a part of the body armor system. It also specifies the methods that are to be used to test their performance. Body

armor models that meet the minimum performance requirements are selected for inclusion on the NIJ Compliant Products List. The tests and methods prescribed by the standard are also used by other agencies for equipment selection according to their own requirements. The standard classifies ballistic performance according the caliber and type of projectile threat that can be defeated.

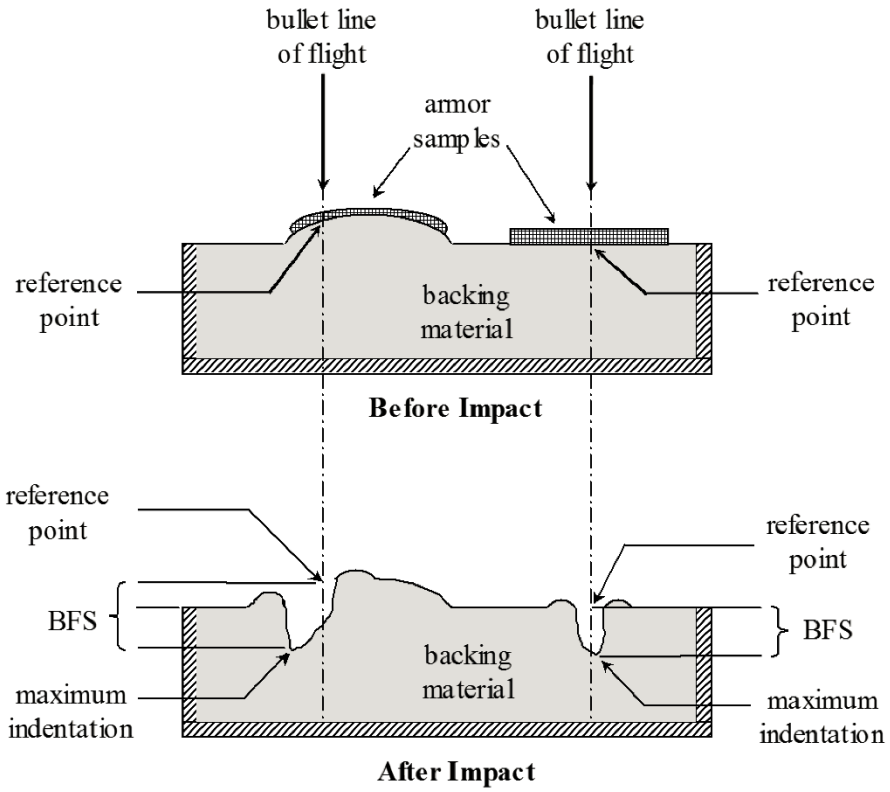

Figure 3 Measurement of Back Face Signature (BFS) as stated by NIJ 0101.06 standard.

2.1.4.3 Injury Tolerance Criteria

Categorizing ballistic performance, resulting BABT injury and survival probability based on BFS size (diameter and depth) in clay has limitations. The 44 mm clay BFS limit has been adopted from the 1977 Prather blunt impactor study [67] on anaesthetized goats, gelatin, clay, and other backing materials. It concluded 44 mm deformation

magnitude correlated to a 4% probability of death in goats. No tests were done on human cadavers. Roma Plastilina® #1 clay emerged from this study as a cheap alternative BFS recording medium to the then prevalent expensive gelatin with high speed camera. [68] points out that the selection of clay as a recording medium by Prather was based on recorded deformation-time histories at low speed impacts which may not apply to impacts at high speeds. Clay is a highly plastic material which undergoes viscous flow not identical to the human body. Hence, clay only serves as a "convenient" recording medium and not a body simulant. Recently, research groups have tried to address this issue by attempting to develop the maximum allowable clay BFS lethality relationship by corresponding body armor tests on clay, porcine surrogates, and human cadaver torsos. Gryth *et al.* [69] concluded a maximum allowable clay BFS should be 28 mm to ensure the highest probability of survival. Bass *et al.* [70], on the other hand, found clay BFS did not correlate well with impact velocity and in turn the corresponding human body BABT response.

The lack of a substantial medical basis to correlate clay BFS to human BABT injury tolerance level has led the scientific community to reassess its phenomenon. Studies on animals, human cadavers, bio-fidelic surrogates, numerical models, and instrumented dummies have extended the understanding of injury mechanisms. Observations have resulted in quantification of human tolerance levels, and the development of numerical relationships between injury and measurable engineering parameters, termed as injury tolerance criteria [68, 71-72]. Detailed description of each criterion is presented in these references. Current accepted standard for assessment of thoracic injury is the Abbreviated Injury Scale (AIS) with range 0 to 6 for increased severity. AIS-code 3

relates to serious injury such as fractures with 8-10% probability of death. Most studies report injury tolerance criteria for AIS-code 3+ or AIS-code 4 (up to 50% probability of death).

Table 9 Injury tolerance criteria published in literature for frontal chest impact.

Criterion	AIS-code	Magnitude	Reference
Whole body peak acceleration	3	60-80g	[71]
Peak sternal force	3	3.3 kN †	[71]
	3	21 kN *	[70]
	4	25 kN *	
Percent compression of chest (low velocity impact)	3	20%	[71]
	4	34%	
Viscous injury	3	1.0 m/s	[71]

† From a 15 cm diameter pendulum impact, * 7.62 NATO Ball impact on hard UHMWPE armor.

Injury tolerance criteria are still in a preliminary stage. Additional experimentation is necessary to make it robust for design applications. Until that point, body armor must be designed to comply with existing criteria using a method that allows easy adaptation of newly evaluated biomechanical parameters.

2.2 Summary of observations from the literature review

A review of published literature on impact protection structures like armor reveals the evolution of their design over the years. Scientific research has been particularly directed to improve the fidelity of material selection and optimization process for this application through various performance verification methods and testing procedures. A primary objective of this research has been to make these structures lightweight and ever more efficient by improving properties of the materials chosen and how the structure exploits them to advance its performance. Basic concepts pertaining to modern armor and

involved materials were identified through this review and they are summarized as follows:

- Modern projectile impact protective structures like body armor are multilayered hybrid composite systems that combine advantages of different materials in a unified solution for providing the desired level of protection. These structures are also known as integral armors.
- Design parameters for such structures are based on the regulations set by standards like those by NIJ or MIL. For example, the NIJ standards categorize body armor according to the perceived threat type to be defeated; and set primary requirement limits for areal density, maximum allowable BFS, and working projectile velocity range. Secondary requirements are set by desired ergonomics and in-field handling. All these factors govern material choice and layup, method of fabrication, desired curvature, and permissible thickness for the final body armor product.
- Survey of review publications indicate most contemporary materials used in projectile impact protective structures are metals, ceramics, and high strength fabric composites. In the case of hard plate body armor, material choice depends on whether the projectile to be defeated is armor piercing (AP) or soft core deformable. Armor protecting against AP projectiles utilize both ceramics and high strength fabric composites, whereas those protecting against soft core projectiles can be solely composite based.
- Ceramics help in breaking/blunting the AP projectile (hence termed disruptors). Composites help in kinetic energy absorption through plastic deformation modes (termed absorbers) and reduce the extent of brittle cracking in ceramics.

- A variety of high strength fabrics like Aramids, UHMWPE, glass etc. have been used in composite based armor. Fabric based body armor functions well against deformable threats by distributing the kinetic energy through the high strength fibers with dissipation modes including fiber shear or fracture, fiber tensile failure, or straining and associated delamination or pullout. Their performance is quantified by their ability to absorb a projectile's kinetic energy and spread it out fast before local failure occurs. UHMWPE is the leading candidate material available at present for composite armors.
- Ceramics are the most resistant materials to compressive stresses and are an excellent choice as disruptor layer first facing the impact. The choice of a ceramic material for a specific armor application is usually based on performance to cost. For example, SiC and B_4C are harder materials with lower densities than alumina but cost more. However, their ability to defeat more tenacious threats with lower weight penalties has resulted in their favored use in armor. Ballistic performance of ceramics is also susceptible to variations in manufacturing processes and parameters used therein. A performance survey by Hazell [13] indicates HP SiC has the highest tenacity to defeat AP threats.
- Impact stress waves tend to lose energy when they encounter materials of different mechanical properties due to acoustic impedance. Multilayered armor benefits from this aspect. The order of layering constituent materials in such armor along with their chosen areal densities thus have to be optimized to maximize the energy absorption capacity of the system during each stage of projectile impact with due consideration of wave propagation effects.

- Structural integrity of multilayered armor depends extensively on inter-laminar shear stresses between individual layers. Although it is possible to achieve this with the use of more adhesive, thicker adhesive layers exacerbate damage in ceramic layers. A solution to this problem is using the highest specific strength adhesive with minimal thickness to bond constituent layers. Another way to decrease inter-laminar shear stress is by increasing the obliquity of projectile impact on the facing ceramic layer.
- Individual layer areal density is a critical factor that affects performance of multilayered armor. Research indicates that there is an optimal composite areal density in a fixed weight multilayered unit at which its performance peaks [38]. Further areal density increase may not improve the armor performance while adding non-functional weight.
- Collapsible energy absorbers (cellular solids) like honeycombs and foams have potential to be used as a constituent layer in multilayered armors. The use of such materials can be particularly effective as they allow maximum acoustic impedance due to their high elastic modulus difference compared to contemporary armor materials. Unlike compliant materials like rubber which have been used for increasing acoustic impedance, cellular solids can do this while maintaining the required structural stiffness. A review of prior publications on this topic [7-9, 39] indicates:
    - Their use in armor can be considered fairly recent as the first published reference indicating this is dated to 1994. A honeycomb layer was used in a multilayered armor as a spacer to minimize energy transfer and stress propagation that

prematurely failed successive layers on impact. Isolation of successive layers from initial stages of impact and helped in gradual dissipation of shock.

- A honeycomb layer also helped to reduce back face bulging in a multilayered armor. The decrease in bulging velocity was found to be proportional to the increase in honeycomb layer thickness. However, this phenomenon was only prominent against soft core deformable projectiles and not AP ones.
- Ballistic performance of honeycombs can be improved by increasing the cell wall as well as panel thickness or by reducing its cell size.
- Review on use of aluminum foam in armors indicates that the time lapse for foam densification corresponded to the delay in stress wave transfer to the back layer. Inclusion of foam also helped to reduce the back face bulging and individual layer debonding in armor. Most importantly, armor plates with foam layers were found to perform better than the non-foam baselines of same areal density.
- Use of cellular solids has predominantly been in mounted armor like those on vehicles. Their role in close contact protection units similar to body armor remains largely unexplored.

Information summarized above can serve as a guideline to innovate new armor designs. The introduction of cellular solids as constituent materials in integral armor presents new horizons for stress wave mitigation to be explored. Successful preliminary use in vehicle armor application supports introducing these materials to the personal body armor domain. Publications reveal most research groups have relied on 3 design steps (a) material selection, (b) experimental evaluation, and (c) numerical, analytical or micromechanical evaluation to verify the performance of their armor concepts.

Experimental testing followed with numerical corroboration has continued to gain impetus as commercial FEA software codes enable a cost-effective and faster turn-over of verification and optimization steps. Accuracy of FEA results depends largely on the chosen material models for simulations. Errors in inputs for the material models results in incorrect visual and numerical responses. Hence, significant research effort has been dedicated to improve the fidelity of the material models.

Metallic constituents involved in dynamic impact simulations (both in projectiles and impacted plates) have been predominantly modeled using the Johnson-Cook plasticity and fracture criteria. The following observations were made after reviewing publications pertaining to this topic:

- A range of Johnson-Cook material parameters have been chosen by research groups for modeling the steel core, lead core, and gliding brass jacket of bullet projectiles. The numerically obtained results are subjective to the chosen inputs.
- Data for these bullet materials is generally not disclosed in literature and a process to experimentally evaluate it is difficult.
- Estimation of plasticity in the steel core appears as a contentious topic amongst research groups. Most research groups have considered the core to be a rigid body. This may be true for impact simulations on soft materials but it is a gross over estimation of penetration capability for simulations on hard materials. Experiments have shown the core to undergo mid-plane fracture when used for tests on thick ceramic plates. Neglecting the lead filler can also be erroneous as it also has a proven influence on the penetration capacity of the bullets as seen through experiments.

- Material modeling of the lead core has proved difficult. Lead being a relatively soft material behaves fluid-like at high strain rates. This, coupled with its high density, manifests in FEA as excessive contact overclosures, mesh distortions from unresolved high deformations, and unrealistic strain. The Lagrangian scheme is unable to tackle this problem causing research groups to apply other techniques like adaptive meshing, ALE, and SPH. The Mie-Grüneisen EOS model coupled with Johnson-Cook has also been implemented to supplement Von Mises flow stress based computations with a pressure-volume relationship. Limited success has come out of these efforts as these methods did not give a good description of the perforation process.

Shortcomings of the current modeling schemes for these metals are a research gap. Modeling ceramics using JH-2 criterion has proven successful. JH-2 is able to balance accurate representations of the physical phenomenon while maintaining computational efficiency. Apart from phase change effects at elevated pressures this model can correctly predict final-buckling pressure and stress pressure history. Similarly for composites, Hashin criterion proves suitable for impact simulations. Ballistic impact of armor involves a three-dimensional stress state which needs failure prediction models that can capture both in-plane and inter-laminar stress components. This can be achieved by the Hashin criterion when supplemented by delamination models like the Hou or Puck criterion or the use of CZM. Strain-rate dependence and adiabatic effects have not been considered in these composite models.

Behind Armor Blunt Trauma (BABT) is a rising issue in body armor primarily due to increases in penetration capacity of projectiles and a decrease in areal density of armor

solutions. BABT manifests itself due to stress wave transfer from the local point of impact on the armor to the underlying tissue. Hence, a hybrid composite body armor concept with increased acoustic impedance by inclusion of a cellular solid layer is a candidate to solve this issue.

CHAPTER 3. EXPERIMENTAL INVESTIGATION OF BACK FACE SIGNATURE (BFS) REDUCTION IN A LEVEL III HYBRID COMPOSITE ARMOR (HCA) INCLUDING A HONEYCOMB CELLULAR SOLID LAYER

3.1 Introduction

Body armor designed to protect against rifle caliber small arms with deformable (lead core) projectiles are now typically made of hard laminates of high strength fabric composites without ceramic components. These are classified as level III armor according to the National Institute of Justice (NIJ) 0101.06 standard. They function by dissipation of a projectile's kinetic energy through fiber failure modes including: shear or fracture, tensile failure, or straining, fiber-pullout, and associated matrix failure causing delamination [73]. For best performance, fibers with high tenacity like Ultra High Molecular Weight Polyethylene (Spectra®, Dyneema®) and Aramids (Kevlar®, Twaron®, Zylon®) are used to achieve maximum energy dissipation [17-18]. Fiber volume percentage in these composites is kept high to achieve maximum utilization of the fiber properties. The low resin content aids in pliability at relatively high thicknesses which, although it improves the wearer's mobility and comfort, it adversely affects the armor's back face deformation post projectile impact.

Higher magnitudes of back face deformation leads to higher body wall deflections and blunt trauma, which may even be fatal. This problem can be solved by coupling these composites with stiffer armor materials like ceramics and metals but not without a significant weight penalty. A new solution lies in pairing armor composites with cellular solids in a sandwich construction. Aluminum based cellular solids have been successfully integrated in hybrid armor and have brought forth other benefits apart from reduction in back face deformation. These include reduction in: energy transfer and the propagation of stress waves (giving gradual dissipation of shock loads), individual layer debonding, and bulging velocity [7-9].

Application of cellular solids in body armor remains unexplored. Recently, a multilayered hybrid composite body armor (HCA) insert was designed using Dyneema® HB50 laminates and amorphous metal based honeycomb (AMH) for protection against deformable lead core 7.62 mm NATO Ball FMJ projectiles in accordance to the NIJ 0101.04 level III standard [74]. It utilized the abovementioned advantages of cellular solids through AMH for BFS reduction. Preliminary experimental evaluation through ballistic testing indicated this HCA was able to reduce the BFS by 16.7% and damage cross section area per shot by 9.7% compared to the HB50 monolith baseline. The study also concluded that if design deficiencies in AMH could be solved the BFS reduction could be increased up to 37%. An interim alternative to solving these deficiencies is selecting a new honeycomb for HCA that can achieve the set objective.

A focus of this investigation is to experimentally validate the ballistic performance benefits from HCA for a new prototype that includes an aluminum honeycomb as a replacement for AMH. Background information on the design hypothesis, involved

materials and inherent deficiencies of AMH are discussed in the following section 3.2. Details of the new HCA prototype and fabrication process are presented in section 3.3. Ballistic testing procedure and objectives are presented in section 3.4. Tests are aimed to verify the role and influence of the honeycomb in the functioning of HCA through specific lay-up scenarios of individual constituents of the HCA. Observed results and pertaining discussion is in section 3.5. In some tests, the performance comparisons of HCA are drawn with monolith HB50 baseline inserts of similar areal densities to negate the influence of incurred weight penalty from the honeycomb addition.

3.2 Background on the first HCA prototype (HCA-P1) and deficiencies of AMH

HCA-P1 was a multilayered sandwich concept (AMH sandwiched between Dyneema HB50 laminates) aimed to function as a stand-alone insert providing protection following the level III specifications of NIJ 0101.04. It could be placed in the Improved Outer Tactical Vest (IOTV) pocket of the Multiple Threat Body Armor (MTBA) similar to the Enhanced Small Arms Protective Insert (ESAPI) currently used by U. S. ground troops. Design constraints for HCA-P1 were specified by the Naval Research Lab (ONR Grant N00173-071-G001) requiring the functional areal density of inserts to be around 18.5 kg/m^2 (3.8 lb/ft^2) with Back Face Signature (BFS) less than 44 mm at V_{50} velocities above 838 m/s. The front facing HB50 laminate of HCA-P1 intercepted the projectile first and deformed it, distributing the energy over a significantly large region to avoid local failures by force concentration. During partial penetration of the front layer, AMH functioned as an energy diffuser, thereby reducing the armor BFS and the resulting blunt trauma. AMH inclusion also helped to limit the spread of fabric delamination damage

allowing an improved multi-hit capability. As a final layer of protection against fragmentation, a thin laminate of HB50 formed the backing spall liner.

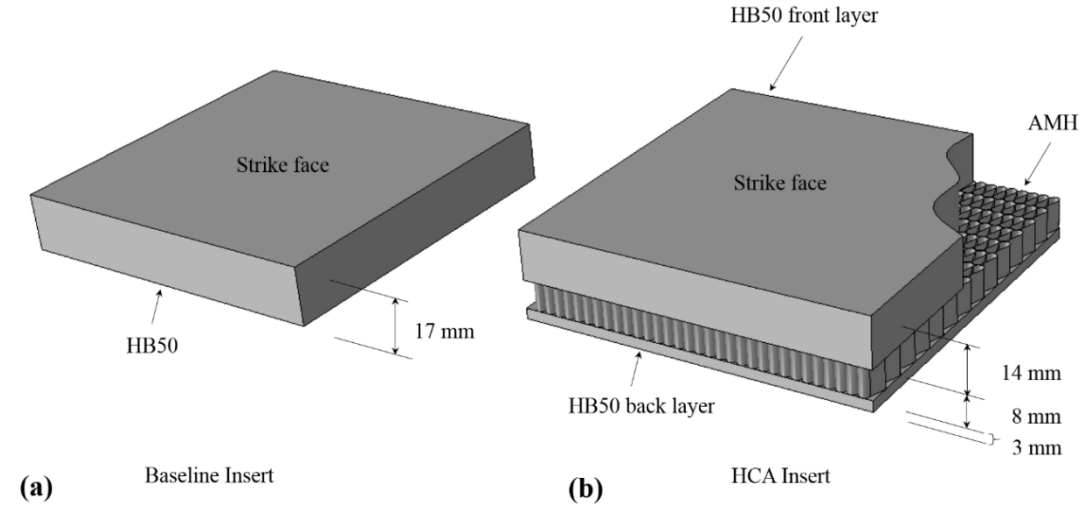

Figure 4 Schematic of the armor inserts used for ballistic test (not to scale). (a) Baseline HB50 insert (b) assembled HCA-P1 with the AMH core. Orientation and thickness of each constituent layer is shown.

The front HB50 layer had adequate areal density to avoid complete penetration. This was because, in case of penetration, the out-of-plane oriented porosity of AMH will result in minimal resistance to projectile traverse thereafter, negating its benefits. From the data in [26], a 16 kg/m^2 areal density HB50 laminate (close to 68 plies) is adequate to defeat the 7.62 mm NATO Ball FMJ threat. This laminate areal density corresponds to approximately 17 mm in thickness. For HCA-P1, this HB50 laminate was divided in a 14 mm front laminate and a 3 mm backing spall liner. AMH was bonded between these laminates using a cyano-acrylate adhesive. Observed performance improvements of HCA-P1 are summarized in Section 3.1 and [74].

The size limitation barrier seen in amorphous metal cellular solids was lifted by making AMH with slip-cast MetGlas® MB2826 ribbons [75]. The bottom-up AMH

fabrication process relied on manual periodic elastic bending on the ribbon precursor to form overlap joints which were then bonded using adhesive. This process had inherent deficiencies:

a. Fabricated samples from the manual process had defects such as cell wall misalignment, bonding mismatch, and incorrect cell size. This resulted in a drop in crush strength from ideal 10.8 MPa to 4.8 MPa.
b. Adhesive bonding resulted in 20-30% non-functional weight addition to AMH giving a non-optimal density while reducing the specific strength of the honeycomb. Inadequate bond strength does not allow for stress stabilization during cell wall bending, resulting in a steady decline in crush strength until densification.
c. The production rate of AMH was low to sustain frequent fabrication of large samples required for inclusion in armor plates (15 mm^2/min approximately).

While these issues are being resolved, an interim solution can be achieved by inclusion of conventional high specific strength aluminum honeycombs in the HCA.

3.3 Revised HCA with Aluminum honeycomb (HCA-P2)

Quasi-static (as per ASTM C365M-05) and dynamic compression tests using a Split Hopkinson Pressure Bar setup were done on AMH samples for mechanical property evaluation [76]. Aluminum CR-PAA 1/8-5052-0.003 corrugated honeycomb (Al-CH) was selected as a replacement for AMH for its relatively close mechanical properties among commercially available options (Table 10). The design principles, applied

constraints, layup sequence, and constituent layer thicknesses of HCA-P2 were kept identical to that HCA-P1.

Table 10 Mechanical property comparison of honeycombs included in HCA.

Honeycomb type	Density (kg/m^3)	Elastic modulus (GPa)	Peak strength (MPa)	Crush strength (MPa)	Energy absorption capacity (MJ/m^3)
Amorphous Metal Honeycomb	290.0	2.0	13.2	5.7	4.0
Aluminum, CR-PAA 1/8 - 5052 - .003	192.2	6.2	18.6	9.3	6.5

Thermoplastic modified polyolefin based adhesive films were used as the bonding adhesive in HCA-P2. Nylon based Cordura wrap was used instead of Kevlar 49. Inserts were fabricated using a hand layup process and consolidated with a hot press at 104°C.

3.4 Ballistic testing of HCA-P2

Ballistic testing of all inserts was done in accordance to the specification for a level III armor in the NIJ 0101.06 standard. The test was conducted at 28°C ambient temperature with 50% relative humidity in a stand-alone setup (testing target plates alone without putting them inside a vest pocket). The projectile selected for tests was the 7.62 mm NATO ball M80 round. Projectile velocity was adjusted by reloading the rounds with controlled powder charge weights. Parameters for performance comparison between the baseline and HCA inserts were BFS and the V_{50}.

BFS readings were taken from the Roma Plastilina® #1 clay backing using a high precision Vernier scale (least count 0.01 mm). Temperature of the clay during the test duration was kept close to 38°C to maintain the minimum BFS requirements monitored by drop weight calibration tests. BFS readings were adjusted to that at the control

temperature in order to compensate for temperature drop during tests using correction factors (additional details in Appendix 1). Inserts were mounted on the clay backing using Velcro straps. The setup was adequately rigid to maintain uniformity and repeatability in tests. Precautions were taken to maintain the prescribed minimum shot-to-shot distance. A CED M2 chronograph was used for velocity measurements.

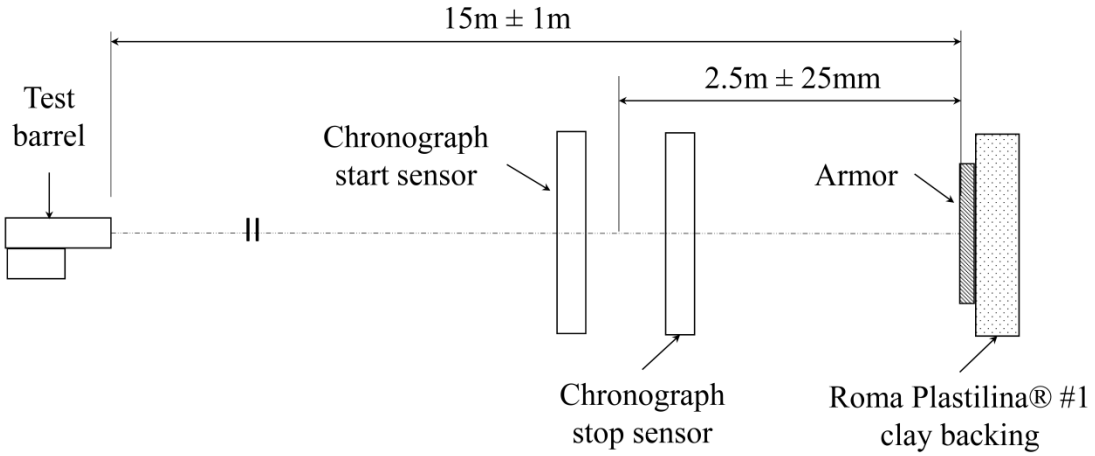

Figure 5 Schematic of the ballistic testing setup used as per the NIJ 0101.06 body armor standard.

Velocities corresponding to complete and partial penetration were plotted against probability of penetration (complete penetration: 0, partial penetration: 1). V_{50} was calculated by taking the arithmetic mean of an equal number of the highest partial and the lowest complete penetration impact velocities as per MIL-STD-662F as recommended in NIJ 0101.06 standard. Each insert was shot multiple times to meet the test result requirements. NIJ recommends a minimum shot-to-shot distance of 51 mm to avoid performance interference from previous shots in assessing fairness of the test. The shot-to-shot distance in all the tests exceeded more than twice the minimum requirement. A schematic of the test setup is shown in Figure 5.

The experimental investigation spanned over 4 tests with each test aimed at a specific objective. Schematic in Figure 6 presents a flow chart representation of the investigation. Detailed description of each test is presented in the following sub-sections.

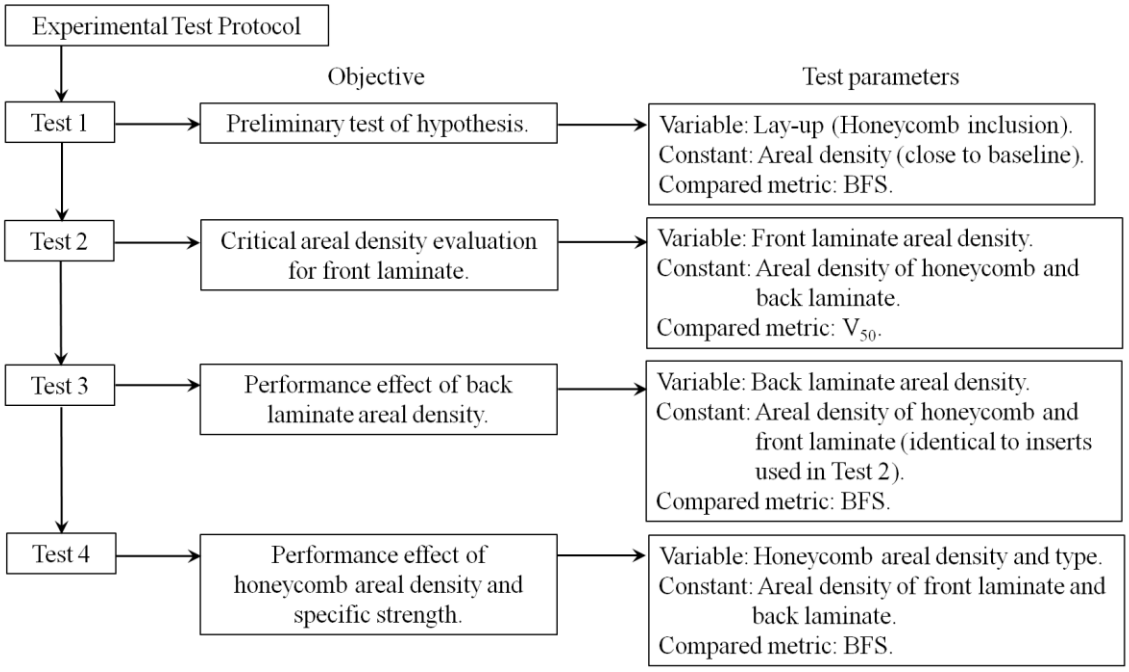

Figure 6 A flowchart schematic that illustrates the experimental test protocol used in the present study to test the hypothesis.

After conducting the tests, shot inserts were cut in the through-thickness direction using water-jet machining and visually inspected to identify failure mechanisms in the insert constituent materials and categorize the role of the honeycomb in the projectile defeat mechanisms of HCA.

3.4.1 Test 1: Preliminary testing and BFS comparison with baseline

HCA-P1 results indicated performance benefits of honeycomb inclusion in the armor. An aim of this preliminary ballistic test was to prove that inclusion of the chosen Al-CH, with better mechanical properties than early AMHs, will result in a better ballistic performing HCA-P2 compared to a baseline of similar areal density. BFS was chosen as

the parameter for comparison, and hence shot velocity was not intentionally increased up to complete penetration. Details of the tested inserts are presented in Table 11.

Table 11 Details of armor inserts manufactured for preliminary ballistic test.

Armor type	Layup description	Functional unit areal density (kg/m^2)	Final areal density with wrap (kg/m^2)	Number of inserts
Baseline	14 mm HB50 + 3 mm HB50, compact bonded	15.2	16.53	2
HCA-P2	14 mm HB50 + 8 mm Al-CH + 3 mm HB50, compact bonded	16.51 ± 0.06	17.97 ± 0.06	2

3.4.2 Test 2: Critical areal density evaluation using V_{50}

The second set of ballistic tests was conducted to verify if the areal density of HB50 can be reduced in HCA-P2 by inclusion of Al-CH; thereby reducing the required total areal density of the armor. Since the front HB50 laminate had the highest areal density, its thickness was selected as the test variable. Reduction in areal density was likely to have a proportionate reduction in penetration resistance of the inserts. Hence, V_{50} was chosen as the parameter for comparison. Three variants of HCA-P2 were manufactured and tested. Their details are presented in Table 12. For effective one-to-one comparison, baseline HB50 monolith inserts of similar areal density as HCA-P2 variants were also manufactured and tested. Shot velocities were gradually increased until complete penetration was achieved and then varied as per MIL-STD-662F. The test objective was to identify a minimum areal density of baseline and HCA-P2 with V_{50} of 847 m/s; the reference velocity recommended by the NIJ 0101.06 standard. This minimum areal density is termed hereon as the Critical Areal Density (CAD).

Table 12 Details of armor inserts manufactured for V_{50} evaluation.

Armor type	Layup description	Functional unit areal density (kg/m^2)	Final areal density with wrap (kg/m^2)	Number of inserts
Baseline Variant-1	10 mm HB50 + 10 mm HB50, compact bonded	18.99	20.02	1
HCA-P2 Variant-1†	14 mm HB50 + 8 mm Al-CH + 2 mm HB50, compact bonded	19.14	20.17	2
Baseline Variant-2	15.5 mm HB50	15.14	16.36	1
HCA-P2 Variant-2	12 mm HB50 + 8 mm Al-CH + 2 mm HB50, compact bonded	15.58	16.58 ± 0.01	2
Baseline Variant-3	12 mm HB50 + 2 mm HB50, compact bonded	13.92	14.94	1
HCA-P2 Variant-3	10 mm HB50 + 8 mm Al-CH + 2mm HB50, compact bonded	13.75 ± 0.22	14.76 ± 0.24	2

† Variant-1 is identical to the HCA-P2 plate used in preliminary testing. Higher functional areal density seen here is due to HB50 laminates procured from a different supplier.

3.4.3 Test 3: Effect of back laminate thickness on ballistic performance of HCA

Test 3 was performed to verify the ballistic performance influence of back laminate thickness. HCA-P2 variant-2 and variant-3, which had reduced front laminate areal densities, were supplemented with a commercially available level IIIA vest liner (areal density: 9.77 kg/m^2). This approach is similar to increasing the areal density of the spall liner back laminate relative to the front laminate without having to fabricate new inserts. In doing so, the location of the honeycomb layer was raised along the out-of-plane direction with respect to the armor rear face in contact with the backing clay. BFS and V_{50} were chosen as the comparison parameters. Observed results were compared with those of variant-1 HCA-P2 insert. A commercially available standard level III insert was

also included in the test for performance comparison with HCA-P2 inserts. Details of the test inserts are in Table 13.

Table 13 Details of armor inserts tested for verifying performance influence of honeycomb location and comparison with commercial plate.

Armor type	Layup description	Functional unit areal density (kg/m^2)	Final areal density with wrap (kg/m^2)	Number of inserts
HCA-P2 Variant-2 combination	HCA-P2 Variant-2 + level IIIA vest liner	25.34	26.37	2
HCA-P2 Variant-3 combination	HCA-P2 Variant-3 + level IIIA vest liner	23.29	24.27	1
Level III standard insert	Alumina ceramic + polymer wrap	-	38.57	1

3.4.4 Test 4: Effect of honeycomb areal density and specific strength on ballistic performance of HCA

Geometric attributes and base material of a honeycomb govern its total energy absorption capacity E_{hc}. This can be illustrated through the expression:

$$E_{hc} = \int_0^{\varepsilon_D} \sigma_{cr}\, d\varepsilon \times A \times c. \tag{3.1}$$

Assuming a constant densification strain $\varepsilon_{D,}$ crush strength σ_{cr} and contact area A, increasing the thickness c of the honeycomb layer (which is synonymous to increasing its areal density) should predictably improve E_{hc} and the ballistic performance of the insert as more material is available to participate in the energy absorption process. Similarly, decreasing honeycomb cell size or increasing its foil thickness, which thereby reduces the amount of porosity, should improve the performance. Variation in honeycomb thickness

c is relatively easy and less cost prohibitive. New inserts of HCA-P2 were made using 6 mm (variant-4) and 10 mm (variant-5) thickness Al-CH and tested along with the 8 mm Al-CH variant-1 to study the effects of thickness variation. BFS was the chosen parameter for comparison. Based on the limited strain rate effects in Al-CH observed from the preliminary test data and analytical model considerations, the change in honeycomb thickness by a constant magnitude should predictably reflect in the BFS versus velocity plot in the form of parallel and proportionate curve translation. This hypothesis was experimentally tested here.

Table 14 Details of HCA-P2 inserts manufactured for verifying ballistic performance influence of honeycomb thickness.

Armor type	Layup description	Functional unit areal density (kg/m^2)	Final areal density with wrap (kg/m^2)	Number of inserts
Baseline	10mm HB50 + 10mm HB50, compact bonded	19.56 ± 0.03	20.08 ± 0.03	4
HCA-P2 Variant-1	14mm HB50 (4+10) + 8mm Al-CH + 2mm HB50 (1+1), compact bonded	18.38 ± 0.02	18.89 ± 0.03	2
HCA-P2 Variant-4	14mm HB50 (4+10) + 6mm Al-CH + 2mm HB50 (1+1), compact bonded	18.26 ± 0.04	18.82 ± 0.03	3
HCA-P2 Variant-5	14mm HB50 (4+10) + 10mm Al-CH + 2mm HB50 (1+1), compact bonded	18.90 ± 0.03	19.47 ± 0.03	2

HB50 ply layup was modified during insert fabrication in Test 4 for streamlining inventory. The front 14 mm HB50 laminate in all HCA inserts was consolidated by compact bonding four individual 1 mm laminates to a 10 mm laminate using the polyolefin based adhesive film in a hot press. The 2 mm back laminate was similarly

consolidated by bonding two individual 1 mm laminates. The temperature and pressure conditions during bonding were identical to that of HCA-P2 inserts made for earlier tests. Increasing the volume fraction of the stronger polyolefin adhesive within HCA-P2 inserts was expected to correspondingly increase the inter-laminar shear strength and decrease the extent of delamination. Increased flexural stiffness as a consequence was to aid in BFS reduction. Details of the fabricated inserts are in Table 14. Baseline inserts made by compact bonding two 10 mm laminates were included in the test for performance comparison.

An alternate approach to vary E_{hc} is by changing the honeycomb crush strength σ_{cr} via the base material type. New variants of HCA-P2 were made with an inclusion of a meta-aramid based Nomex™ honeycomb (NH) to study its influence on ballistic performance and gauge the extent of honeycomb participation in the energy absorption process. The honeycomb was selected among commercially available options of this base material type to have intermediate crush strength between AMH and Al-CH (refer Table 10). Honeycomb cell size and foil thickness is similar to that of Al-CH. The gradual strength increments between the honeycombs help to visualize a performance transition, if any. Details of the chosen honeycomb are in Table 15.

Table 15 Mechanical property details of the chosen Nomex™ honeycomb.

Honeycomb type	Density (kg/m^3)	Elastic modulus (GPa)	Peak strength (MPa)	Crush strength (MPa)	Energy absorption capacity (MJ/m^3)
Nomex™, PN2- 1/8 - 9.0	149.1	< 1*	14.79	7.4	5.1

* Elastic modulus not specified in the product data sheet. Value stated here is experimentally observed for similar honeycombs of this type.

Inserts made using 8 mm (variant-6), 6 mm (variant-7) and 10 mm (variant-8) thickness NH were tested for BFS measurement. Identical thickness to Al-CH based variants will aid in a one-to-one comparison and assist in testing the hypothesis stated earlier for Test 4. Details of the NH based HCA-P2 inserts are in Table 16.

Table 16 Details of NH based HCA-P2 inserts manufactured for verifying ballistic performance influence of honeycomb specific strength and thickness.

Armor type	Layup description	Functional unit areal density (kg/m^2)	Final areal density with wrap (kg/m^2)	Number of inserts
HCA-P2 Variant-6	14mm HB50 (4+10) + 8mm NH + 2mm HB50 (1+1), compact bonded	18.13 ± 0.01	18.65 ± 0.03	2
HCA-P2 Variant-7	14mm HB50 (4+10) + 6mm NH + 2mm HB50 (1+1), compact bonded	17.77	18.33 ± 0.02	2
HCA-P2 Variant-8	14mm HB50 (4+10) + 10mm NH + 2mm HB50 (1+1), compact bonded	18.31 ± 0.06	18.89 ± 0.06	2

3.5 Results and discussion

A summary of test results is presented in Table 17. Error in the velocity readings was ±5 m/s as seen during chronograph calibration. Error in BFS diameter size and depth measurement is compounded human and instrument error with a magnitude of ±0.1 mm. Measured values of BFS for both insert types were plotted against the corresponding projectile velocity (Figure 7). A semi-empirical model based on energy balance, and an analytical model based on conservation of momentum with classical yarn theory was developed to determine the regression fit for BFS versus projectile velocity (V) for deformable projectiles against Dyneema® based armor and presented in [74]. These models were adaptations of those in [22] and [77] respectively, that were designed

specifically for V_{50} estimation. It was shown using both methods that BFS varies with velocity according to a second order polynomial function given by:

$$BFS = AV^2 + BV - C. \tag{3.2}$$

Table 17 Summary of results from the preliminary ballistic test.

Armor type	Shot number	Velocity (m/s)	BFS (mm)
Baseline Insert 1	1	780	33
	2	804	42.4
	3	812	45.3
	4	788	35
Baseline Insert 2	1	803	40.9
	2	792	33.9
	3	799	36.4
	4	811	44.7
HCA-P2 Insert 1	1	810	31.7
	2	807	34.1
	3	804	32.1
	4	804	30.6
HCA-P2 Insert 2	1	803	32.2
	2	814	35.1
	3	822	37.3
	4	799	29.5

The second order terms of this function represent the projectile kinetic energy, whereas, the first order terms and the intercept constant represent the energy absorbed by the HB50 laminate. In the case of HCA, the energy absorbed by the honeycomb will also be represented by the first order terms if the honeycomb has significant strain rate dependence. Else, it will be a part of the intercept constant. A detailed explanation for both methods is provided in Appendix 1. Predicted BFS values and calculations using these methods have also been detailed. Resulting trends for calculated BFS have been added to Figure 7 and show good agreement with the experimental results for both the baseline and HCA-P2 inserts.

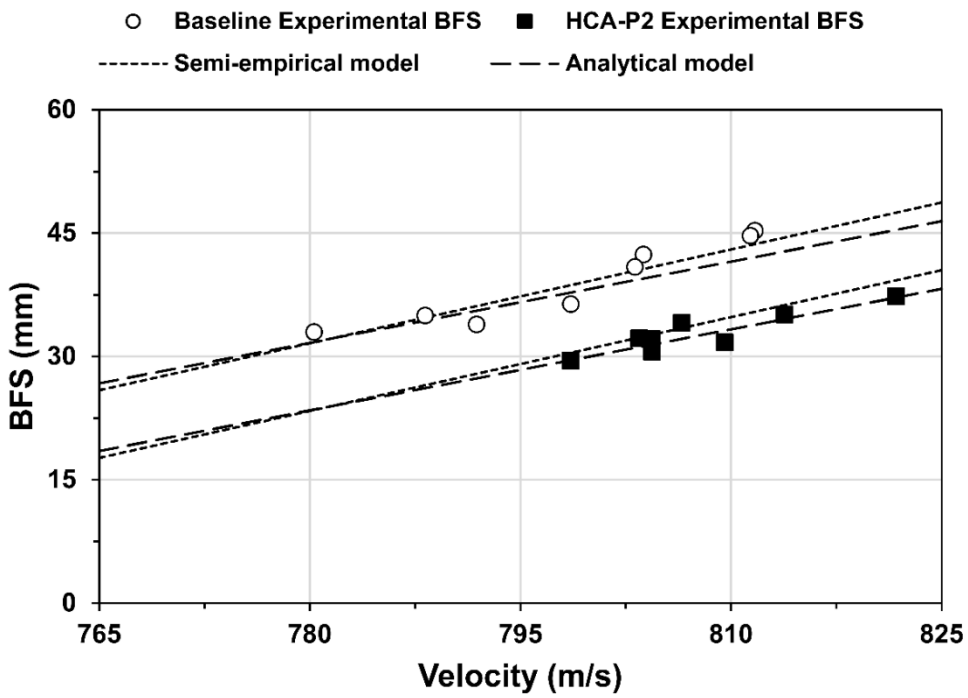

Figure 7 Plot of BFS measured from clay backing versus projectile velocity from the preliminary test for the baseline and HCA-P2 inserts. Calculated BFS plots using semi-empirical and analytical scheme have been added and show a good agreement with the experimental data. Error in velocity and BFS measurement was ±5 m/s and ±0.1 mm respectively.

The analytical model aided to extrapolate the BFS value for each insert at the reference velocity of 838 m/s according to the cited NIJ 0101.04 standard in [74]. It is similarly used here to predict BFS at the NIJ 0101.06 standard reference velocity of 847 m/s. BFS values estimated at 847 m/s were 54.1 mm and 45.8 mm for the baseline and HCA-P2 inserts, respectively. A BFS of 49.3 mm is predicted for a 16.51 kg/m^2 areal density baseline (same functional areal density as HCA-P2) using the analytical model. BFS of HCA-P2 was 7.1% lower than this value for the same areal density. A summary of BFS and BFS per unit functional areal density comparison is shown in Figure 8. Values for HCA-P1 from [74] are also included.

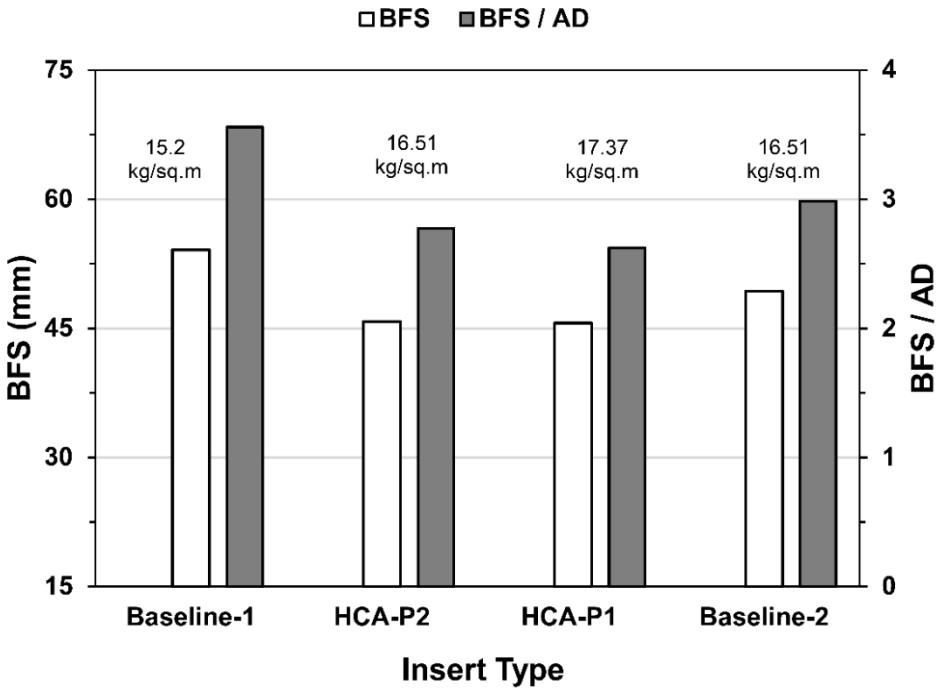

Armor type	BFS at 847 m/s		BFS / AD	Δ BFS /Δ AD
	(mm)	% change	(mm per kg/m^2)	(mm per kg/m^2)
Baseline-1	54.1	-	3.56	-
HCA-P2	45.8	15.34%	2.77	6.34
HCA-P1	45.6	15.71%	2.63	3.92
Baseline-2	49.3	8.87%	2.99	3.66

Figure 8 Summary of BFS based comparison for the tested inserts at the NIJ reference velocity of 847 m/s. Percentage difference between observed values in comparison to the baseline insert from preliminary test (referred as Baseline-1 here) is shown in tabulated form. For effective one-to-one comparison, values predicted for a baseline insert of same weight as HCA-P2 (referred as Baseline-2 here) using analytical model are also included.

BFS per unit functional areal density is a measure of potential BFS resulting at a given weight. Lower numbers indicate superior performance. By this metric HCA-P1 with the AMH honeycomb has the best performance. However, since BFS is inversely proportional to areal density BFS per unit areal density will always be least for the heaviest inserts. Appropriate comparison metric is ΔBFS / ΔAD which represents how much BFS reduction was achieved with the incurred weight penalty with reference to the

lower areal density baseline. A higher number indicates superior performance. HCA-P2 with Al-CH has the best performance improvement with this metric.

General observation from visual imaging of water-jet cut vertical sections at the point of impact suggested the failure modes in the HB50 laminates reflect those observed for cross-plied fabric composites namely: (i) dual stage ply shear due to force localization, (ii) sequential delamination in the successive layers, and (iii) combined fiber elongation / pullout and fiber tensile failure. In the cross-plied laminates, fibers in the projectile facing plies are typically found to shear along the edges of the projectile indicated by a penetration cavity with the same size of the projectile's diameter (first stage). Consequently, the projectile deforms and undergoes petal-like stripping of the jacket and pancaking of the soft core projecting a larger diameter cross-section on the later plies. Failure of these plies is by shear combined with the listed types of fiber tensile failure.

The presence of honeycomb partially isolated the front laminate rear face bulging from the back laminate resulting in the reduced BFS. This is inferred from the difference in bulge curvature radius for these laminates. It delayed the time of interaction between the front laminate bulge, caused by progressing delamination during impact, and the back laminate. This created an isolation of the actual projectile arresting process within the front laminate from the armor rear face thereby reducing the concentration of transferred shock loads. The result was a reduction in observed BFS. These attributes suggest that the honeycomb may be behaving as a spacer. At the same time, participation of the honeycomb in energy absorption was confirmed from good agreement of the analytical fit with the experimental data. The honeycomb did not affect the energy absorption mechanisms in HB50 laminates, as the variation of laminate thickness failing in first

stage shear with velocity is identical for both insert types (Appendix 4). This hints towards a rigid plastic behavior of the honeycomb during impact, which is a common assumption made during analysis of conventional sandwich composites under projectile impact. Failure in the honeycomb layer was due to core crushing and shear in the immediate vicinity of the projectile zone with extensive plastic deformation by bending in surrounding areas. It is to be noted that average size of the impact zone on Al-CH was 35.4 cm^2, which is much less than that seen for AMH in [74].

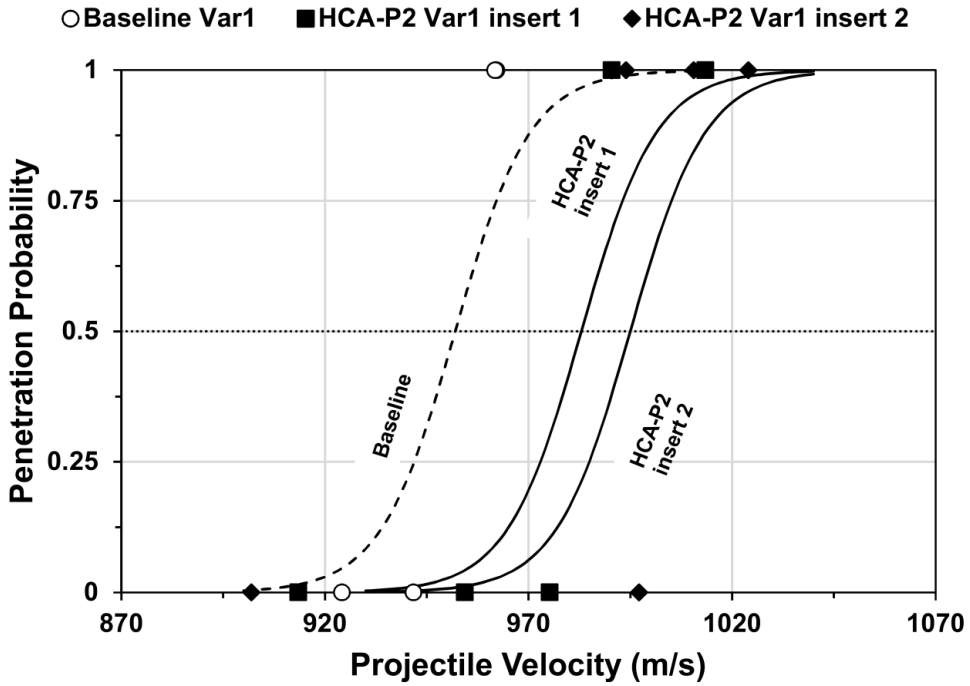

Figure 9 V_{50} representation for variant-1 baseline and HCA-P2 using Boltzman sigmoidal fit to the penetration probability versus velocity data.

Crush strength of the honeycomb appears to affect the extent of honeycomb participation in the energy absorption process. This can be due to restriction of the delamination process in the front laminate during impact by presence of a stronger

honeycomb layer at the laminate base arresting the membrane like bending of individual plies.

A summary of test results for V_{50} evaluation is presented in Appendix 2A. V_{50} for the inserts was calculated by taking the arithmetic mean of equal number of highest partial and the lowest complete penetration impact velocities from the data. V_{50} for variant-1 baseline and HCA-P2 inserts is represented using a Boltzman sigmoidal fit to the penetration probability versus velocity data and shown in Figure 9. V_{50} of all baseline and HCA-P2 variants were then plotted as a function of their areal density (Figure 10). The data agreed well with linear regression fits for both baseline and HCA-P2 insert types. Baseline and HCA-P2 of functional areal densities 14.5 and 15.7 kg/m^2 respectively were predicted using this linear model to satisfy the minimum V_{50} requirement of 847 m/s; the NIJ standard level III reference velocity. V_{50} of the baseline was found to exceed that of HCA-P2 until the transition point of 914 m/s, after which, the trend was reversed. The areal density of HCA-P2 corresponding to this point was termed the Critical Areal Density (CAD), as it was an indicator for the initiation of performance benefit of honeycomb inclusion. CAD for HCA-P2 was 17.34 kg/m^2 and corresponds to 13 mm thickness of the front laminate.

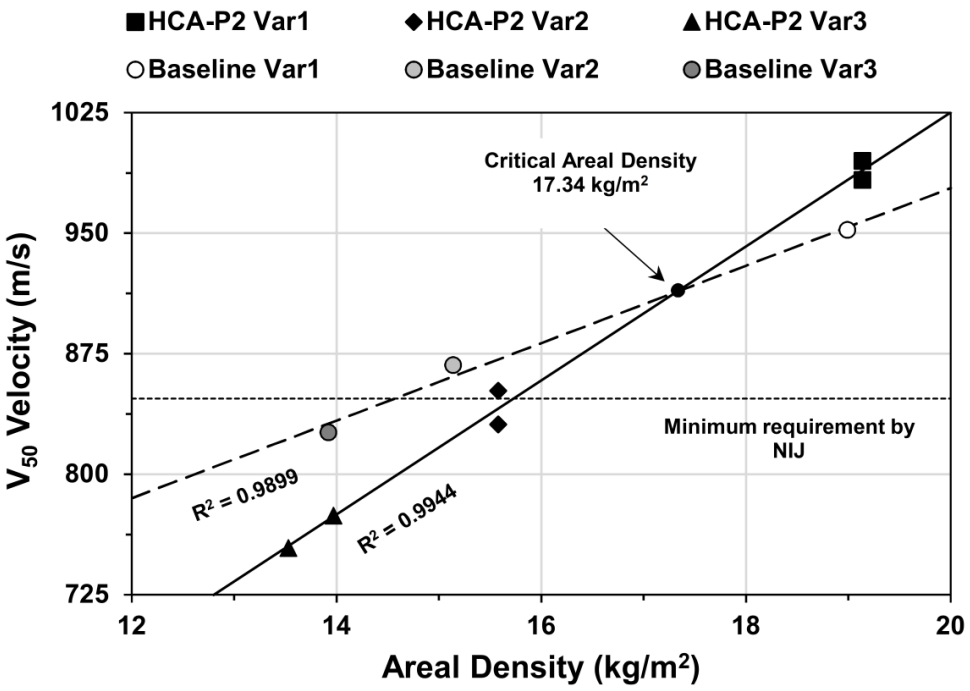

Figure 10 Plot of V_{50} of baseline and HCA-P2 variants versus respective functional areal densities. Minimum requirement by NIJ is shown. The Critical Areal Density (CAD) or the transition point beyond which V_{50} of HCA-P2 exceeds that of baseline is also indicated.

It can be inferred from the results that, below the CAD, monolith baselines will have better ballistic performance than HCA for the same areal density. Hence, as a design criterion for HCA, CAD should be the chosen parameter and not minimum areal density at which V_{50} meets the NIJ reference velocity. Since the V_{50} is a measure of penetration resistance of armor, the observed phenomenon can be explained by a consideration of involved mechanisms for the baseline and HCA-P2 inserts. Direct resistance to penetration for the honeycomb will always be minimal and lower than HB50 due to its geometric porosity oriented along the direction of projectile traverse. Therefore, in an event of front laminate penetration by the projectile in HCA-P2, any additional resistance will only be provided by the rear spall liner laminate. Al-CH cell walls will be sheared off and it will not undergo complete compression for maximum energy absorption to

occur. In contrast, when the same number of plies as the front laminate are penetrated in the baseline, more plies with areal density equal to that of the honeycomb and spall liner back laminate combined are available to offer higher penetration resistance. This in turn results in a higher V_{50} for the baseline. In summary, for a successful HCA-P2 design that has maximum utilization of the Al-CH's capabilities, it is imperative that the front HB50 laminate areal density is 17.34 kg/m^2 or higher. Inclusion of Al-CH does not allow reduction of the areal density of HB50 below the critical thickness. Its role in HCA was proven as a passive absorber.

Maximum projectile kinetic energy that can be exactly consumed by the target is at the V_{50}. The sum of the areal densities undergoing shear plugging and subsequent bulging is equal to the target areal density up to this impact velocity. Prediction of the transition point between these areal densities is a critical input for both the semi-empirical and analytical model used to estimate BFS earlier. It is represented in Appendix 1 by the ratio $R = t_s/t$, where t_s is the thickness of the target material undergoing shear plugging and t is the total target thickness. FSP impact experiments on HB26 by Nguyen *et al.* [77] demonstrated a dependence of this transition point on impact velocity as well as the total target areal density. Dependence on velocity is linearly proportional as an increase in velocity will result in more plies failing by shear plugging. Similarly, an increase in target thickness or areal density increases the flexural stiffness by a cubic relationship thereby causing more shear failure. Thus, mathematically, R has to represent both velocity and areal density simultaneously which is uniquely possible at V_{50}.

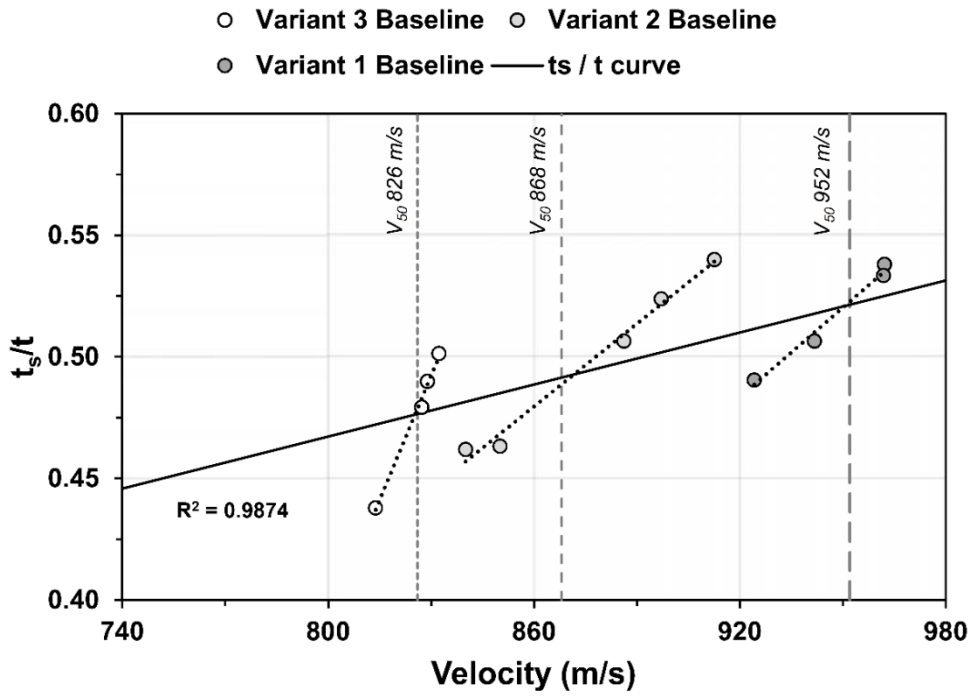

Figure 11 Shear plugging thickness ratio plotted as a function of velocity. Empirical relationship for the ratio is derived from the linear regression fit to the intersection data points between the thickness function and the V_{50} velocity for that insert.

The thickness of a target insert undergoing shear plugging is easy to measure from water-jet cut vertical sections of target plates at the point of impact as done earlier after preliminary testing. These measurements were taken for all baseline inserts used for V_{50} tests (Appendix 4) and were plotted as a function of impact velocity (Figure 11). The V_{50} velocity for each insert was then added to the plot. The ratio *R* is represented mathematically by the linear t_s/t regression fit to the intersection points between the thickness function and the V_{50} velocity of that insert.

A summary of test results for the HCA-P2 variants with level IIIA liners and the level III standard plate is presented in Appendix 2B. V_{50} for both HCA-P2 variants was calculated as done earlier. Complete penetration of the insert and not the back liner was considered for a probability of 1. V_{50} could not be calculated for the standard insert as no

instances of penetration occurred. The observed BFS values were plotted against velocity (Figure 12). BFS values for the HCA-P2 variant-2 inserts showed a reasonable correlation with velocity. This is indicated by the adjusted R^2 value of 0.9143 using the second order polynomial fit of equation 3.2. The limited number of data points available for the variant-3 insert did not make the use of this regression fit for BFS extrapolation practical. The variation observed for the standard level III Alumina ceramic based insert was extensive. An attempt to fit the second order polynomial curve to the data resulted in negative values for *A* and *B* coefficients which is physically incorrect (Appendix 1). Average of data values for shots above 800 m/s gives a BFS of 42.5 mm at 847 m/s for the standard insert.

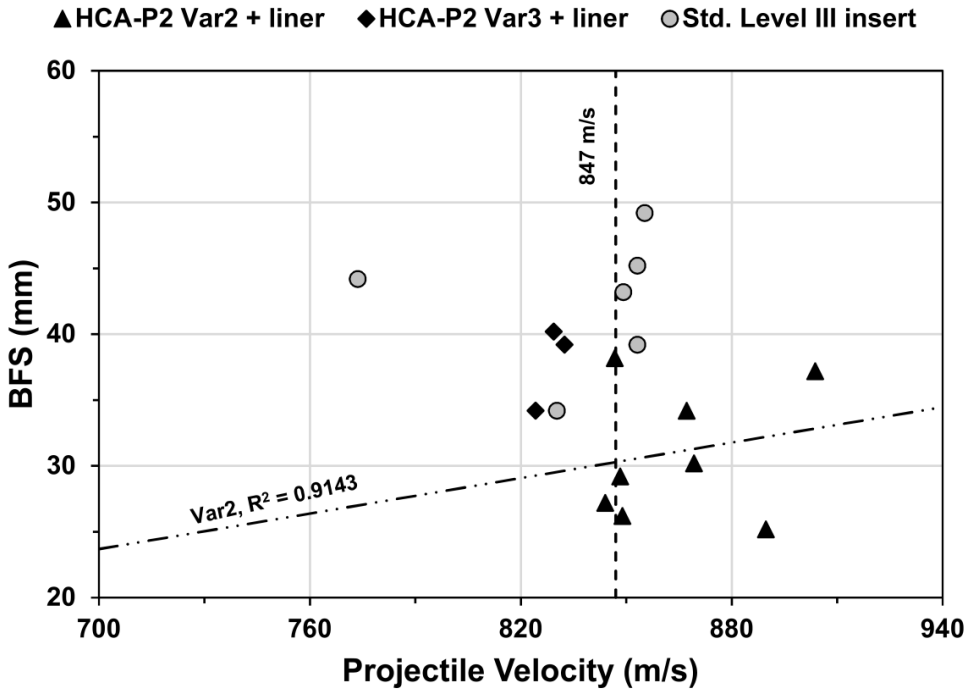

Figure 12 Plot of BFS measured from clay backing versus projectile velocity for the HCA-P2 variants with level IIIA vest liner and a standard Alumina ceramic based level III insert. Second order polynomial regression fit is used for the HCA-P2 variants. Error in velocity and BFS measurement was ±5 m/s and ±0.1 mm respectively.

V_{50} comparison with HCA-P2 variant-1 indicates its superiority in ballistic performance over both variant combinations (Table 18). Increasing the areal density of ballistic resistant material after the Al-CH layer offers no significant improvement in performance. The weight penalty incurred by use of the level IIIA liner offsets the BFS improvement for the variant-2 combination and the standard insert. The V_{50} calculation assumed complete penetration, if the insert rear face was breached but not of the liners. Comparing V_{50} for with and without liner (Figure 10) indicates minimal improvement, and the performance of baseline plates exceeds both cases. The addition of the liner layer does not affect the projectile defeat mechanisms suggesting similar extent of Al-CH utilization in defeating the projectile. This reaffirms the previous conclusion that honeycomb inclusion improves ballistic performance only when its areal density is higher than the CAD with a front HB50 laminate thickness of 13 mm or higher.

Table 18 Summary of BFS based comparison between HCA-P2 variant-1, and variant-2 and 3 with liner combination. The Level III standard insert is also included.

Armor type	BFS at 847 m/s		BFS/AD	ΔBFS / ΔAD	V_{50}	
	(mm)	% change	(mm per kg/m2)	(mm per kg/m2)	(m/s)	% change
HCA-P2 Variant-1	45.8	-	2.77	-	989	-
HCA-P2 Variant-2 combination	33.4	27.1%	1.32	1.4	870	12.0%
HCA-P2 Variant-3 combination	-*	-	-*	-*	835	15.6%
Level III standard insert	42.5	-7.2%	1.10	0.15	-	-

*BFS not estimated as reference velocity is higher than the insert V_{50}, †V_{50} could not be calculated as no instances of penetration occurred during testing.

A summary of results from Test 4 are in Appendix 2C. The temperature of the clay backing in the vicinity of the BFS location during test shots was recorded and measured BFS values were corrected to reflect desired clay temperature of 38°C (100°F).

Correction factors were derived from drop weight tests on the clay backing material. Details for the drop tests are in Appendix 3. Observed BFS values for the baseline inserts were plotted against velocity (Figure 13). The average size of the BFS diameter was 9.3 cm. Observed BFS values showed a good correlation with velocity. However, the slope of the BFS versus velocity trend was different than the analytical model prediction, suggesting material properties for these baselines were different than those tested during the preliminary test. A curve fitting method was used to derive the regression fit. A second order polynomial fit following equation 3.2 was used and showed a good agreement with the experimental data, as seen from the R^2 value. A BFS value of 50.1 mm was derived for the baselines at the reference velocity of 847 m/s using data interpolation with the regression fit.

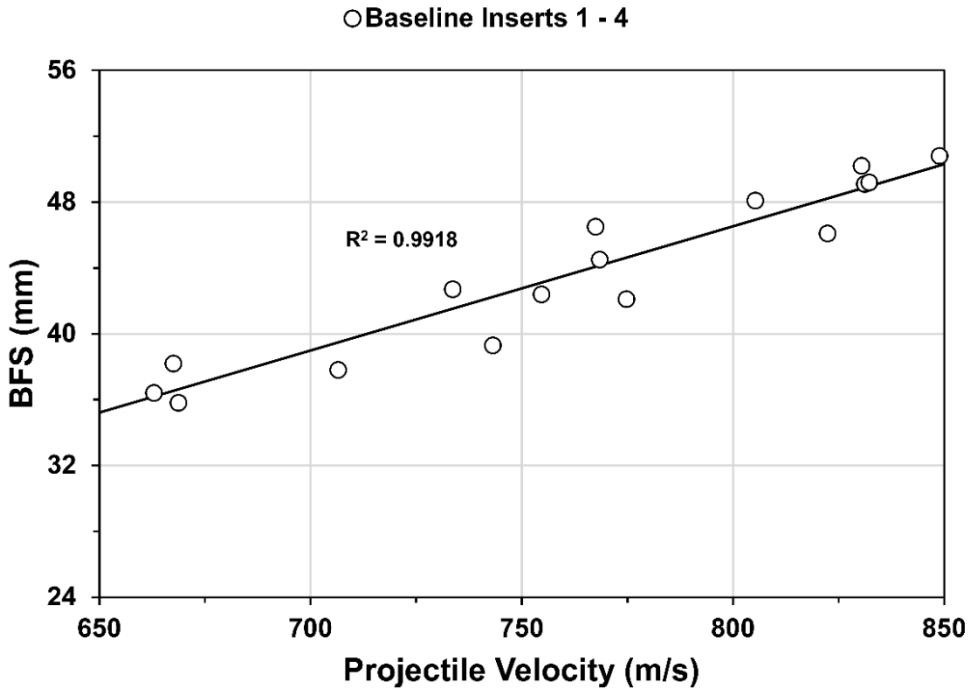

Figure 13 Plot of BFS measured from clay backing versus projectile velocity for the baseline inserts. A second order polynomial regression fit is overlayed with the test data points. Error in velocity and BFS measurement was ±5 m/s and ±0.1 mm respectively.

Similarly, BFS results variant-1, 4, and 5 inserts were plotted versus velocity (Figure 14). BFS values for all inserts showed good agreement with their second order polynomial regression fits as can be seen through the individual R^2 values. Confirming the test hypothesis, any change in energy absorption capacity (E_{hc}) of the honeycomb (due to a change in thickness, as in the present case) should cause a corresponding change in only the intercept coefficient *C*. Accordingly, a parallel transition of the regression fit should occur. This is true if the involved honeycomb is strain rate independent. From Figure 14, an apparent parallel transition does seem to occur between the baseline as well as the HCA-P2 variants, implying strain rate independence of Al-CH. However, a similar test for lower velocity regimes (giving lower strain rates for the honeycomb compression) will have to be conducted to confirm this observation. Also, if the change in honeycomb thickness is kept equal (2 mm in the present study between variant-1 and variant-4 and 5), an equal and proportionate transition of data regression fits should occur. This is confirmed from the results in Figure 14 and corroborates the physical relevance of the analytical scheme presented in Appendix 1. BFS values of 39.1 mm, 48.7 mm, and 30.2 mm were derived for variant-1, 4, and 5 respectively using data interpolation with the regression fit. The average BFS diameter for these inserts was 8.56 cm.

BFS versus velocity plot for NH based HCA-P2 variant-6, 7and 8 is shown in Figure 15. Once again, near parallel, equal and proportionate transition of data fits is observed similar to Al-CH based HCA-P2 variants for an equal change in included honeycomb thickness. This confirms the test hypothesis. BFS values of 39.2 mm, 45.4 mm, and 34.2 mm were derived for variant-6, 7, and 8 respectively using data interpolation with the regression fit.

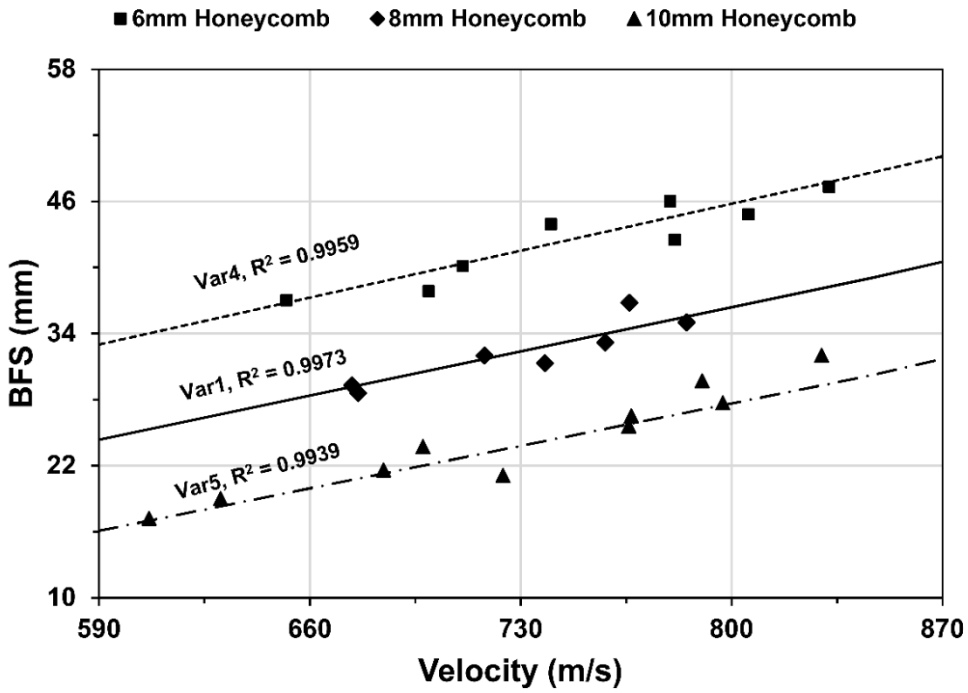

Figure 14 Plot of BFS measured from clay backing versus projectile velocity for the HCA-P2 variants with different Al-CH honeycomb layer thicknesses. Second order polynomial regression fits are overlayed with the test data points. Error in velocity and BFS measurement was ±5 m/s and ±0.1 mm respectively.

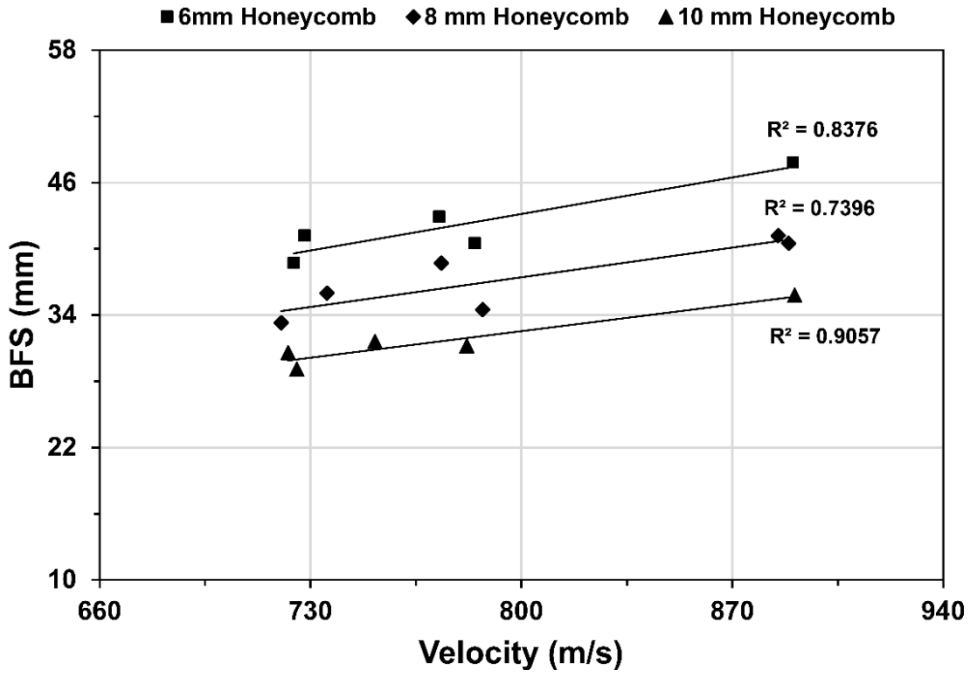

Figure 15 Plot of BFS measured from clay backing versus projectile velocity for the NH based HCA-P2 variant-6, 7, and 8 with different honeycomb layer thicknesses. Regression fits are overlayed with

the test data points. A near parallel transition similar to Al-CH based HCA-P2 variants is again observed. Error in velocity and BFS measurement was ±5 m/s and ±0.1 mm respectively.

Results from Test 4 are summarized in a BFS (at 847 m/s reference velocity) versus areal density combined plot for all tested inserts (Figure 16). BFS values for the preliminary test baseline are also included in the plot. Ideally the trend lines for Al-CH and NH based HCA-P2 data should converge to a point on the baseline plot as this point represents the front and back HB50 laminates together without any honeycomb. However, for practical laminates the plot can still permit direct performance comparisons. Benefits of the HCA-P2 design are clearly seen by the significant BFS reductions achieved from inclusion of honeycombs. Maximum BFS reduction was observed for variant-5 with 10 mm Al-CH which was 40.8% lower than that of a similar areal density baseline insert. Increasing the honeycomb thickness predictably improves the BFS reduction ability of the HCA. It is to be noted that the magnitude of the BFS reductions achieved exceeds the change in honeycomb thickness in each case further confirming that its participation in HCA is not only as a spacer. According to equation 3.1, NH with lower crush strength than Al-CH should demonstrate higher BFS values. Data indicates a possibility of this phenomenon for the 10 mm thick included honeycomb variants but not for the 6 and 8 mm honeycomb variants. More data points are needed to confirm the observation.

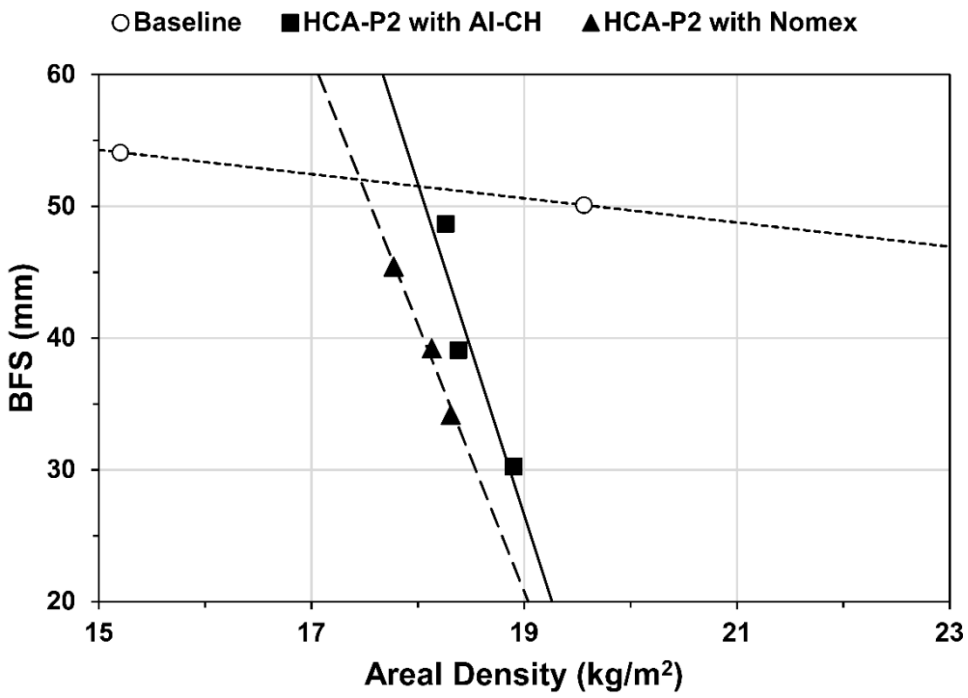

Figure 16 Summary of results from Test 4 shown as a BFS at 847 m/s reference velocity versus areal density plot. Advantages of honeycomb inclusion in ballistic performance are clearly indicated by the lower BFS values for all HCA variants in comparison to baseline HB50 inserts of same areal density.

This BFS for the 8 mm honeycomb variants is 23.6% lower than that of a similar areal density baseline insert. Percentage of BFS reduction achieved is much higher than HCA-P2 variant-1 from Test 1. The new fabrication process utilized for inserts in Test 4 clearly has improved inter-laminar shear rigidity. However, as seen from results in Appendix 2C this modification has potentially reduced the V_{50} of all HCA-P2 inserts, as penetration occurred for almost all impact instances above 860 m/s. Since the V_{50} for variant-1 HCA-P2 from Test 2 was higher than the baseline, the reduction in V_{50} is not due to honeycomb inclusion but due to the construction of the front laminate. This can also be corroborated by the fact that penetration velocities of 860 m/s or higher were almost identical and independent of the included honeycomb thickness. Compact bonding the laminates with the polyolefin based adhesive film increased the inter-laminar

shear strength but made inserts more rigid and prone to shear. Figure 17 illustrates the penciling effect seen in the HCA-P2 inserts through computerized tomography scan images of shot inserts. This is indicated by the localized dense concentration of the projectile fragments close to the line of impact. In comparison, the baseline insert demonstrates extensive spread of the fragments by undergoing delamination and resulting in no instances of penetration.

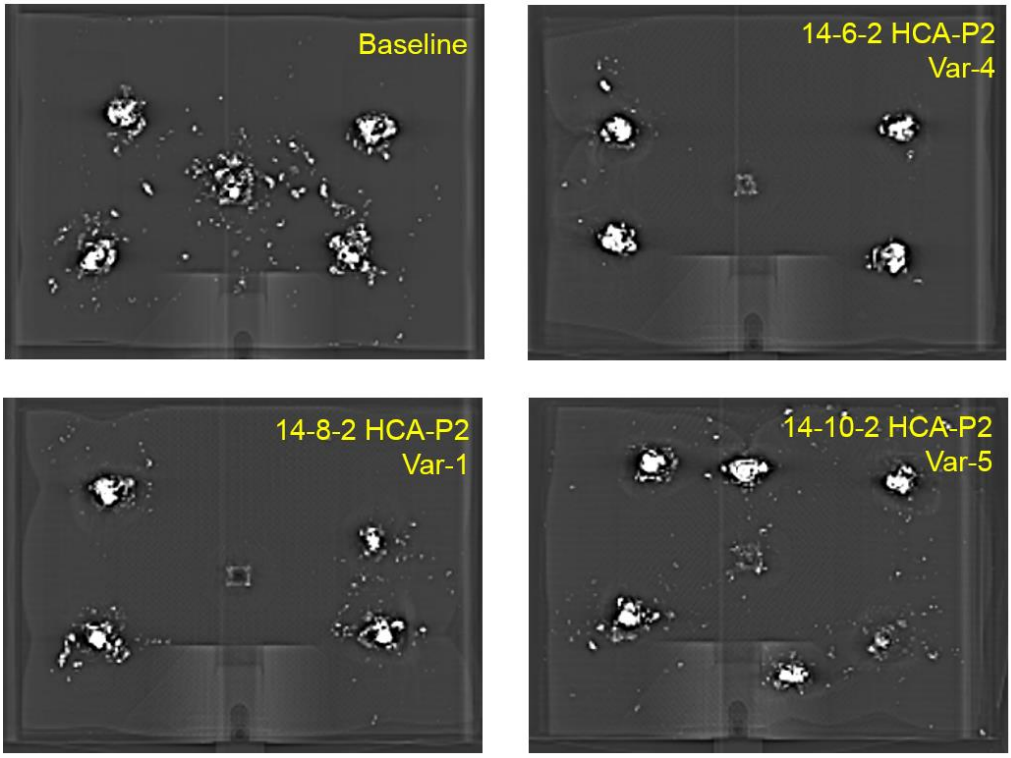

Figure 17 CT scan images of baseline and Al-CH based HCA-P2 inserts showing the extent of projectile fragmentation post impact. Baseline insert demonstrates fragments spread over a wider region compared to HCA-P2 where fragmentation is more localized and dense and close to the line of impact.

An increase in the extent of front laminate thickness undergoing shear plugging is evident from the t_s/t data in Appendix 4, also hinting toward a penciling effect. Consequently, the extent of honeycomb participation is also reduced as seen from the impact area diameter measurements which are almost identical for both honeycomb

types. The effect of crush strength on the size of impact area could not be studied. Information on a honeycomb thickness effect on the size of the impact area could not be obtained, which may provide valuable insights on its role in HCA. These will be part of future work.

The problem of increased shear plugging can be easily alleviated by retaining the original fabrication process for the front laminate allowing an increased membrane like behavior for the front laminate plies and increasing their resistance to shear. Rigid projectile impact experiments at high velocities on HB26 by Heisserer *et al.* [78] confirmed higher energy absorbed per unit areal density for thin targets than thick ones. Similarly, a study by Karthikeyan *et al.* [79] showed higher penetration resistance for HB50 than HB26 due to lower inter-laminar shear strength, facilitating individual ply response and maximum utilization of fibers via lamina stretching on impact. Delamination and lateral ply movement are crucial to maintain the penetration resistance of HB50 but are in principal opposed to the mechanisms of BFS reduction. Maximum improvement in performance can thus be realized if initial layers where shear failure is dominant are flexible and later layers where bending and bulging is dominant are rigid.

3.6 Conclusion

A new HCA prototype (HCA-P2) was fabricated with the inclusion of an aluminum honeycomb, selected as a replacement for AMH through mechanical property comparison under quasi-static and dynamic comparison. Ballistic tests were successfully carried out on variants of HCA-P2 to evaluate the role and influence of the honeycomb in the ballistic performance of the armor.

1. Preliminary test BFS results indicated superior ballistic performance of HCA-P2 compared to a baseline of similar areal density. Calculated BFS values from semi-empirical and analytical models developed in the study were in good agreement with the test data. A 7.1% reduction in BFS (hence BABT) was calculated using the analytical model based second order polynomial regression fit compared to the baseline monolith Dyneema® HB50 of same areal density. $\Delta BFS/\Delta AD$ calculations show improvement in performance for HCA-P2 compared to HCA-P1 and the baseline. Al-CH has higher energy absorbed per unit weight than HB50.
2. General observation of tested inserts suggest the failure modes in the HB50 laminates are identical to those reported earlier [74]. The presence of honeycomb appeared to partially isolate the front laminate rear face bulging from the back layer resulting in reduced BFS. Resulting isolation of the projectile arresting process from the armor rear face and reduced time of interaction between laminates decreased the concentration of transferred shock loads that cause BABT. Participation of the honeycomb in mechanical energy absorption without affecting performance of HB50 was confirmed by correlation of an analytical model to the experimental data. This suggests rigid plastic behavior of the honeycomb under impact, which is commonly seen for conventional sandwich composites in similar scenarios.
3. V_{50} for HCA-P2 variants were evaluated to verify if honeycomb inclusion allowed for a reduction in front laminate areal densities and hence the total areal densities of the armor. A plot of V_{50} versus areal density from the test results

indicated V_{50} for the monolith baseline HB50 inserts exceeded that of HCA-P2 up to a transition point, after which the trend reversed. This transition point was termed the critical areal density (CAD) with a value of 17.34 kg/m^2 (13 mm front laminate) and corresponds to a V_{50} of 914 m/s. Improvement in V_{50} by honeycomb inclusion above the CAD further corroborates higher energy absorption capacity per unit weight for Al-CH compared to HB50 in the bulging stage. Test data was also successfully used to derive the transition point for HB50 from shear plugging to bulging failure modes.

4. As a design criterion for HCA, CAD should be the chosen parameter and not only the minimum areal density that satisfies the NIJ V_{50} requirement. For the NIJ Level III example tested here, the honeycomb contribution to the projectile defeat mechanism of the HCA insert was optimal only when its front HB50 laminate was equal or greater than 13 mm, as indicated by the CAD.
5. HCA-P2 variants tested in combination with level IIIA liners did not show performance benefits. Increasing the areal density of ballistic resistant material after the honeycomb layer results in a weight penalty that offsets perceived BFS and V_{50} improvements. Results confirmed the previous test observation that the optimal honeycomb contribution in insert performance occurred only if the front HB50 laminate areal density was 17.34 kg/m^2 or higher.
6. Inserts with varying honeycomb thickness demonstrated a proportionate variation on their BFS performance. This was observed for both aluminum and Nomex™ based HCA-P2 inserts. Second order polynomial regression fits to the BFS versus velocity data showed a parallel transition of fits with the transition extent

consistent to the change in honeycomb thickness. These observations validate the physical relevance of the analytical model used to derive the second order polynomial regression fits. A significant BFS reduction was observed in HCA-P2 inserts compared to similar weight baselines. The magnitude of reduction exceeded the included honeycomb thickness proving their participation in HCA is not merely as a spacer. A 23.6% BFS reduction was observed for HCA-P2 with 8 mm included honeycomb, which is much higher than results from earlier tests. Maximum BFS reduction was observed for 10 mm Al-CH included HCA-P2 which was 40.8% lower than that of a similar areal density baseline insert. The improvement in performance was due to the revised fabrication process that improved the shear rigidity through inter-laminar shear strength of the HB50 laminates. The process however adversely affected the insert V_{50}. It was concluded that an optimum balance of laminate flexural stiffness is needed to promote the membrane like behavior in HB50 plies without increasing the BFS.

Experimental ballistic tests and results presented in this chapter offered a macro-mechanical insight in the behavior of the HCA and its potential to reduce BABT. The method used for design, testing, and obtained data can serve as a guideline for inclusion of other cellular solids in other hybrid armors and related protective structures. Evaluation of micro-mechanical data for BABT characterization through *in-situ* observation of the projectile defeat mechanism and time dependent properties like armor rear face velocity, its acceleration and stress wave impedance are difficult to conduct experimentally. This provides a motivation for the next chapter in which numerical

modeling by finite element analysis (FEA) is demonstrated as a tool to provide those results.

CHAPTER 4. PRELIMINARY NUMERICAL ANALYSIS OF PROJECTILE IMPACT ON HCA FOR PROCEDURE FAMILIARIZATION

4.1 Introduction

Advantages of finite element analysis (FEA) for simulating ballistic impacts on armor have been discussed in section 2.1.3. Capacity of any armor to defeat a projectile is highly dependent on the localized material response under rapid loading rates making far field considerations of lesser influence in the event. A micro-mechanical FEA of the impact event can provide vital insights on interactions of different materials, especially for multilayered armors like HCA. It is an effective means to substantiate experimentally established ballistic test results while providing additional understanding of involved critical time dependent properties that govern them. *In-situ* observations of individual layer performance under ballistic impact are not feasible experimentally. Visual results obtained from simulations could also be used to compare the damage distribution pattern and evolution of temporal back face bulge for multilayered armors like HCA which can only observed otherwise through difficult flash X-ray techniques and post-test CT scans. As mentioned in the introduction of Chapter 3, BABT manifests itself due to stress wave transfer and local acceleration of the underlying viscera. Acoustic impedance and stress

wave analysis for high velocity ballistic impact is extremely difficult to conduct using an experimental set-up, but feasible in FEA using certain assumptions [80].

Objective set for numerical analysis in the present study is to supplement the findings from the experimental investigation of performance influence of honeycomb inclusion in the HCA inserts under dynamic projectile impact. Desired outputs from the numerical analysis are the time dependent properties that can prove the performance improvement by use of honeycomb.

Feasibility and flexibility of the FEA scheme used in the present study was demonstrated in [10] through ballistic impact modeling of monolith steel plates by steel and copper projectiles. The FEA scheme was streamlined to address issues of excessive distortions, convergence problems, node penetrations, and warping of elements during the dynamic contact. Section controls, mass scaling, and material modeling options were explored to solve these problems. Resulting simulations were able to calculate the effect of model size and mesh dependency on numerical outputs derived from the analysis. Stress distributions, ballistic limits, and projectile velocity versus time plots were estimated from the nodal outputs.

An extension to these capabilities is explored in this chapter (from single plate to multiple plates, with or without spacing or inclusion of honeycomb layer). FEA simulations, being problem specific, do not have set procedures to ensure positive results. Hence, this chapter presents a preliminary analysis aimed at streamlining the adapted FEA scheme further, readdressing its procedural shortcomings, and identifying significant factors that affect simulation results. Simulated models presented in this

chapter have a progressive increase in complexity and computational load than those in [10] and lay the foundation of subsequently more complex model iteration in Chapter 5; serving as a guideline and ensuring a smooth transition in result fidelity.

General details of the FEA scheme are in section 4.2. Preliminary models with steel plates and copper projectiles are presented in the initial part of section 4.3. First preliminary model extends monolith steel plate impact by copper projectile to spaced plates. Second preliminary model extends the first model by inclusion of a honeycomb shell layer. Observed results and discussion is in section 4.4.

4.2 Finite Element Analysis (FEA)

Impact problems have been analyzed using finite elements with the basic objectives of numerically deriving ballistic limits of structures and also to visualize and compare their damage distribution patterns [18, 48, 81-83]. Referring to these listed publications as guidelines, the dynamic explicit simulations in ABAQUS® were designed for the current study.

4.2.1 Explicit 3D FEA

The explicit code in ABAQUS® works by direct computation of the dependent variables in terms of known quantities or provided inputs. An explicit dynamic analysis was also selected for the reason that it was computationally efficient and consistent for large models with relatively short dynamic response times, comparatively larger deformations, and large number of small time increments. This analysis system was also quite flexible and allowed for fixed or automatic time incrementation depending upon the requirement. The General Contact algorithm was used to formulate the contact between

the impacting projectile and the armor plates. This algorithm accounts for contact through element based surfaces that allows for material degradation. The classic erosion model in ABAQUS® was used to simulate the material damage response by individual element deletion as the damage parameter *D* reached unity. The software also allowed selection of post-damage-initiation material response and how failure evolved. Dynamic impact models for high velocity (>400 m/s) are prone to issues of excessive distortions, convergence problems, node penetrations, and warping of elements during the dynamic contact. Section controls, mass scaling, and material modeling options were used in the present study to solve these problems.

4.2.2 Model development

The primary components of the finite element model were the constituents of the target plate and the impacting projectile. The geometry of the impacting projectiles was modeled to exactly match the volumetric attributes of the 7.62 mm FMJ round. 3D dynamic FEA is computationally extensive due to the large number of elements, nodes, and integration points involved. Only a quadrant of the actual volume was considered owing to the axisymmetric nature of the problem enabling faster execution of the analysis procedure and solution computation time reduction (similar to [18, 83]). As the total time duration of the dynamic impact is in the order of 2×10^{-4} seconds, the choice of reduced volume does not affect the solution with wave propagation issues. The time duration also allows for neglecting friction effects on contact. Solid part meshes were created using hexagonal or hexagonal dominated elements (C3D4) and then structured and sweep mesh construction was done as required. For later simulations involving the cellular honeycomb, conventional shell elements (S4R) were used with wall thickness assignment

through section properties. Section controls were assigned to all elements in the models to control excessive distortion. The mesh was generated in discrete biased zones (denser in the contact region, coarser at the far edge to improve result quality without severely increasing computation time). The element sizes varied across the length of the plate model. Meshed parts were created to enable mesh surface generation required for the ease of element erosion. Necessary boundary conditions had to be evaluated and assigned to accurately model the field experiments. As only a quadrant of the entire volume was considered for analysis, the inside edge surfaces of the model were subjected to symmetry conditions along the X and Y axes. For the outer rear edges, their motion being completely restricted due to the test setup, a pinned boundary condition was chosen (Figure 18). Additional details on boundary conditions are available in [10]. Initial velocity assignment to the projectile was done by regulating the predefined field values. Values for velocity change with time were procured as an output through a node set near the center of mass of the projectile.

4.3 Simulated models for projectile impact

4.3.1 Preliminary FEA with plate spacing and aluminum honeycomb

Experimental test results suggest honeycomb inclusion in HCA isolates the front laminate from the back laminate during impact while absorbing energy resulting in BFS reduction. As a first step, pure spacing was created between steel plates and simulated for ballistic impact. The model was then modified to include an aluminum honeycomb layer in the spacing and simulated for impact.

4.3.1.1 Model details

First preliminary model evaluated effect of spacing on ballistic performance by comparing projectile velocity versus time plots for a monolith 6 mm thick plate with two 3 mm thick plates with spacing distance of 1.5 mm, 3 mm and 6 mm respectively.

Contribution of the honeycomb layer to the overall performance during ballistic impact was evaluated in the second preliminary model by comparing similar projectile velocity versus time plots and ballistic limits for with-honeycomb (6 mm steel + 8 mm Al-CH + 1 mm steel), spaced plate (6 mm steel + 8 mm spacing + 1 mm steel), and non-spaced plate (6 mm steel + 1 mm steel) configurations. Ballistic limit of each configuration was calculated using a plot of the impact velocities and the corresponding residual velocities post impact. Volumetric stress distribution plots were used to identify damage zone sizes for each configuration. Typical steps for model build up are shown in Figure 18.

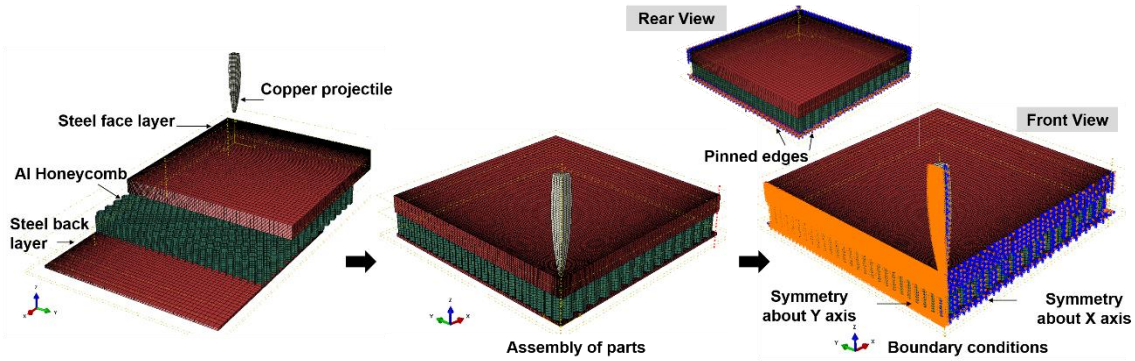

Figure 18 Steps involved in development of the FEA model are shown. Assembly of parts is followed by application of boundary conditions described in section 4.2.2.

4.3.1.2 Materials

For each preliminary model, OHFC copper projectiles were used. Lead was not chosen in the preliminary study due to the excessive deformation problems associated

with its use in high velocity impact FEA. Description of the issues faced is available elsewhere [10]. Choice of steel for front and back laminate was based on prior success in simulation. Properties for both OHFC copper and steel were taken from the ABAQUS user's manual [84]. The extended Shear and Ductile damage model was used for this steel while the Johnson-Cook plasticity and damage criterion was used for copper (see Section 2.1.3.1 in Chapter 2). Strain and strain energy based damage evolution was used for both these materials. Johnson-Cook plasticity and damage was also considered for aluminum. Material properties for Al 2024 were adopted [85].

4.4 Results and discussion

FEA scheme adopted in this study was successful in simulating ballistic impact for both preliminary models. Simulations were able to compute projectile velocity versus time plots during the period of impact and predict the residual velocity after penetration for all simulated configurations. The time period for this plot corresponds to the contact time of the projectile with the components of the armor plate. Results from the first preliminary model with varying spacing distance are presented in Figure 19. Increasing the spacing distance appeared to decrease the residual velocity — an indication of improvement in ballistic performance, qualitatively similar to the observations from the experimental results. An 11% decrease in residual velocity was observed for a 4X increase in the spacing. However, no significant change in rear face peak stress and rear face deflection was seen in the simulated spaced configuration. This is contrary to the observations from experiments and suggests that a pure spacer is not adequate to achieve BFS reduction.

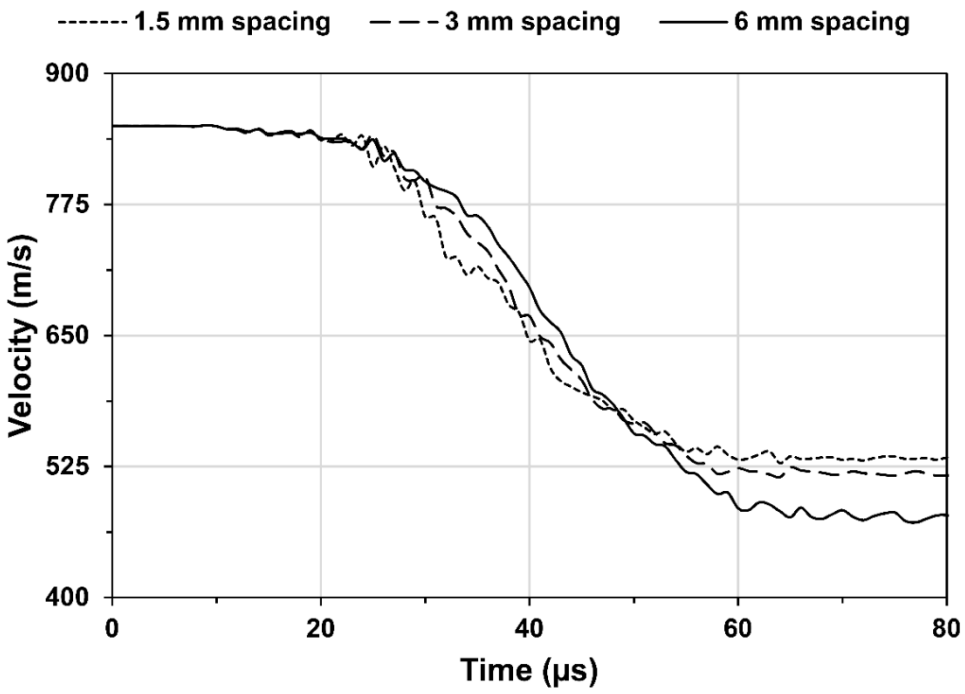

Figure 19 Projectile velocity versus time plot for increasing plate spacing computed from the first preliminary model.

For the second preliminary model, a similar comparison of the residual velocities for with-honeycomb, spaced plate and non-spaced plate configurations was obtained through the projectile velocity versus time plots. Such a plot for the with-honeycomb configuration is shown in Figure 20. The plot indicates that the ballistic limit of the with-honeycomb configuration is 650 m/s. Similar results were computed for the spaced and the non-spaced configurations. The summary of the results is shown in Figure 21 in the form of Lambert-Jonas curves for ballistic limit. The residual velocity gives an indication of the amount of kinetic energy absorbed during the deformation process. Results show no significant variation in performance between the configurations (< 7.5%). The extent of variation observed from the first preliminary spaced plate simulation was not replicated here.

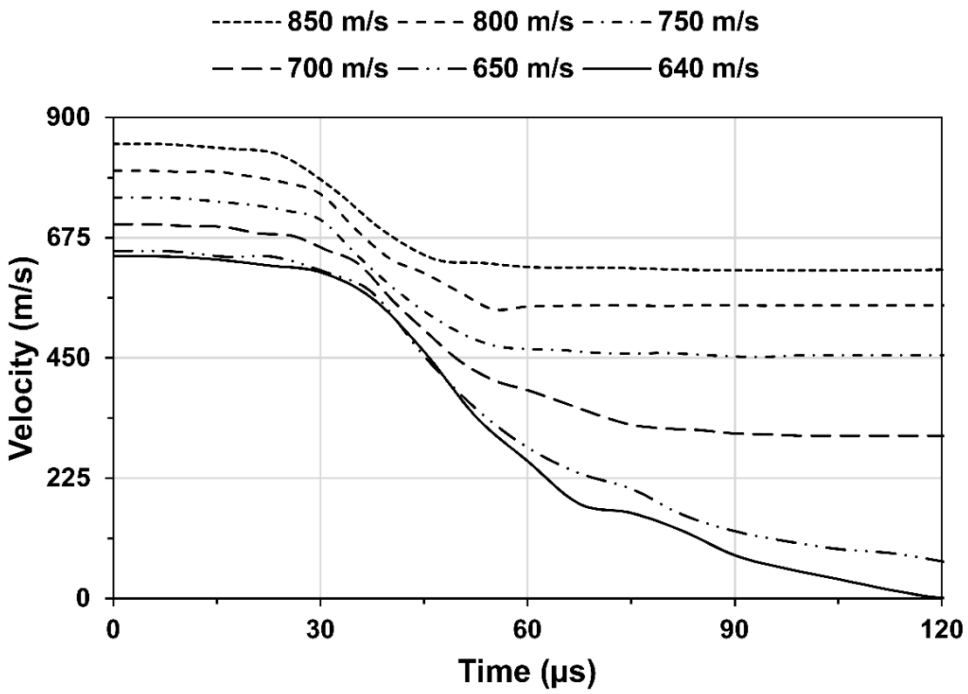

Figure 20 Projectile velocity versus time plot for with-honeycomb configuration from the second preliminary model.

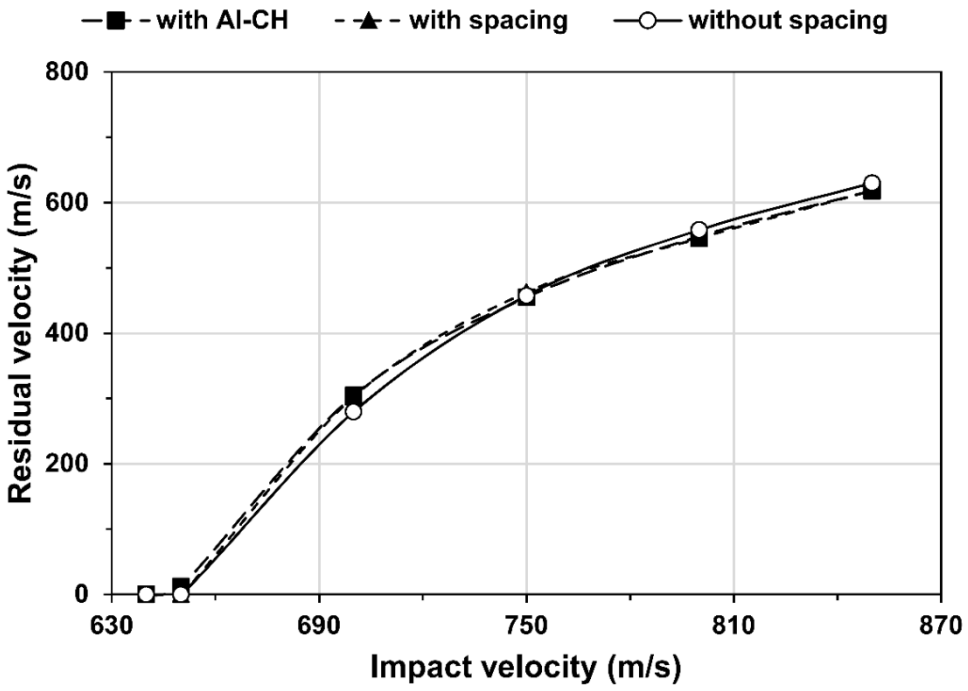

Figure 21 Ballistic limit prediction from velocity versus time plots for the with-honeycomb, with-spacing and without-spacing configurations using Lambert-Jonas curves. No significant change is observed.

The trends observed in all the change in velocity plots shown in Figure 20 show no specific discretization in slope of the curve based on resistance to perforation. This is due to the high magnitude of impact velocities considered in this study (>640 m/s) and smaller plate thicknesses; resulting in minimized interaction time between plate and projectile. Typically, impact at low velocities for thin face sheet high thickness honeycombs sandwich plate would result in three discrete zones in the change in velocity plots.

Experimental testing provides limited information concerning damage evolution and the process of projectile penetration during the impact. FEA simulations were able to provide information on these aspects through 3-D visualization of volumetric stress field distributions. This proves an effective way to compare the size of the damaged area for all individual components of the target plate.

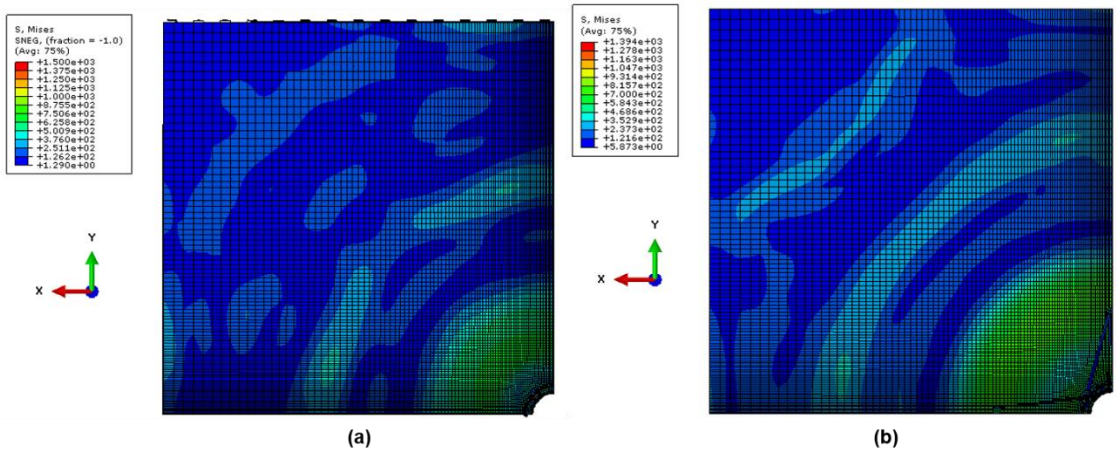

Figure 22 Stress distribution in the back layer at 850 m/s and 100 µs after impact; (a) with-honeycomb configuration, (b) non-spaced configuration.

The stress distribution versus time history for the backing layer is an indicator of the communication of stresses through the thickness of the target plate. Delayed stress

transfer and minimized damage zones enable minimizing the BFS as well as the corresponding BABT. Figure 22 shows the stress distribution observed in the backing steel layer for the with-honeycomb and non-spaced configurations at time interval of 100 μs at 850 m/s impact velocity. The size of the damaged zone observed in the with-honeycomb configuration is smaller than the non-spaced one, similar to what was observed in experimental testing of the HCA-P2.

This was also indicated by the through-thickness damage evolution observed from volumetric stress distribution plots at increasing time increments for each configuration. Sample volumetric plots for the with-honeycomb plate are shown in Figure 23. Results from the present FEA are in agreement to those by Ivanez *et al.* [86]. Observations made from change in velocity plots, ballistic limits, and 3-D volumetric stress distribution plots portray similar trends for the impact characteristics of the aluminum based collapsible absorber core they presented.

Visual results from the current modeling procedure do not clearly match the expected damage zone sizes seen experimentally on HCA-P2. This difference can be attributed to the use of steel face and backing layers in the current model instead of UHMWPE. Since steel is isotropic, a high through thickness modulus results in localization of damage before the projectile interacts with the honeycomb layer. Resulting bending creates separation between the laminates and the honeycomb. Not more than three honeycomb cells were seen to undergo compression and are in extended contact with the laminates. In the case of HCA-P2, delamination in the front HB50 laminate causes honeycomb compression over an approximate area of about 30X its cell size.

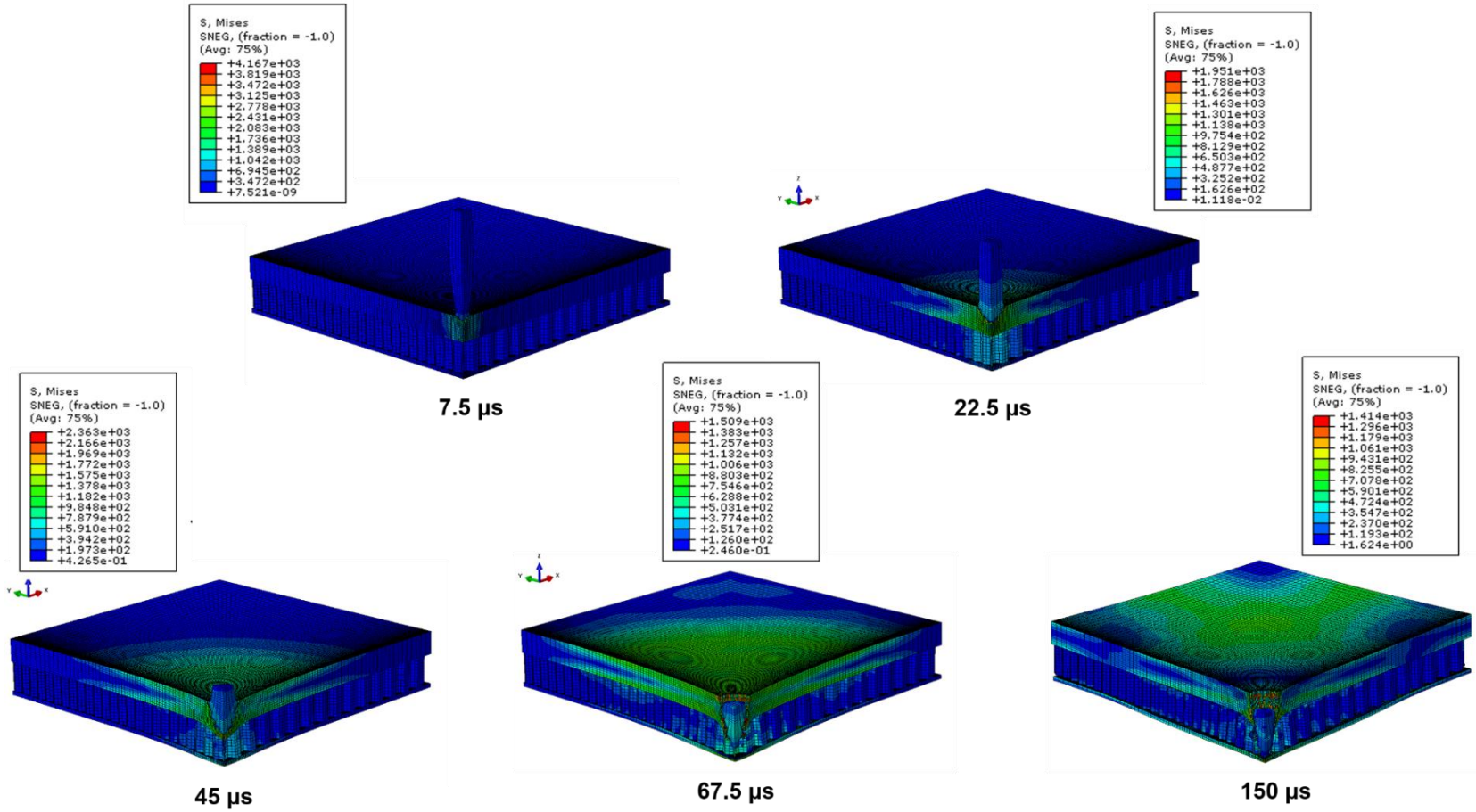

Figure 23 Volumetric stress distribution plots for the with-honeycomb configuration at varying time increments (impact velocity 640 m/s).

The reduced number of interacting honeycomb cells in the current FEA has led to minimal kinetic energy absorption by the honeycomb layer. This is evident through negligible change of residual velocity in comparison to non-spaced plates.

4.5 Conclusion

A preliminary FEA was developed using dynamic explicit code in ABAQUS® to evaluate the influence of a honeycomb layer on the ballistic performance of the armor plate.

1. Verification of performance improvement by inclusion of a honeycomb layer was also done through FEA in ABAQUS®. Three configurations (with-honeycomb, spaced-plate, non-spaced) were subjected to ballistic impact simulations by a copper projectile. Change in velocity plots and ballistic limit predictions from obtained results did not indicate high variation as expected by honeycomb inclusion. A 2.3% reduction in residual velocity was calculated for the with-honeycomb configuration in comparison to the spaced plate one for the high velocity regime (impact velocity >750 m/s). Verification of residual velocity as a function of plate spacing was also carried out for this high velocity regime. An 11% decrease in residual velocity was observed for a 4X increase in the spacing. Further numerical investigations can confirm and elaborate on this dependence.
2. The stress distribution versus time history for the backing layer was used an indicator of the communication of stresses through the thickness of the target plate. The size of the damaged zone observed in the with-honeycomb configuration was smaller than the non-spaced one, similar to what was observed in the experimental testing of the

HCA-P2. This delayed stress transfer and minimized damage zones indicated minimizing of the BFS as well as the corresponding BABT.

3. Discrepancies in the FEA scheme were identified from the preliminary models. Localization of damage by inclusion of steel as well as high velocity and interaction time kinetics appear to have a significant influence on the observed results. Limited participation of the honeycomb seen in the preliminary models as separation of layers occurred. Incorporation of adhesive in the model is necessary to alleviate this issue.

CHAPTER 5. NUMERICAL INVESTIGATION OF HONEYCOMB PARTICIPATION DURING DYNAMIC PROJECTILE IMPACT ON HCA

5.1 Introduction

Preliminary numerical analysis was successful in demonstrating the flexibility of the adopted FEA scheme to accommodate increased complexity in the dynamic impact simulation with inclusion of spacing and honeycomb layer. Results from this effort were able to indicate the ballistic performance influence of these inclusions to a limited extent. It was observed that participation of the honeycomb in the ballistic impact event can be increased by incorporating inter-layer bonding via adhesives. Reducing damage localization by considering more pliant actual cross-ply composite material instead of steel could also potentially alleviate the issue. This will be the focus of the preconceived more complex simulation iteration than the preliminary models and presented in this chapter. Outputs of interest from the simulations include:

a. time dependent: change in displacement, velocity, and acceleration of insert rear face, through-thickness stress distribution, delay in stress wave arrival at rear face,
b. time independent: extent of kinetic energy absorption, BFS, peak stress at rear face, maximum delamination damage area, observed failure modes along each layer.

Based on the simulation results from the preliminary models, the FEA scheme was adapted to include actual HCA-P2 materials: HB50 laminates with inter-ply bonding, and Al-CH. Successful implementation of this scheme would set up a reference method that can be followed to verify influence of other factors on the ballistic performance of HCA.

5.2 Material constitutive models

5.2.1 Dyneema® HB50

HB50 composite laminates are fabricated by hot pressing cross plied stack of monolayer plies and have a fiber volume fraction of 82%. Available volume fraction of the matrix material and high fiber-matrix strength offset results in lower inter-laminar bond strength than in-plane ply strength. Consequently, mechanical response of these orthotropic laminates under a complex loading scenario, such as a projectile impact, has to be numerically analyzed on a ply-to-ply level. A discretized-ply composite part generation method is thus adopted in Chapter 5 instead of a homogenized one used in Chapter 4.

Ballistic impact on armors FEA is a three-dimensional stress state analysis which requires a composite failure prediction model that can capture both in-plane and inter-laminar stress components. In-built composite models available in ABAQUS® neglect out-of-plane tensile and shearing stresses and are only suitable for a 2D plane-stress analysis. Hence, a user defined 3D material model was implemented through a virtual user material (VUMAT) subroutine to capture these stresses. The subroutine uses Hashin's failure criteria for a fiber constitutive model and Puck's action plane theory for the matrix material (see Section 2.1.3.2 in Chapter 2). Results from the preliminary FEA

in Chapter 4 highlight the requirement to include delamination and individual layer bonding to facilitate adequate interaction of the honeycomb during the impact process. Element based cohesive zone modeling (CZM) with quadratic traction-separation rules was used for both inter-ply and inter-layer delamination.

A review of most recent publications on numerical analysis of high velocity ballistic impacts on armors having UHMWPE as a constituent material indicate partial success. Grujicic *et al.* [83] and Burger *et al.* [51] applied material user subroutines for UHMWPE in their continuum composite models. The model scheme adopted in [83] was able to correlate the calculated BFS bulge diameter evolution during impact with experiments but was unable to retain similar accuracy for the BFS bulge depth or the extent of delamination. Similarly, the model adopted in [51] was able to match the energy absorption capacity of HB25, but had under prediction of BFS and it was unsuccessful in simulating delamination. Krishnan *et al.* [50] used an in-built material model from the commercial software code for their simulations. Although the modeling scheme and use of cohesive elements captured delamination, the BFS was under predicted by about 50%. Material properties used for UHMWPE were adjusted to match the penetration response but not corroborated using other mechanical tests. Present study aims to combine advantages perceived from these publications by mating the chosen Hashin-Puck VUMAT subroutine with the discretized part geometry having CZM.

3D stress tensor with a cross-ply composite laminate schematic is shown in Figure 24a illustrating the directionality of the stresses with respect to the laminate co-ordinate geometry. Directions 1 and 2 (represented by x_1 and x_2) are aligned in-plane with the 0° and 90° plies in the laminate respectively, whereas, direction 3 (represented by x_3) is

aligned out-of-plane with the laminate and is the direction of the projectile impact. Figure 24b shows a water-jet cut cross-section image of a ballistic tested HB50 laminate with prominent deformation and failure modes from the projectile impact. This cross-section image is considered to be aligned along the x_1-x_3 plane with perpendicular direction x_2 as the normal to the plane of the paper. The co-ordinate system for the VUMAT subroutine and the element based CZM follows this exact orientation and is a reference to all material properties listed in this section.

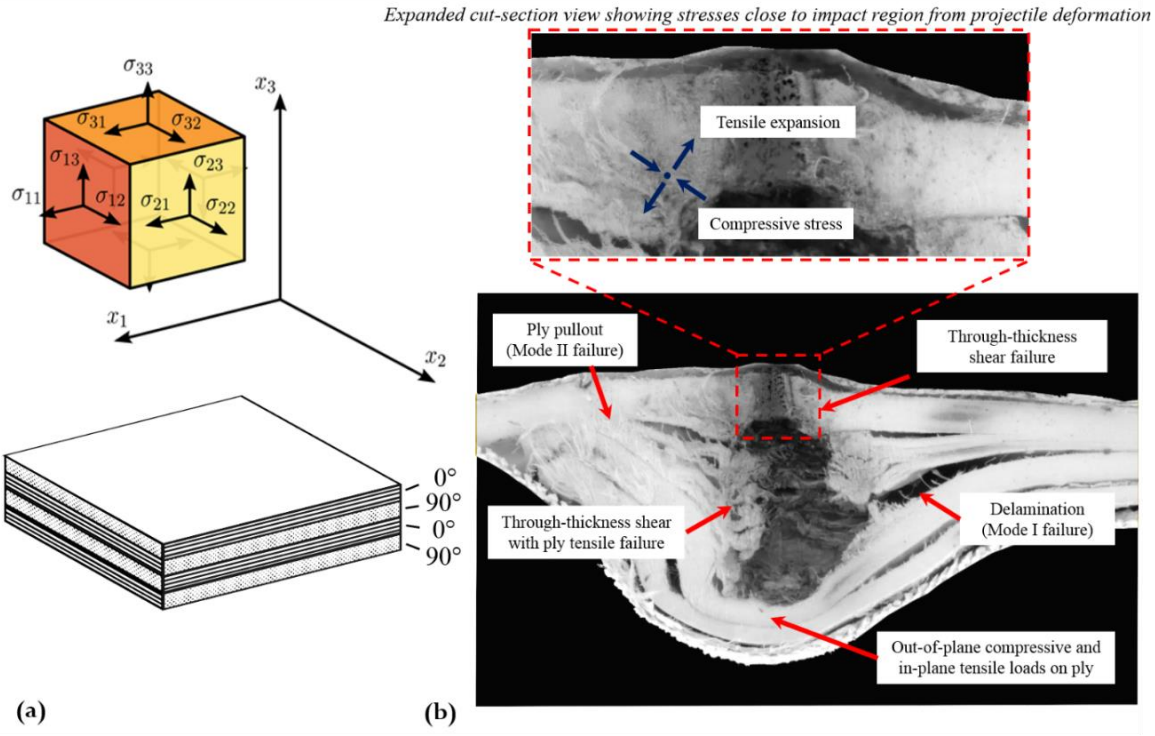

Figure 24 (a) Schematic of a 3D stress tensor with a cross-ply laminate shown to illustrate the direction of stresses with respect to the laminate co-ordinate geometry; (b) cross-section image of a ballistic tested HB50 laminate shows prominent deformation and failure modes from the projectile impact.

5.2.1.1 HB50 laminate material properties for VUMAT

Uniaxial quasi-static in-plane tensile response of cross-ply HB26 and HB50 laminates was evaluated experimentally by Karthikeyan *et al.* [87]. Both laminate types exhibited near identical tensile strengths of ~780 MPa. This could be due to the same SK76 fiber system common to both laminates types and accounting for 83% volume of the composite. The specimen used for the test were customized to have wider gripping areas with a bolting arrangement and narrow gage width to negate sample slippage (inter-ply shear and pull-out within the grips), which is a persistent problem for UHMWPE composites (due to high fiber tensile strength, low shear strength and low coefficient of friction). An independent investigation by Lassig *et al.* [88], who adopted the same test specimen geometry, has also corroborated the observed peak tensile strength for HB26.

ASTM D3039 standard for uniaxial tensile testing of composites recommends specimen geometry to ensure failure occurs within gage length and that specimen cross-section has adequate fiber count to suitably represent the bulk material. A typical minimum specimen geometry as per the standard is rectangular, with 25 mm width and 2.5 mm thickness for cross-plied composites. The customized sample geometry used in [87-88] had a reduced gage cross section area (less than half, 4 mm width and 6 mm thickness) than the minimum standard recommendation; to avoid slippage. The authors confirmed test validity based on observed failure modes in the post-test specimen. Since neither study presents data variation for multiple cross-section sizes, it is difficult ascertain if measured response correlates to bulk properties. Cutting specimen to such small dimensions from larger laminates may introduce pre-test damage or exacerbate edge effects that can then result in a premature failure response. Russell *et al.* [89] has

shown a significant decrease in measured strength from single fiber to a $[0/90]_{48}$ laminate for HB26 (~3.8 GPa for single fiber and ~780 MPa for the laminate) which they attribute to differences due to processing route. They conclude practical laminates display tensile strengths in agreement with yarn strengths as tested by rollers (~2.2 GPa).

Present study considers an average laminate tensile strength of 1.5 GPa for the numerical analysis. Similar estimate was also used by Attwood *et al.* [90] for their numerical study. Average elastic modulus for HB50 from the referred experimental data was 61 GPa. HB26 yarn tensile data in [89] at varying strain rates suggests no strain rate sensitivity for strain rates up to about 10^3 s^{-1}. Again, since HB26 and HB50 have a common SK76 fiber system, we assume no strain rate dependence for HB50.

Quasi-static tensile response of HB50 laminate in the ±45° orientation was also evaluated in [87]. ASTM D3518 is referred for such a test which provides the in-plane shear properties of the composite (direction 12, Figure 24). As the dominant failure mode in the composite during the test was matrix shear, a low strength high ductility response was observed as compared to uniaxial tension test. Measured shear modulus was 300 MPa with peak shear strength of 1.6 MPa. Again, the standard recommends test specimen dimensions to be identical to ASTM D3039, which was not the case in the study, and may have resulted in under-prediction of strength as less cross-section area was available for load bearing. This is evident from data presented for HB26 in [87] and [88] for this test. Specimen with gage geometry close to the ASTM standards was used in [88] for tests and a peak strength twice higher than in [87] was reported. Moreover, double-notch specimen shear tests from [87] indicate a significant strain rate dependence in matrix dominated mechanical response. The study reports data at only two strain rates making

prediction of extrapolation models difficult. A peak strength of 77 MPa is therefore assumed in this study [51]. Shear failure in direction 12 is not prominent during ballistic impact and is expected to have minimal influence on the numerical analysis.

Through-thickness shear behavior (direction 13 and 23, Figure 24; identical as HB50 is orthotropic) in cross-ply Dyneema® laminates is fiber dominated due to their high volume fraction. Conventional Losipescu test setup as per ASTM D5379 is permissible for use only for flexurally rigid composites that allow for fiber shear or matrix cracking at quasi-static strain rates. Such a test setup cannot be used for relatively pliant cross-ply Dyneema® laminates as they are more prone to bending than shear. A new test configuration was presented in [88] to evaluate through-thickness shear behavior for HB26. Observed average shear modulus was 31 MPa. Failure was not seen from the tests as the test setup was limited in maximum achievable displacement to avoid collision between loading arm and fixed support. An alternate method to evaluate shear failure stress is by Depth of Penetration (DoP) impact tests with rigid projectiles like FSPs [77-78]. Mechanical behavior of thin plates is different than that of thick plates under DoP impact tests. Thin plates show a coupled bending-shear failure with a more membrane like response (single stage), whereas, thick plates show shear failure followed with delamination and extensive bulging (two stage). At a certain intermediate thickness, failure behavior transition occurs between thin and thick plates as demonstrated in [77]. Ideal scenario for measuring through-thickness shear failure stress would be a partial penetration by a rigid projectile in a plate with thickness corresponding to this transition point. In doing so, energies associated with bending, compressive flow, delamination, ply tension and bulging, and shock induced heating can be neglected. A perforation by shear

model presented in [77] assumed complete conversion of projectile impact kinetic energy in to work done in forming shear plug due to penetration by pure transverse shearing, can then. As per the model:

$$\frac{1}{2}\, m\, V^2 = \tau_{max} \pi r_p DoP^2 \tag{5.1}$$

where, m is the projectile mass, V is the projectile velocity, r_p is the projectile radius, and τ_{max} is the through-thickness shear strength. Average effective shear strength of 560 MPa was reported for HB26 using Equation 5.1. Kinetic energy versus DoP data for HB26 under steel sphere impact was also presented for two areal densities. Applying equation 5.1 to this data results in a higher average effective shear strength of 700 MPa for the thicker laminate. As a first approximation, average effective shear strength of 630 MPa is used here for HB50.

Out-of-plane compressive response of Dyneema® composite laminates was matrix dominated and found to be sensitive to specimen length and thickness [90]. As seen from the shear tests, matrix dominated material properties of these composites are also strain rate sensitive. Peak nominal compressive strength of 1600 MPa and modulus of 10 GPa for HB50 is used in the present study. Similarly, it is expected the out-of-plane tensile response will also be size and strain rate dependent. An extrapolated peak nominal tensile strength of 10 MPa is used [88].

Poissons' ratio values for HB50 were not available experimentally and were assumed as 0.1 for the VUMAT. Summary of all material properties for the VUMAT subroutine are in Table 19.

Table 19 Material properties for HB50 virtual user material subroutine.

Required Property	Value	Units
Density	980	kg/m^3
Young's modulus along direction 1	61	
Young's modulus along direction 2	61	GPa
Young's modulus along direction 3	10	
Poisson's ratio 12	0.1	
Poisson's ratio 13	0.1	
Poisson's ratio 23	0.1	
Shear modulus in 1-2 plane	0.3	
Shear modulus in 1-3 plane	0.031	GPa
Shear modulus in 2-3 plane	0.031	
Coefficient for stiffness proportional damping	1.00E-09	
Tensile failure stress in direction 1	1500	
Compressive failure stress in direction 1	64.3	
Tensile failure stress in direction 2	1500	
Compressive failure stress in direction 2	64.3	
Tensile failure stress in direction 3	10	MPa
Compressive failure stress in direction 3	1200	
Shear strength in 1-2 plane	77	
Shear strength in 1-3 plane	630	
Shear strength in 2-3 plane	630	

5.2.1.2 Inter-ply material properties for element based CZM

Cohesive Zone Modeling (CZM) is mesh-relative. The traction separation rules used to define the cohesive behavior depend upon the length measures of when unrecoverable damage initiates (crack length δ_0) and the point where complete failure occurs (crack length δ_f). Elastic response of the bonding material is then defined by the slope of the linear elastic traction separation curve which is the effective initial material stiffness per unit area (K_{eff}) and given by:

$$K_{eff} = \frac{T_{ult}}{\delta_0} \tag{5.2}$$

where, T_{ult} is the effective ultimate nominal stress of the bonding material. It is to be noted that T_{ult} is not the ultimate stress of the bulk version of the bonding material but a parameter that defines the behavior between the bonding material and bonded material pair. The effective elastic modulus E_{eff} is then related to K_{eff} via:

$$E_{eff} = K_{eff}\ h_{eff} \tag{5.3}$$

where, h_{eff} is the initial geometric thickness of the solid cohesive element from the mesh. Damage initiation was modeled by quadratic stress behavior which assumed damage to initiate when a quadratic interaction function involving the nominal stress ratios for the normal and shear modes reaches a value of one. This criterion can be represented as:

$$\left(\frac{T_n}{T_{ult\ I}}\right)^2 + \left(\frac{T_s}{T_{ult\ II}}\right)^2 + \left(\frac{T_t}{T_{ult\ III}}\right)^2 = 1 \tag{5.4}$$

where, each bracketed term represents the ratio of the actual nominal stress to the ultimate nominal stress for each mode. A damage evolution law was used to describe the rate at which the material stiffness is degraded once the corresponding initiation criterion is reached. The dependence of the fracture energy G_C on the mode mix was defined based on a power law fracture criterion. The power law criterion considers failure under mixed-mode conditions to be governed by a power law interaction of the energies required to cause failure in the individual modes. It is given by

$$\left(\frac{G_n}{G_{C\ I}}\right)^{\lambda} + \left(\frac{G_s}{G_{C\ II}}\right)^{\lambda} + \left(\frac{G_t}{G_{C\ III}}\right)^{\lambda} = 1 \tag{5.5}$$

where, each bracketed term again represents the energy ratio for each mode similar to the damage initiation criterion. The power exponential λ was taken as 1 in this study. Properties of the HB50 bonding matrix required for CZM not entirely available in published literature. Only preliminary tests have been done thus far. Evaluated material properties were at quasi-static strain rates and show significant strain rate dependence. Data from Mode I DCB test as per ASTM D5528 published by Lassig *et al.* [88] and Mode II double notched shear test published by Liu *et al.* [91] were used to derive properties required for CZM. Properties for Mode III have been approximated to those of Mode II. They are summarized in Table 20.

Table 20 Material properties for cohesive zone model used for inter-laminar behavior of HB50.

Required Property	Value	Units
Density	1026	kg/m^3
Effective elastic stiffness per unit area, Mode I	20	
Effective elastic stiffness per unit area, Mode II	20	GPa/m
Effective elastic stiffness per unit area, Mode III	20	
Maximum nominal stress, Mode I	5	
Maximum nominal stress, Mode II	5	MPa
Maximum nominal stress, Mode III	5	
Mode I inter-laminar fracture toughness	790	
Mode II inter-laminar fracture toughness	1460	J/m^2
Mode III inter-laminar fracture toughness	1460	

5.2.2 Aluminum honeycomb

Aluminum 2024 material properties were used for the corrugated honeycomb in the preliminary FEA as the Johnson-Cook parameters for this aluminum grade were available in published literature. Numerical simulations of a honeycomb compression test were conducted to verify if the resulting honeycomb response was close to the actual experimental results (as per ASTM C365M-05). FEA model for this test was based on the

numerical modeling scheme by Aktay *et al.* [92] to evaluate honeycomb crush behavior. Honeycomb was modeled using shell elements similar to the preliminary FEA and was dimensionally identical to the samples used for experimental compression test. Compression platens were modeled as rigid bodies. Compression loads were applied on the honeycomb structure using motion of the upper compression plate through displacement amplitude that corresponded to 10^3 s^{-1} test strain rate. High strain rate of compression was chosen for faster computation time. Comparison with the quasi-static experiment is still fair since Al-CH demonstrated no strain rate sensitivity during ballistic testing as shown in Chapter 3. Bottom plate had fixed non-movable boundary conditions. Contact between platens and the honeycomb as well as within the honeycomb itself upon initiation of plasticity was modeled using general contact algorithm with self-contact definitions. Contact penalty was enforced through friction coefficient of 0.4. Schematic of the simulated test setup in is Figure 25a. An alternate method to simulate honeycombs is by applying crushable foam material model to a homogenous solid section. This approach is typically used in very large models where honeycomb micromechanical behavior is irrelevant to primary objective of the numerical simulation. The crushable foam model takes direct honeycomb property inputs and was included in this exercise to confirm the fidelity of the modeling scheme. Shell element based honeycomb underwent cell wall folding and collapse during compression similar to the experimental test sample (Figure 25b).

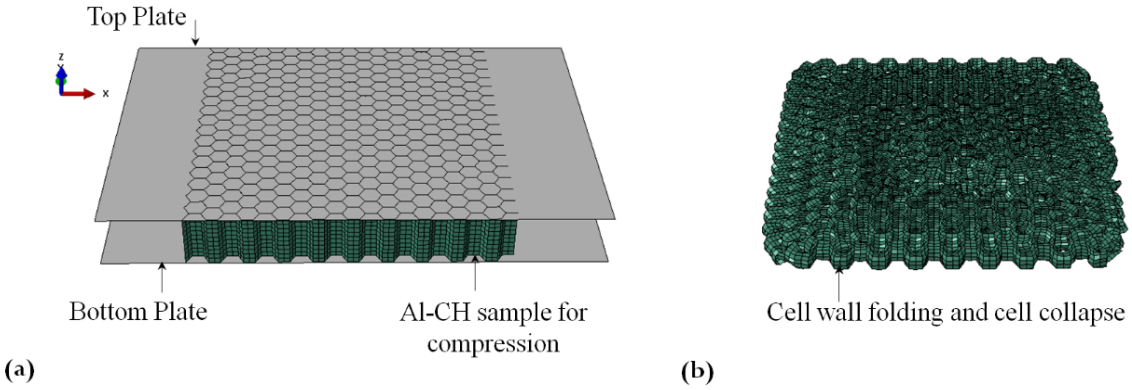

Figure 25 (a) Schematic of the honeycomb compression test setup modeled in ABAQUS®. Compression plates were modeled as rigid bodies. Shell element based model used for the aluminum honeycomb. (b) Honeycomb after compression has crushing failure through cell wall folding and cell collapse.

Stress versus strain curve from experiment and simulation of crushable foam model show good agreement (Figure 26). Magnitudes of peak and average crush strength are as specified in the technical data sheet by the manufacturer. However, the shell honeycomb response shows gross over prediction. It was found that decreasing the magnitude of yield strength and the strain hardening coefficient (parameters *A* and *B* in equation 2.3) brought the plastic response of the honeycomb closer to that of experimentally evaluated. Best correlation was observed when the base material was considered as elastic-perfectly plastic with yield stress of 165 MPa. No transition from peak to crush strength was observed due to lack of micro-inertial effects. However, potential change in the energy absorption capacity of the simulated honeycomb due to no transition would be minimal and not affect the honeycombs participation in sandwich composite scenarios like in present study.

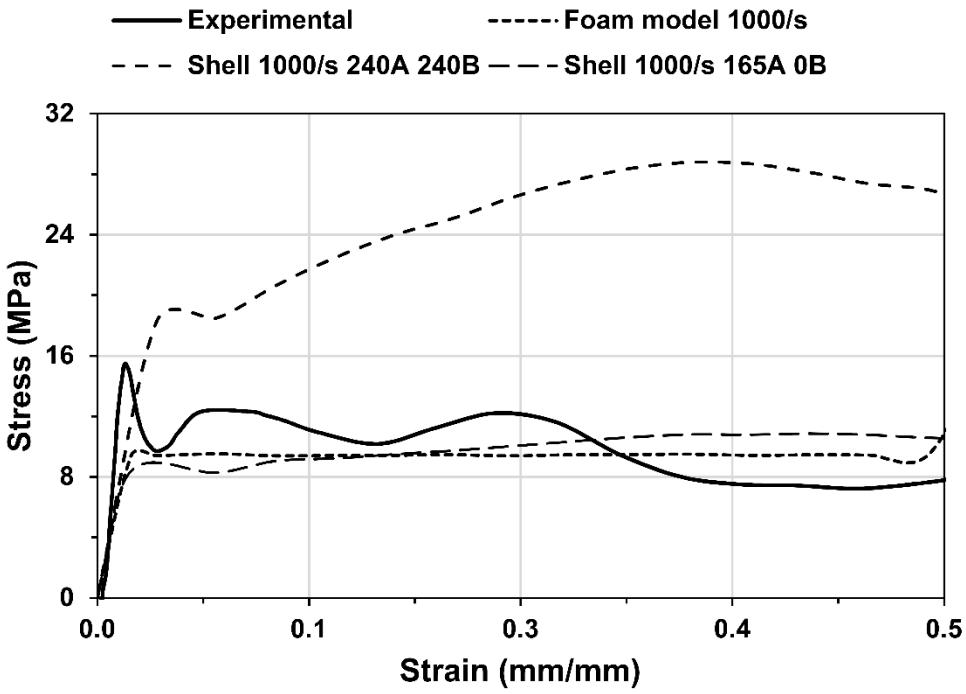

Figure 26 Stress versus strain plot for aluminum honeycomb. Results from numerical simulation show good agreement with experimental values. Material properties used in preliminary FEA over predicted the honeycomb behavior. Decreasing the magnitude of yield strength and strain hardening coefficient of the base material improved the correlation between numerical and experimental response.

5.3 Simulated impact model for wave impedance analysis

BABT manifests itself due to stress wave transfer from the local point of impact on the armor to the underlying tissue. The rear of the armor deforms at high velocities and accelerates underlying viscera locally causing tissue shearing. Delaying and attenuation of the propagating stress waves by generating wave impedance via inclusion of a honeycomb layer can thus reflect as performance improvement. Preliminary FEA was aimed at testing this hypothesis but had limited success due to reduced participation of the honeycomb. As a solution to this issue, the preliminary model was revised to now include the actual HB50 composite with inter-layer bonding through CZM in a new FEA model. The model generation process, orientation, projectile geometry, contact

assignment, applied boundary conditions and predefined field was identical to the preliminary model where a quadrant of the actual insert was simulated for impact. Individual solid HB50 plies and inter-ply solid cohesive zone was created from a single part using the partition tool. VUMAT and CZM material models detailed in the previous sections were implemented for these discrete parts. Similarly, use of shell element based honeycomb for Al-CH was continued here from the preliminary model but with refined material properties derived earlier. Material properties for brass jacket and lead core were taken from [46] and are listed in Chapter 2 Table 5. In addition to the node set on the projectile for procuring velocity values, an additional node set was also created on the insert rear face to get time dependent outputs listed at the beginning of the chapter. Schematic of the baseline model assembly is shown in Figure 27.

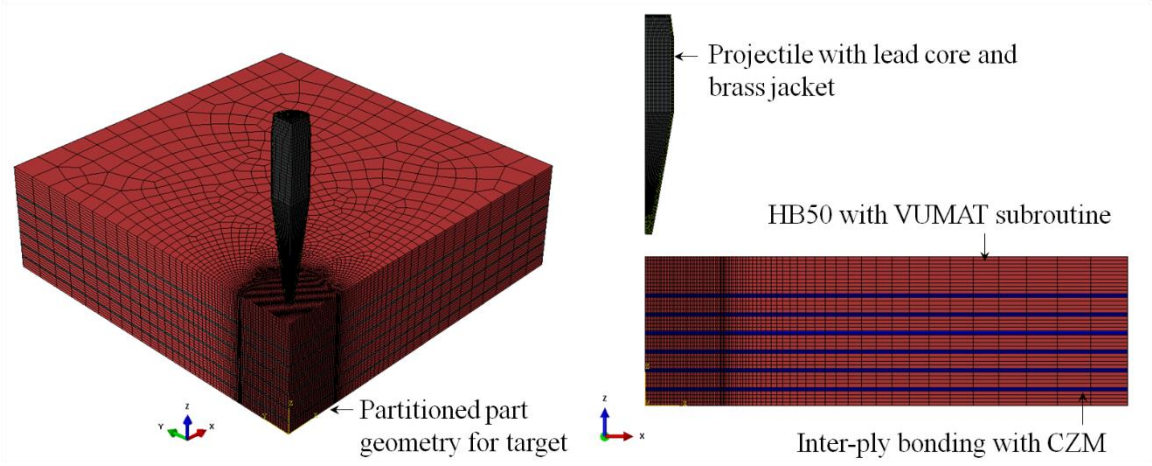

Figure 27 Schematic of baseline model assembly with part details. Target portioned to create individual HB50 plies and modeled with VUMAT subroutine. Inter-ply bonding achieved by CZM.

Execution of the high fidelity FEA model was not successful due to limitation in VUMAT subroutine available. Mesh refinement, model size and involved complexity resulted in an initial stable time increment on the order of 10^{-12} seconds (giving ~10^{8} increments per microsecond during analysis) and non-convergence. Single precision of

the VUMAT subroutine resulted in error round off and caused severe node penetrations. Excessive distortion of elements occurred even with mesh refinement to an element size of 0.2 mm. Deformation speed exceeded wave speed due to high impact velocities which led to premature termination of the analysis. Modifying the VUMAT subroutine code was beyond the scope of this study and can be attempted as a part of future work. However, a qualitative comparison between baseline and HCA was still feasible for a non-penetrative soft impact scenario at lower velocities similar to the foam impact experiments done in [87]. FEA of such scenarios can allow evaluation of time dependent outputs and stress wave propagation analysis set as the study objective.

Stress wave propagation analysis for multilayered armors is complex as impact events produce planar-shear, spherical-shear and dilatational wave fronts, which are typically non-planar. Gama *et al.* [80] have presented a stress wave propagation analysis that assumed a planar wave front for the through-thickness stress wave close to the impact centerline. A similar stress wave propagation analysis was conducted by using the nodes along the impact centerline. Baseline model assembly used for the analysis was identical to that shown in Figure 27. The 7.62 bullet projectile was replaced with aluminum foam (trade name Alporas) of 15% relative density. Diameter of the projectile was 40 mm with 30 mm length. Material and size of the projectile was specifically chosen to ensure minimal distortion of elements on contact while achieving a linear wave front in the target region directly in the line of impact. Properties for the Alporas aluminum foam ware taken from [93] and applied with crushable foam plasticity model available in ABAQUS®. Mesh sensitivity analysis was conducted for the projectile and eventually element size of 0.5 mm was chosen. Node set was created on the back face of the target

to retrieve displacement, velocity and acceleration variation with time. For HCA-P2, 8 mm thickness shell honeycomb model was incorporated within the HB50 laminates. Thickness of the front laminate was reduced HCA-P2 to match the cumulative areal density to that of the baseline for effective one-to-one comparison. Honeycomb bonding to HB50 laminates was enforced using tie constraints. Projectile impact velocity was reduced to 250 m/s in order to resolve issues with excessive element distortion and node penetrations. Schematic of the model is in Figure 28a.

5.4 Results and discussion

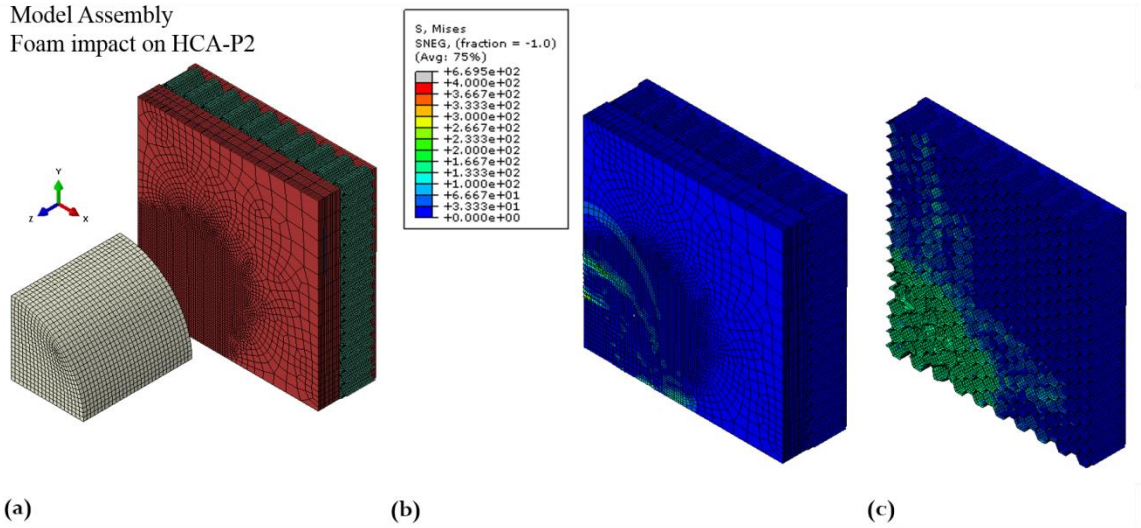

Figure 28 (a) Schematic of HCA-P2 model assembly for the foam impact simulation is shown. (b) Stress distribution on the front laminate top face is shown at the point of impact. Magnitude of peak stress was determined from nodes within the impact zone. (c) Stress distribution in the honeycomb is shown 10 µs post impact. Plastic deformation in honeycomb is by cell wall folding and cell collapse similar to compression test FEA.

Revised foam projectile impact model with VUMAT and CZM was successfully executed. Computation time for baseline and HCA model was about 48 hours with parallel execution on 16 cores. Increased participation of the honeycomb during impact was observed. Shock induced delamination occurred in the front laminate along the line of impact due to compressive stress wave reflectance as tensile. Velocity versus time

plots and ballistic limits for the projectile were not evaluated as the FEA was inherently of non-penetrative nature. An alternate metric used for comparison was extent of kinetic energy absorbed by means of plastic deformation in both inserts. Normalized energy absorbed through plastic deformation with kinetic energy was plotted as a function of time (Figure 29).

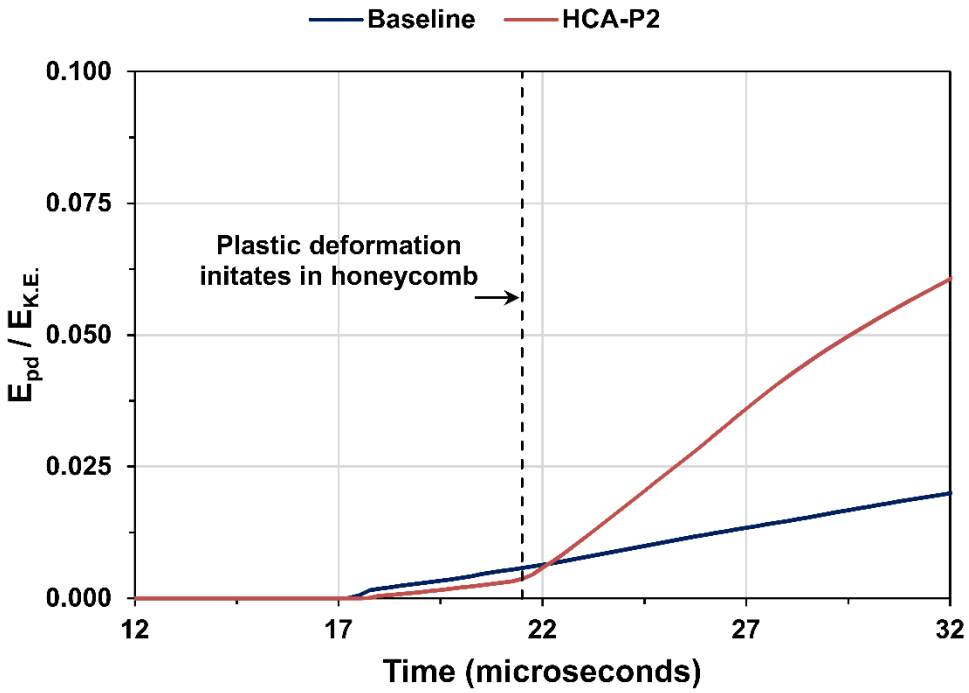

Figure 29 Normalized energy absorbed by plastic deformation with kinetic energy plotted as a function of time. Plot indicates significant increase in energy absorbed by HCA-P2 after plastic deformation initiates in the honeycomb.

Since projectile does not penetrate on impact, observed plastic deformation is physically synonymous to the later instances of the bulging stage where there is intact translation of plies along the line of impact. Experimental results have shown honeycomb to be most effective in such a scenario and absorbs more energy than an equal weight HB50 laminate. This observation is also corroborated from Figure 29. Cumulative energy absorbed by plastic deformation higher in HCA-P2. Discretization is observed in the

slope of the normalized energy plot for HCA-P2 with transition occurring at the point of plastic deformation initiation in honeycomb. Plot slope is similar for both baseline and HCA-P2 till the transition point, which indicates proportionate energy absorption by HB50 in both cases. Inclusion of honeycomb did not affect energy absorption mechanisms in HB50 similar to the inference from ballistic tests. Magnitude of normalized energy absorbed at a given time before transition is slightly lower in HCA-P2 as included areal density of HB50 is lower than baseline (corresponding to the areal density of added honeycomb). Energy absorbed in HCA-P2 increases much rapidly after initiation of plastic deformation in honeycomb. This effect was more pronounced in FEA than experiments in Chapter 3 as impact was simulated by a larger diameter cylindrical projectile resulting in near-uniform vertical load distribution on the honeycomb and over a wider area.

Isolation of stress fields in the front laminate was again seen in HCA-P2 as in preliminary FEA. Stress distribution in the front laminate top face is shown at the point of impact in Figure 28b. Plastic deformation in honeycomb occurred by cell wall folding and cell collapse indicating predominant uniaxial compression. Stress distribution in honeycomb 10 μs post impact is shown in Figure 28c. Through-thickness normal stress (σ_Z) in the back face of the target was made non-dimensional by normalizing with the maximum compressive stress (σ_{Zmax}) developed close to the point of impact in the front laminate and plotted as a function of time for comparing stress transfer in baseline and HCA-P2 (Figure 30). A delay in arrival of peak stress was seen in HCA-P2 by the inclusion of honeycomb. Amplitude of the peak compressive stress impulse in baseline was higher than that in HCA-P2. It was inferred that honeycomb inclusion increased

stress wave impedance by demonstrating more than 50% reduction in shock loads for the current impact scenario. A corresponding decrease in peak sternal force can thus be expected which correlates to a reduction in BABT.

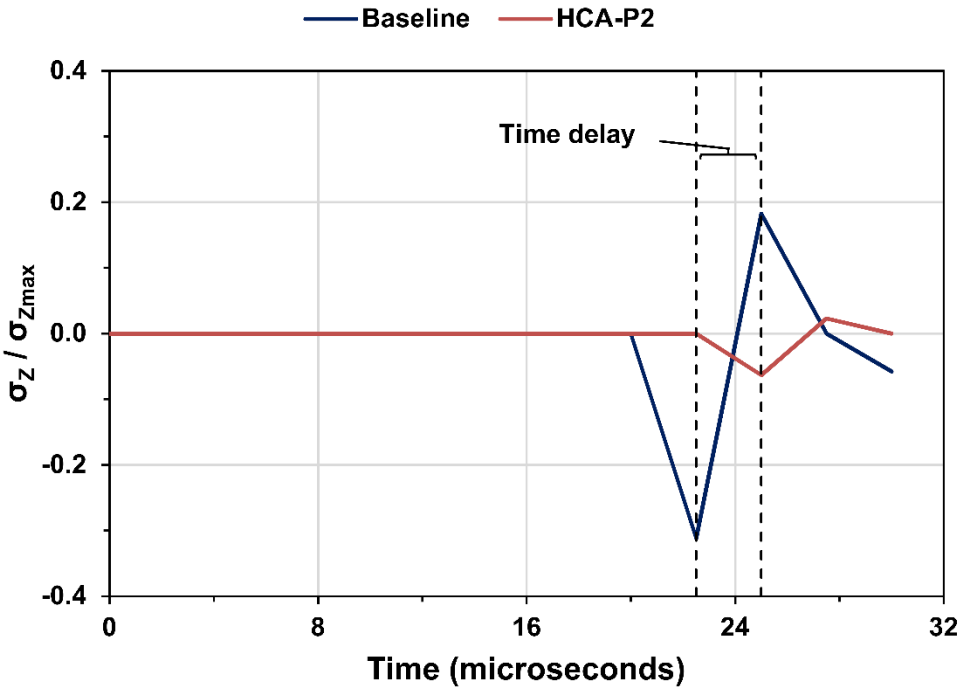

Figure 30 Normalized stress in the back layer plotted as a function of time. A delay in the time of arrival of peak stress in the back layer is seen for HCA-P2. Amplitude of the stress impulse is more than 50% lower by inclusion of honeycomb resulting in reduced shock loads and therefore potential reduction in BABT.

Similarly, time delay was also seen in displacement, velocity, and acceleration of central region of the impact zone in HCA-P2 back laminate. This is summarized in a time-history plot of these variables for baseline and HCA-P2 at foam impact velocity of 250 m/s (Figure 31). Significant reduction in the displacement magnitude projects a higher flexural stiffness in HCA-P2 and lower BFS. The extent of reduction is again more pronounced than ballistic experiments due to the simulated blunt impact and larger area participation of the honeycomb.

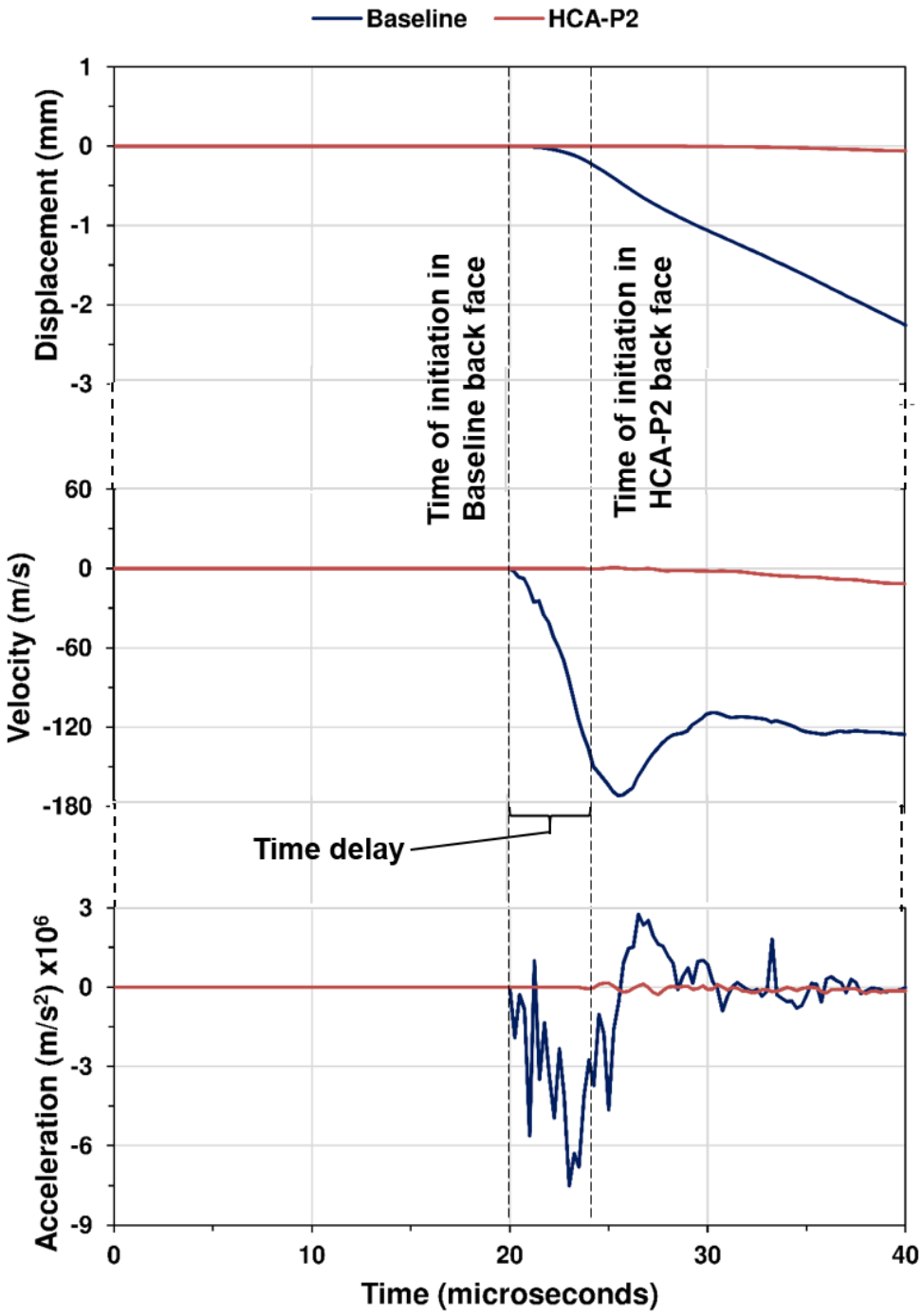

Figure 31 Time- history plot of displacement, velocity, and acceleration of the back laminate for baseline and HCA-P2 at foam impact velocity of 250 m/s. Difference in the time of initiation of these parameters between baseline and HCA is termed as time delay. Negative values indicate compression.

Reduced back face velocity and acceleration with incurred time delay indicate a slower distension of the back face than the baseline which may reduce the propensity of viscous injury occurring in the underlying viscera of the chest cavity. Inferences derived from FEA of foam impact at 250 m/s were not altered by varying impact velocity. Increasing the yield strength of the honeycomb base material and height of the honeycomb further reduced normalized stress in the back layer. Changes in the time dependent variables from Figure 31 were minimal and difficult to gauge. Overall, foam impact FEA was able to highlight the potential performance benefits that can be achieved by honeycomb inclusion by gauging pertinent parameters linked to BABT. Successful execution of actual 7.62 NATO ball projectile impact FEA can follow the same method presented here while accounting for penetration mechanisms and enable a direct comparison of injury tolerance criteria hard limits (Table 9) with those evaluated numerically. Predicted ballistic limits and BFS can then be compared to experimental data from Chapter 3.

5.5 Conclusions

BABT reduction potential by honeycomb inclusion in HCA-P2 was successfully demonstrated through foam projectile impact FEA. A combined VUMAT user subroutine and CZM material modeling approach was successfully implemented in the soft impact FEA to simulate three-dimensional stress state analysis with delamination in the HB50 composite. Normalized plastic deformation energy plot derived from the simulations indicated higher energy absorption by honeycomb than HB50 in bulging stage corroborating observations from experiments. Honeycomb inclusion did not alter energy absorption mechanisms in HB50 as also seen experimentally. Aluminum honeycomb

was found to reduce the amplitude of the stress wave pulse in the back laminate as well as delay the time of its arrival creating stress wave impedance and gradual dissipation of shock loads. A corresponding decrease in peak sternal loads can then be assumed correlating to a decrease in BABT. Time-history plot of displacement, velocity and acceleration derived from the simulation also proved a reduction in amplitude and time delay that can also be correlated to reduction in the propensity of viscous injury occurring in the underlying viscera of the chest cavity.

Foam impact FEA projects a significant performance improvement in HCA-P2 if load distribution on the honeycomb is kept uniform and over a larger area. Including a honeycomb with higher energy absorption capacity can further extend that advantage. Design methodology of HCA-P2 can be potentially modified to incorporate these factors. If deficiencies of VUMAT subroutine are solved, an actual 7.62 NATO ball projectile impact FEA can be carried out for direct comparison of injury tolerance criteria hard limits using the method presented here. This will be a part of the future work.

CHAPTER 6. SELECTION CRITERIA FOR HONEYCOMB INCLUSION IN LEVEL III HCA

6.1 Introduction

Ballistic tests on HCA revealed that honeycomb responds as a rigid plastic passive absorber under impact. Its inclusion improved armor performance by reducing BFS incurred on impact. BFS reduction was shown to be proportional to the energy absorption capacity of the honeycomb with the aid of analytically derived model based on energy conservation approach. Honeycomb inclusion also improved V_{50} in comparison to similar weight baseline when the front laminate areal density was above the critical. Honeycomb thus increased the energy absorption capacity per unit weight in the bulging stage than HB50 by increasing the flexural rigidity. It may be inferred that advantages by honeycomb inclusion can potentially be extended further by selecting other honeycombs with higher stiffness and crush strength than Al-CH. However, as seen from ballistic Test 4 results in Chapter 3, significant increase in armor stiffness reduces BFS, but it also adversely affects V_{50} by increased shear failure in HB50. Mechanisms of improving V_{50} and reducing BFS in HB50 are hence functionally opposite. It is possible achieve both objectives only if these mechanisms can be isolated.

A solution to this problem can be in isolation of the front laminate from the honeycomb sandwich. Inclusion of the spacer will allow HB50 plies to have a membrane like response critical to their penetration resistance, while the increased stiffness sandwich can then facilitate in BFS reduction. The spacer material can be low-relative-density polymeric foam for minimum weight addition, with lower bending stiffness than HB50 for minimum resistance to membrane like motion of the plies. Consequently, a larger area of honeycomb will be directly involved in the energy absorption process, and as numerically proven in Chapter 5, will also improve stress wave impedance with gradual shock load dissipation. Detailed experimental evaluation is necessary to confirm effectiveness of the spacer and can be a part of the future work. It is assumed here that the proposed solution is adequate to maintain a constant energy absorption capacity of the HB50 laminates in HCA while retaining their functionality irrespective of the included honeycomb. A methodology of honeycomb selection is then proposed here that can allow to choose suitable candidates from commercially available honeycombs in order to achieve a higher BABT reduction than by Al-CH. Objective of this study is to present selection criteria that are based on the functional contributions of the honeycomb in HCA identified through experiments and numerical simulations. Each criterion considers certain human BABT tolerance parameters stated in section 2.1.4.3 of Chapter 2. This is done keeping in mind that current parameter thresholds could be premature and their values can be updated in future with more focused studies. The scheme for each criterion is purposely devised for easy adaptation in case of such an eventuality. The process utilized can serve as a guideline for similar applications.

6.2 Honeycombs applicable in composite armor

Technical data sheets for commercially available honeycombs manufactured by Hexcel Co. and Plascore Inc. were referred to identify the highest specific strength honeycombs available. As a first step, only those honeycombs with crush strength of 7.4 MPa or higher were selected considering the Nomex™ honeycomb used in Chapter 3 as a baseline. These honeycombs are listed in Table 21 with their mechanical properties.

Table 21 Commercial honeycombs with crush strength of 7.4 MPa or higher. Designation and mechanical property details are listed. Permissible thickness values on applying design constraints are also stated.

Base Material	Honeycomb designation	Density (kg/m^3)	Elastic Modulus, E_c (GPa)	Crush strength (MPa)	c_t † (mm)	c * (mm)
Al 5052	Rigicell™ 1/8 - 2 - .006-STD	354.00	6.69	28.3	6.5	6.5
Al 5052	Rigicell™ 1/8 - 2 - .0038-STD	232.26	4.48	14.8	9.9	9.9
Al 5052	Rigicell™ 1/8 - 2 - .003-STD	192.22	3.86	10.0	12.0	10.0
Al 5052	CR-PAA 1/8 - 5052 - .003	192.22	6.21	9.3	12.0	10.0
Al 5052	CR-PAA 1/16 - 5052 - .0015	198.62	4.48	8.3	11.6	10.0
Fiberglass-PR	HRP - 3/16 - 12.0	192.22	1.79	7.9	12.0	10.0
Al 5052	CR-PAA 1/8 - 5052 - .0025	160.18	3.45	7.2	14.4	10.0
Nomex	PN2 - 1/8 - 9.0	144.16	0.62	7.4	16.0	10.0

† Maximum permissible thickness in compliance to the maximum allowable areal density constraint. * Adjusted maximum permissible thickness based on constraints related to insert ergonomics.

Any honeycomb that is to be included in a revised HCA design must continue to follow the primary design constraint of maximum permissible weight. A functional areal density limit of 18.5 kg/m^2 set in the insert preliminary design phase was used to stay relevant with contemporary body armor solutions. Maximum permissible areal density for honeycomb inclusion was then 2.3 kg/m^2, after accounting for the front and back laminates. Maximum permissible thickness for each honeycomb corresponding to this areal density was calculated. Honeycomb panels of specific thickness are typically cut

out of a larger hobe. Minimum thickness of these panels cannot be less than 6 mm owing to manufacturing difficulties. Similarly, ergonomics associated with the body armor insert restrict its total thickness to less than 38 mm (1.5 inches). These constraints limit permissible honeycomb thickness to within 6 – 10 mm. Maximum permissible thickness for each honeycomb was adjusted after complying with all design constraints and is also listed in Table 21.

6.3 Selection criteria for honeycombs

6.3.1 Specific strength criterion for minimum BFS

BFS at NIJ 0101.06 standard reference velocity of 847 m/s can be predicted using the experimentally verified analytical model detailed in Appendix 1. Energy absorbed at this velocity by the HB50 laminates and a chosen honeycomb can be calculated with the model in a similar way as done for Al-CH. Remainder of the energy transferred to the clay then correlates to a BFS prediction. Using this method, BFS at 847 m/s was calculated for each honeycomb listed in Table 21 with the adjusted thickness value. As a conservative estimate, surface area of honeycomb participating in the energy absorption process was kept identical to that observed in Test 4 of Chapter 3. Predicted BFS values are in Table 22. BFS diameter size of 8.56 cm was used for the calculation. Plot of energy absorption capacity of the honeycomb versus its crush strength shows only Al-CH and similar corrugated honeycombs of Rigicell™ type are able to meet the minimum BFS criterion by NIJ (Figure 32). For more stringent BFS limits, 28 mm as concluded by Gryth *et al.* [69] for example, set design constraints will have to be relaxed to achieve the desired performance even with the best Rigicell™ honeycomb inclusion.

Table 22 Predicted BFS values for selected honeycombs by using experimentally verified analytical model detailed in Appendix 1.

Designation	Maximum energy absorbed per unit volume (MJ/m^3)	Adjusted thickness (mm)	Energy absorption capacity, E_{hc} (J)	Predicted BFS at 847 m/s
Rigicell™ 1/8 - 2 - .006-STD	19.8	6.5	454.8	33.7
Rigicell™ 1/8 - 2 - .0038-STD	10.4	9.9	363.2	37.8
Rigicell™ 1/8 - 2 - .003-STD	7.0	10	247.5	43.0
CR-PAA 1/8 - 5052 - .003	6.5	10	230.4	43.8
CR-PAA 1/16 - 5052 - .0015	5.8	10	204.8	44.9
HRP - 3/16 - 12.0	5.6	10	196.3	45.3
CR-PAA 1/8 - 5052 - .0025	5.1	10	179.2	46.1
PN2 - 1/8 - 9.0	5.2	10	183.0	45.9

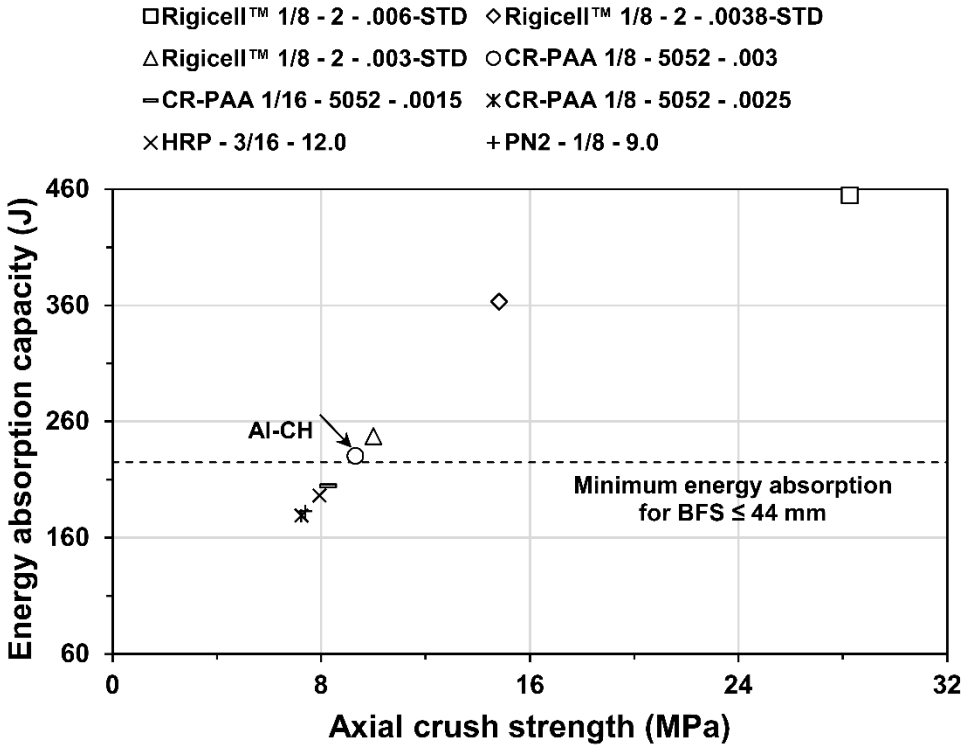

Figure 32 Energy absorption capacity versus axial strength plot for the selected honeycombs shows only corrugated honeycombs like Al-CH are able to meet the minimum BFS requirement by NIJ at the reference velocity of 847 m/s.

ΔBFS / ΔAD was calculated for the honeycombs with BFS less than 44 mm keeping a baseline of 14 + 2 HB50 laminate configuration as a reference (Table 23). BFS for this baseline was 54.1 mm, as experimentally found in preliminary ballistic test of Chapter 3. ΔBFS / ΔAD values were seen to be predictably proportional to the included honeycomb specific strength (refer equation 3.1). It can therefore be implied that specific strength of a honeycomb is an acceptable criterion for its selection in armor applications. Highest specific strength is most desirable.

Table 23 Comparison of candidate honeycombs using ΔBFS / ΔAD values calculated using using experimentally verified analytical model detailed in Appendix 1.

Property	CR-PAA 1/8 - 5052 - .003	Rigicell™, 1/8 - 2 - .003-STD	Rigicell™, 1/8 - 2 - .0038-STD	Rigicell™, 1/8 - 2 - .006-STD
Added areal density, ΔAD (kg/m^2)	1.922	1.922	2.300	2.301
Analytically predicted BFS (mm)	43.8	43	37.8	33.7
Specific strength (MPa / kg/m^3)	0.048	0.052	0.064	0.080
ΔBFS / ΔAD calculated with baseline (14+2 HB50 configuration) BFS of 54.1 mm as reference	5.36	5.78	7.09	8.87

6.3.2 Bending deflection criterion for maximum rigidity

Termination of shear damage coupled with delamination at the end of bulging stage of projectile penetration in HB50 results in near-intact rear plies' traverse along the projectile direction creating the back face bulge. Considering the sandwich construction of the HCA, bulging of the rear plies of the front laminate causes corresponding deflections in the following honeycomb and back liner layers. The cumulative deflection profile of the front laminate rear layers with the honeycomb and back liner (section ABCD in Figure 33a) resembles that of a simply supported sandwich beam undergoing

bending under a central load. Deflection magnitude and velocity is inversely proportional to the beam's resistance to bending. Hence, it is possible to analytically correlate the extent of deflection or back face bulge for each type of honeycomb by applying bending theory to HCA.

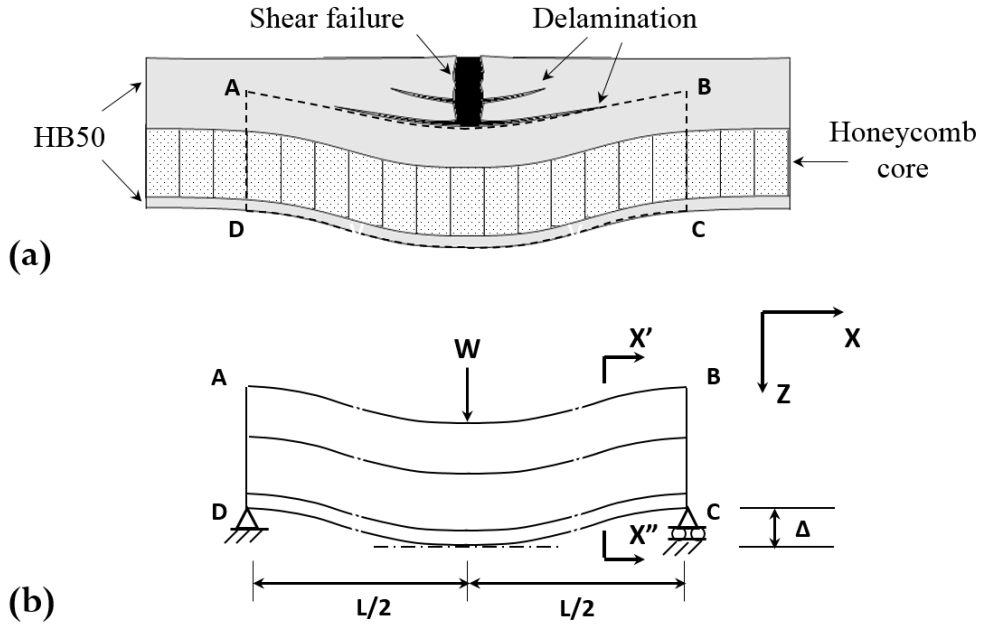

Figure 33 (a) Vertical cross section of HCA after deformable projectile impact indicating shear and delamination zones in the front HB50 laminate resulting in back face bulging. Corresponding deflections are also transferred to the successive honeycomb and back liner layers (b) deflection profile of HCA (shown by section ABCD) resembles that of a simply supported sandwich beam undergoing bending under a central load.

The deflections in sandwich beams undergoing bending can be derived from the analysis presented by Allen [94]. This analysis assumes that the cross-sections which are plane and perpendicular to the longitudinal axis of the unloaded beam will remain so when the bending is taking place. The simplest form of this analysis considers the sandwich beam undergoing bending has thin faces of equal thickness and an antiplane core (shear stresses in the core are constant and independent of z location). However, in case of HCA we have thick face layers of unequal thickness and the honeycomb core is

not antiplane. Allen's analysis is modified to accommodate these changes and an expression for deflection in the z direction is evaluated for the HCA.

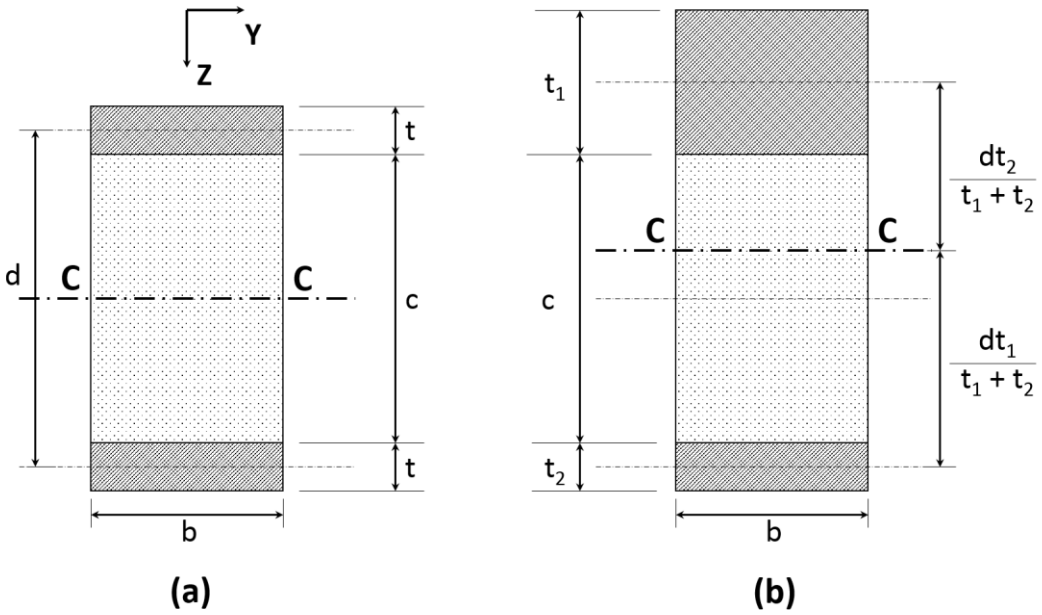

Figure 34 Section X'X" for the bending beam (a) if the beam was a regular sandwich (b) if it resembles HCA.

Deflections in a bending beam result from a combined effect of bending moments and shear stresses. Maximum deflection will occur at the beam's central plane and is calculated by summation of bending and shear components. The bending component is calculated by using the flexural rigidity *D* of the beam which is a product of the modulus of elasticity *E* and the second moment of area *I*. The sandwich beam being composite in nature, *D* is a sum of the products *EI* for the individual faces and the honeycomb core. The shear component of deflection is calculated using the shear rigidity *AG*. Since the faces for HCA sandwich are of unequal thickness, the centroidal axis of the bending beam (axis shown by C-C in Figure 34) no longer coincides with the horizontal mid plane of the core. The z location of the centroidal axis of HCA z_c is given by:

$$z_c = \frac{t_1}{2} + \frac{dt_2}{t_1 + t_2} \tag{6.1}$$

where, d is the distance between centroids of the faces, t_1 and t_2 are the thicknesses of the face sheets. The second moment of area for each face and the core is evaluated about the centroidal axis using the parallel axis theorem. For a regular sandwich beam undergoing bending with thin faces of equal thickness, Allen neglects the contribution of I for the faces and the core about their own axis in the equivalent moment of area as they account to 1% or less in magnitude compared to the moment-transfer-to-centroidal-axis term. In the present analysis, all terms are retained as the equations to verify negligible contribution are not satisfied (see Table 24). The sum of the second moment of area for the faces bending separately is given by:

$$I_F = \frac{bd^2 t_1 t_2}{2} + \frac{b}{12}[{t_1}^3 + {t_2}^3] \tag{6.2}$$

Table 24 Verification of conditions stated by Allen [94] to select second moment of area terms to be retained in flexural rigidity analysis.

For a regular sandwich beam: Flexural rigidity, $D = E_F \frac{bt^3}{6} + E_F \frac{btd^2}{2} + E_C \frac{bc^3}{12}$

where, E_F = Axial modulus of elasticity for the faces
E_C = Modulus of elasticity for the core in the z direction
b = beam width, c = core thickness, d = distance of separation between centroids of the faces, and t = thickness of the face sheets, as shown in Figure 34a.

First term in the above D equation amounts to less than 1% of the second if: $d/t > 5.77$	For HCA, t_1 = 14mm, t_2 = 2mm, and $6 \leq c \leq 10$mm, giving $d \leq 22$mm. As $t_1 \neq t_2$, using t_{avg} = 8mm, we get, $d/t_{avg} < 5.77$ Condition is not satisfied and the term is retained in the analysis.
Third term in the above D equation amounts to less	For HCA, E_F = 10 GPa, E_C = 6-11 GPa, $t_{avg}/c < 1$,

than 1% of the second if:	and $d/c < 2$,
$6\frac{E_F}{E_C}\frac{t}{c}\left(\frac{d}{c}\right)^2 > 100$	$6\frac{E_F}{E_C}\frac{t}{c}\left(\frac{d}{c}\right)^2 < 100$
	Condition is not satisfied and the term is retained in the analysis.

The second moment of area for the honeycomb core is given by:

$$I_c = \frac{bc^3}{12} + bc\left[\frac{t_1 + c}{2} - \frac{dt_2}{t_1 + t_2}\right]^2 \tag{6.3}$$

Equivalent flexural rigidity $(D)_{eq}$ for HCA is given by the summation:

$$(D)_{eq} = E_F\left[\frac{bd^2 t_1 t_2}{2} + \frac{b}{12}[{t_1}^3 + {t_2}^3]\right] + E_C\left[\frac{bc^3}{12} + bc\left[\frac{t_1 + c}{2} - \frac{dt_2}{t_1 + t_2}\right]^2\right] \tag{6.4}$$

The local bending stiffness of the faces has an effect on the shear deformation of the core. If the faces and the core are to remain in contact during bending, there has to be a smooth transition of shear deflections across the beam. Faces reduce shear deflection discontinuity at the expense of introducing additional bending moments and shear forces in the faces. This effect is prominent if the faces are thick with a weak core and has to be accounted for during estimation of the shear rigidity of the beam. In the present analysis, although the faces are thick, the core material is not weak and therefore no correction is necessary while calculating the shear rigidity. The deflection due to shear is obtained by the integral expression:

$$\Delta_s = \int \frac{Q}{AG}dx = \frac{Q}{AG}x + C \tag{6.5}$$

where, Q is the shear force, G is effective shear modulus of the core material and A equals bd^2/c. For a simply supported beam with central load W, the shear force Q is $W/2$. The integration constant C will also cancel out as at $x=0$, $\Delta_s=0$. The expression simplifies to:

$$\Delta_s = \frac{W}{2AG}x \tag{6.6}$$

Also, maximum deflection will occur at beam central plane ($x=L/2$) giving $(\Delta_s)_{max} = WL/4AG$. Now, as the honeycomb core is not antiplane in nature, the shear stress is not constant over the depth. To account for this change, Allen recommends replacing G with G' to give the correct deflection magnitude where,

$$G' = \frac{G}{1 + \frac{E_C}{6E_F}\frac{c^2}{t(c+t)}} \tag{6.7}$$

The total beam deflection by load W acting over beam span L is given by the sum:

$$(\Delta)_{eq} = (\Delta_b)_{max} + (\Delta_s)_{max} = \frac{WL^3}{48(D)_{eq}} + \frac{WL}{4AG'} \tag{6.8}$$

Calculation for equivalent deflection as per the theory presented above is shown in Table 25. It was observed that the best choice honeycomb according to the specific strength or energy absorption criterion displayed maximum deflection per kN load. The propensity of viscous injury scales directly with back face bulge velocity and acceleration which are time derivatives of this maximum deflection. It is desirable to have highest specific stiffness and thickness of the included honeycomb to maximize flexural rigidity for

reducing deflection by bending. High bond strength between HB50 plies and at the face sheet–core interface is desired to maximize shear rigidity.

Table 25 Comparison of candidate honeycombs by bending deflection analysis.

Property	CR-PAA 1/8 - 5052 - .003	Rigicell™, 1/8 - 2 - .003-STD	Rigicell™, 1/8 - 2 - .0038-STD	Rigicell™, 1/8 - 2 - .006-STD
Foil thickness, t (mm)	0.0762	0.0762	0.09652	0.1524
Cell edge, l (mm)	1.833	1.833	1.833	1.833
Density, ρ (kg/m^3)	192.2	192.2	232.3	354
Elastic modulus, E_C (GPa)	6.2	3.9	4.5	6.7
Crush strength (MPa)	9.3	10	15	28
Specific strength (MPa/ kg/m^3)	0.048	0.052	0.065	0.079
Shear modulus, G_{13} (GPa)	0.6	0.6	0.8	1.2
Shear modulus, G_{23} (upper)	1.0	1.0	1.3	2.1
Shear modulus, G_{23} (lower)	0.9	0.9	1.2	1.9
Average shear modulus, G (GPa)	0.9	0.9	1.1	1.7
Maximum permissible height, c (mm)	10.0	10.0	9.9	6.5
Face material modulus, E_F (GPa)	10.0	10.0	10.0	10.0
Effective core shear modulus, G' (GPa)	0.8	0.8	1.0	1.7
Beam width, b (length CD in Figure 33, m)	0.131	0.131	0.131	0.131
Beam span, L (m)	0.131	0.131	0.131	0.131
Face centroid separation distance, d (m)	0.0180	0.0180	0.0179	0.0145
Equivalent flexural rigidity, Deq (N.m^2)	1146.1	834.6	904.6	730.2
Equivalent shear rigidity, AG' (kN)	3446.13	3522.89	4434.15	7060.94
Deflection per kN load, Δeq (mm)	0.050	0.065	0.059	0.069

6.3.3 Stress wave impedance criteria for minimum stress transfer

Numerical analyses conducted as a part of this study have shown stress wave transfer in materials undergoing impact is a three-dimensional event. However, it is possible to utilize a one dimensional stress wave analysis as a crude tool to characterize stress wave impedance potential in materials. Analytical scheme for one dimensional analysis has been presented by Hazell [13] to estimate stress transfer on impact in multilayered armor

through geometric wave impedance calculations at material interfaces. Consider an X-t diagram for a bi-material interface as shown in Figure 35a.

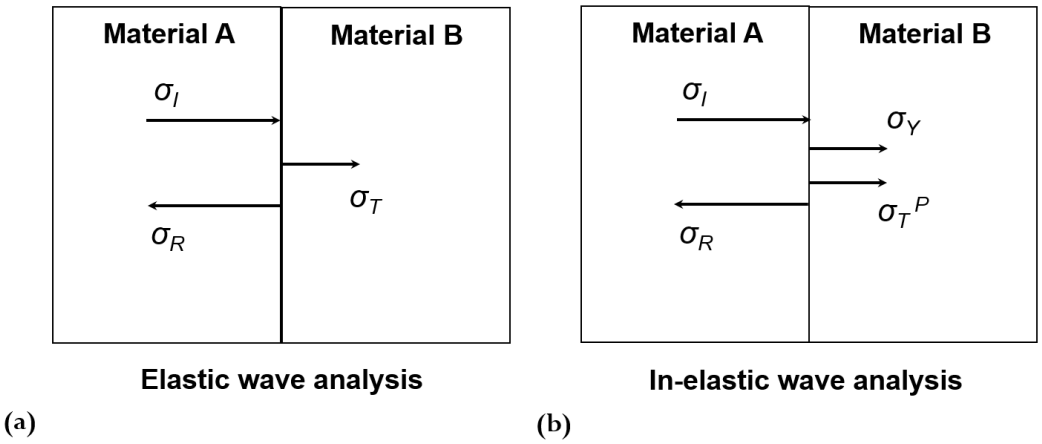

Figure 35 X-t diagram schematic for one-dimensional (a) elastic and (b) in-elastic wave analysis at a bi-material interface.

As per elastic wave analysis, when the incident stress wave (denoted by σ_I) in material A reaches the interface, a part of it is transmitted to material B (denoted by σ_T) while the remainder is reflected back (denoted by σ_R). The amplitude of the elastic wave transmitted to material B is given by:

$$\sigma_T = 2\sigma_I \left(\frac{\sqrt{E_B \rho_B}}{\sqrt{E_A \rho_A} - \sqrt{E_B \rho_B}} \right) \tag{6.9}$$

where, E is the material elastic modulus and ρ is the material density. The term $(E\,\rho)^{1/2}$ represents the elastic impedance at the material interface with suffixes denoting the corresponding material. If material B is considered to be elastic-plastic then in-elastic wave analysis applies whereby the transmitted wave is represented by a summation of elastic wave corresponding to the yield stress (denoted by σ_Y) and the plastic wave

corresponding to the peak stress (denoted by ${\sigma_T}^P$). This is represented by the X-t diagram in Figure 35b. The amplitudes of the transmitted elastic and plastic waves are given by:

$$ {\sigma_T}^P = \frac{\sigma_I}{A}\left(\frac{B-A}{B-C}\right) - \frac{\sigma_R}{A}\left(\frac{B+A}{B-C}\right) \tag{6.10a} $$

$$ \sigma_Y = \frac{\sigma_I}{A}\left(\frac{C-A}{C-B}\right) - \frac{\sigma_R}{A}\left(\frac{C+A}{C-B}\right) \tag{6.10b} $$

$$ \text{where, } A = \sqrt{E_A\rho_A} \quad B = \sqrt{E_B\rho_B} \quad C = \sqrt{S_B\rho_B} $$

and, S_B denotes the reduced modulus in material B after the onset of plasticity. For HCA-P2, the HB50 laminates can be assumed to be pure elastic in accordance to tensile behavior and higher strains to failure. For the honeycomb, the stress at yield is represented by the bare compressive strength of the honeycomb, whereas, the peak plastic stress is represented by the crush strength of the honeycomb that stays constant up to densification. Since the bare compressive strength has a higher magnitude than the crush strength, $\sigma_Y > {\sigma_T}^P$ and peak stress transfer will occur during the elastic regime. It is therefore sufficient to apply elastic wave transfer theory to the HCA honeycomb sandwich in order to evaluate stress wave impedance by each selected honeycomb from the earlier section. The interface between front face sheet and honeycomb core is identical to the interface between the core and the back face sheet for a sandwich composite with same face sheet material. Stress transmitted through this two-interface system is given by:

$$ \sigma_T = 4\sigma_I \frac{\sqrt{E_F\rho_F}\sqrt{E_C\rho_C}}{(E_F\rho_F + E_C\rho_C)^2} \tag{6.11} $$

where, suffix *F* denotes HB50 material while suffix *C* denotes the selected honeycomb core. Transmitted stress to the back laminate was estimated for each honeycomb using equation 6.11 and the calculations are presented in Table 26. Stress wave dispersion by bonding adhesive was neglected in the analysis. Elastic modulus for HB50 in the through-thickness direction (E_F) is 10 GPa and density (ρ_F) is 980 kg/m^3.

Table 26 Comparison of candidate honeycombs by elastic stress wave impedance analysis.

Property	CR-PAA 1/8 - 5052 - .003	Rigicell™, 1/8 - 2 - .003-STD	Rigicell™, 1/8 - 2 - .0038-STD	Rigicell™, 1/8 - 2 - .006-STD
Core density ρ_C (kg/m^3)	192.2	192.2	232.3	354
Core elastic modulus, E_C (GPa)	6.2	3.9	4.5	6.7
σ_T / σ_I x 10^{-4}	1.13	0.97	1.09	1.30

Honeycomb with maximum difference in elastic modulus compared to HB50 has the highest stress wave impedance. According to this criterion, honeycomb with the least elastic modulus is desirable.

6.4 Summary from selection methods

Three selection criteria that are based on the functional contributions of the honeycomb in HCA were successfully developed. It was now possible to use these criteria simultaneously to select a candidate honeycomb with optimum performance that can potentially achieve a higher BABT reduction than by Al-CH. This is demonstrated in Table 27 by applying a ranking system for each criterion. Rigicell™ 1/8-2-.0038-STD honeycomb demonstrated optimum performance. No single honeycomb had the best performance according to more than one criterion. As a part of future work, new HCA-P2 variant including the optimum performing Rigicell™ honeycomb can be ballistic tested and compared with Al-CH. Rigicell™ 1/8-2-.003-STD honeycomb with next near-

optimum performance can also be included in the test scheme to observe performance transitions, if any.

Table 27 Selection of candidate honeycomb with optimum performance to achieve higher BABT reduction than Al-CH by simultaneous consideration of developed criteria by applying a ranking system. Optimal choice is highlighted.

Criterion	Performance ranking of candidate honeycombs			
	Worst	→		Best
Highest specific strength	A	B	C	D
Minimum bending deflection	D	B	C	A
Highest stress wave impedance	D	A	C	B
A - CR-PAA 1/8 - 5052 - .003		**B** - Rigicell™ 1/8 - 2 - .003-STD		
C - Rigicell™ 1/8 - 2 - .0038-STD		**D** - Rigicell™ 1/8 - 2 - .006-STD		

Steps followed during the selection procedure are summarized and represented in the form of a flow chart schematic in Figure 36. The method used for selection can be easily adapted to suit other armor application. For example, the primary threshold metric for initial choice refinement was BFS in this study, which can be switched to V_{50} by altering the analytical model. The selection criteria used in the ranking system can be similarly changed based on the end design functionality of the honeycomb sandwich.

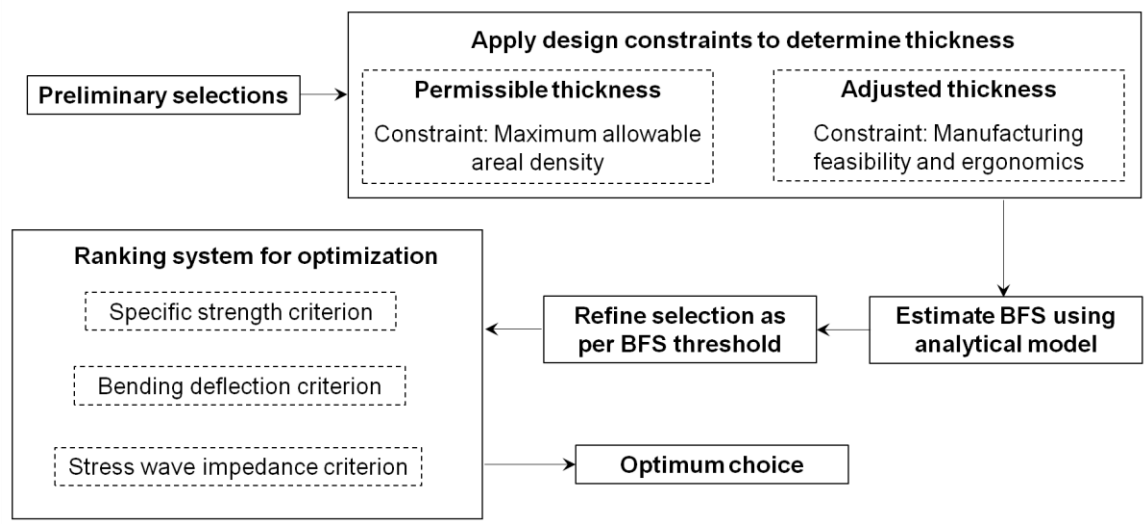

Figure 36 Flowchart schematic for the selection process used to determine honeycomb with optimum performance to achieve higher BABT reduction than Al-CH. The selection method presented here can be easily adapted to suit other armor applications.

Peak sternal force threshold as per AIS-code 3 (no permanent injury) is 21 kN (Table 9). It correlates to a maximum permissible stress of 3.5 MPa, if considered to act over experimentally observed BFS area of ~60 cm^2. No candidate honeycomb from the preliminary selection can meet this requirement while achieving the desired BFS reduction. Therefore, a polymeric foam liner as a trauma attenuating backing (TAB) between the insert and user body cannot be avoided. TAB foam thickness again governs how much energy it can absorb. As permissible values are again limited by ergonomics to within 6-10 mm, maximum absorbable energy by the foam up to densification is 5-10 J. Ideal foam candidate for the TAB can then be selected using the iterative procedure with energy absorption diagram (EAD) presented by Gibson and Ashby [11]. Peak stress and energy limits derived here will be the applicable constraints. A combination of improved ballistic performance HCA and the foam TAB can ensure minimum BABT injury to the wearer.

CHAPTER 7. CONCLUSIONS AND FUTURE WORK

A fabrication process and design method for integration of honeycomb cellular solids in body armor was successfully established in this study. Ballistic tests showcased the benefits of honeycomb inclusion in HCA by demonstrating a maximum BABT reduction of 40.8% compared to a same weight HB50 baseline. BFS reduction capabilities of the HCA improved proportionately with increase in the included honeycomb thickness. This confirmed the first part of the research hypothesis that *inclusion of a minimum thickness honeycomb in multilayered body armor improves ballistic performance compared to the same areal density armor without honeycomb*. The later part of this hypothesis implied that *this minimum honeycomb thickness depends on the face material and material properties of the honeycomb* was successfully confirmed by good agreement shown between experimental data and the analytical model developed as a part of this study. V_{50} analysis and BFS tests were able to show that a critical areal density of the front laminate is necessary for honeycomb to be useful.

Gauging the effect of honeycomb properties on its area extent undergoing impact is the next logical research gap to be filled. A meta-aramid base material (Nomex™) honeycomb has been identified with properties intermediary to AMH and Al-CH.

Ballistic test on inserts with varying Nomex honeycomb and Al-CH thickness could be repeated after addressing the penciling effect seen due to the applied fabrication process. Ballistic testing of these plates can be conducted along with accelerometer or piezo-pressure sensors (mounted on clay backing or an instrumented dummy) for a possible stress wave impedance analysis. Tests would primarily focus on obtaining data on BFS depth and size at each shot velocity. Observed results would provide additional time dependent metrics for direct comparison between the baseline, Al-CH-based HCA, and Nomex-based HCA. Ballistic gel as an alternate backing material can prove useful to obtain visual cues on ballistic performance through high-speed imaging.

Numerical analysis results obtained in this study were able to supplement experimental observations by proving performance benefits of honeycomb inclusion in HCA. The method developed here for modeling HB50 cross-ply composite and honeycomb can serve as a guideline for future FEA. Modifying the VUMAT subroutine code for convergence and stability under high velocity impact is envisioned as a necessary next step for future work. An actual 7.62 NATO ball projectile impact FEA can be carried out for direct comparison of injury tolerance criteria hard limits using the method presented here.

It was proved through this study that mechanisms of improving V_{50} and reducing BFS in HB50 are functionally opposite. It is possible to achieve both objectives only if these mechanisms can be isolated by inclusion of a low stiffness polymeric foam spacer between the front laminate and honeycomb sandwich. Inclusion of the spacer can permit membrane-like ply motion in HB50 which is critical to maintain its penetration resistance while simultaneously allowing the honeycomb sandwich to be as rigid as possible for

reducing BFS. Rigicell™ 1/8-2-.0038-STD honeycomb that demonstrated optimum performance through the selection scheme devised in this study can be the included honeycomb. This hypothesis could also be tested as a part of future work. This revised HCA insert design is envisioned to have the greatest BABT reduction capability.

APPENDICES

Appendix 1:

Semi-empirical and analytical model for the prediction of BFS

Fabric composite armors defeat deformable projectiles by absorbing their kinetic energy through a range of plastic deformation modes. The prominent modes include fiber - shear, elongation and pullout coupled with the resulting delamination. A part of this kinetic energy is spent on deforming the projectile by petal-like stripping of the jacket and pancaking of the soft core. The extent of projectile deformation depends upon the core and armor materials, impact obliquity, and the projectile velocity. The remainder of the kinetic energy and structural loads during impact are transferred to the backing material. Bulging of the armor back wall during the entire process creates a spherical dent in the backing material termed the BFS. The extent of this energy transferred to the backing material can be estimated by the size of the BFS. Other dissipation processes (like gross mechanical excitation and conversion to heat) consume less than 2% of the initial projectile kinetic energy and can be ignored. The energy absorption process can then be represented by the equation:

$$E_{K.E.} = E_{pd} + E_{back} \quad \text{(A1.1)}$$

where, $E_{K.E.}$ is the initial kinetic energy of the projectile, E_{pd} is the energy absorbed by the composite through plastic deformation modes, and E_{back} is the energy transferred to the clay backing material.

Semi-empirical model for BFS prediction:

Jacobs and van Dingenen presented an empirical model for V_{50} prediction of Dyneema® based armors against deformable soft core projectiles like the 7.62 NATO Ball [22]. It was an extension of the model developed for similar estimation against Fragment Simulating Projectiles (FSPs). The FSP model approximated the relation between the strike face area *S* which is the projectile cross-sectional area projected on the target, the energy absorbed E_{pd} and the areal density of the target *AD* by:

$$E_{pd}/S = AD \times k_1 \quad \text{(A1.2)}$$

with E_{pd} in Joules, *S* in mm^2, *AD* in kg/m^2 and k_1 is a ballistic material related constant. It assumed the strike face area to be constant throughout the penetration process and the contribution of each layer in energy absorption was the same. FSPs penetration in relatively thick Dyneema® based armors is a two stage process as shown in Figure 37a. Jacobs and van Dingenen adapted Equation A1.2 for deformable projectiles by considering penetration as a three stage process. Stage 1 considers projectile penetration while retaining pre-impact strike face area, similar to an FSP. In stage 2, the projectile undergoes deformation consuming some energy and then continues penetration with

increased strike face area again like a FSP in the stage 3. The energy absorbed by the composite under deformable projectile impact can then be represented by the relation:

$$E_{pd} = E_{pd1} + E_{bd} + E_{pd2} = AD_1 \times S_1 \times k_1 + E_{bd} + AD_2 \times S_2 \times k_1 \qquad \text{(A1.3)}$$

with E_{pd1} as the absorbed energy during initial shearing corresponding to composite areal density AD_1 and initial strike face area S_1, E_{bd} as the energy absorbed in bullet deformation, which is experimentally observed to be relatively constant (160-300J) for a given deformable projectile type; and E_{pd2} as the absorbed energy corresponding to the deformed strike face S_2 and involved the composite areal density AD_2. Equation A1.3 was successfully used to predict V_{50} for Dyneema® HB2 under 7.62 NATO Ball impact [22].

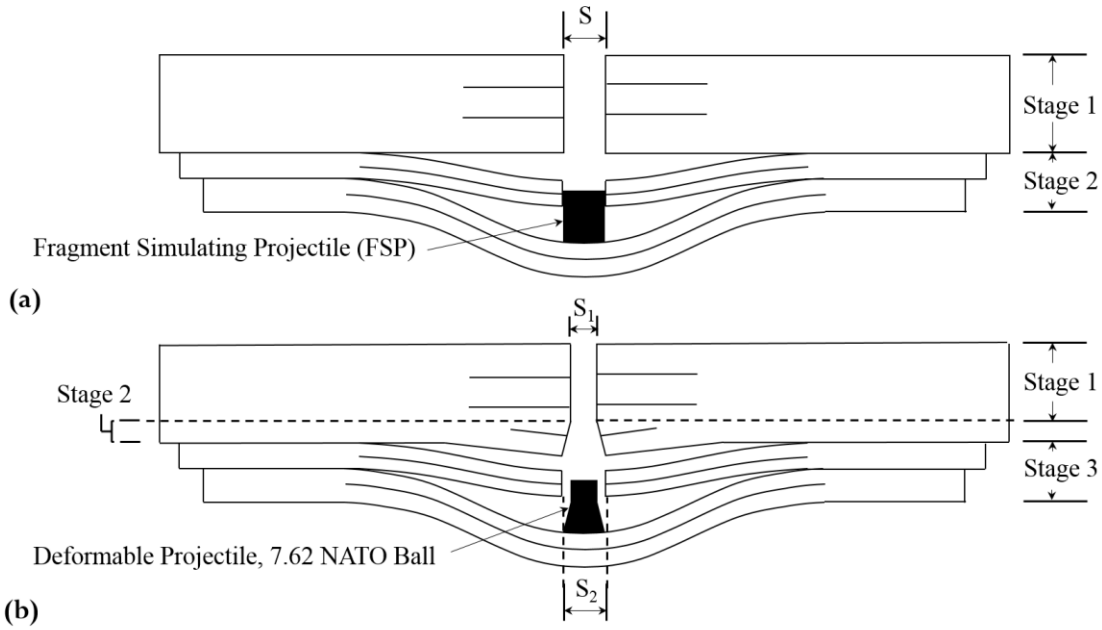

Figure 37 (a) Cross-section schematic of Dyneema® based armor tested with a Fragment Simulating Projectile (FSP) showing two distinct stages of penetration however with constant a constant strike face area, (b) cross-section schematic of Dyneema® based armor tested with a deformable soft core projectile like the 7.62 NATO Ball showing a three stage penetration process where the projectile strike face area increases due to deformation.

The bullet deformation is near instantaneous and the transition from stage 1 to stage 3 can be considered immediate. If R is the ratio of stage 1 areal density AD_1 with the total areal density AD (with $AD_1 + AD_2 = AD$), the model can be expressed as:

$$E_{pd} = (RS_1 + (1 - R)S_2)AD \times k + E_{bd}. \quad \text{(A1.4)}$$

The ratio R is linearly proportional to the projectile velocity V, as increase in V will result in more number of plies failing with shear dominated failure. Consider $R = xV + y$, and, $S_2 - S_1 = S$ (with $S_2 > S_1$), E_{pd} can be expressed as:

$$E_{pd} = f(V) \times AD + E_{bd} \quad \text{(A1.5a)}$$

where, $f(V)$ is also a linear function of variable V given by:

$$f(V) = (S_2 - S\,x\,V - S\,y)k = -a\,V + b \quad \text{(A1.5b)}$$

Experimental data from FSP impact tests on HB26 was presented in [77]. It was used to plot the energy absorbed per unit strike face area versus panel areal density curve which is non-linear (Figure 38a). Regions of single stage tensile failure by bulging (characteristic for thin plates) and two stage shear with tensile bulging failure modes as observed from the tests have been delineated in the plot. Narrowing the focus to practical body armor insert areal densities ($\leq$ 24 kg/m^2) and single stage perforation zone where the stated assumptions of empirical FSP model apply, the linear fit approximation for energy absorbed per stage with areal density in Equation A1.2 becomes fair (Figure 38b).

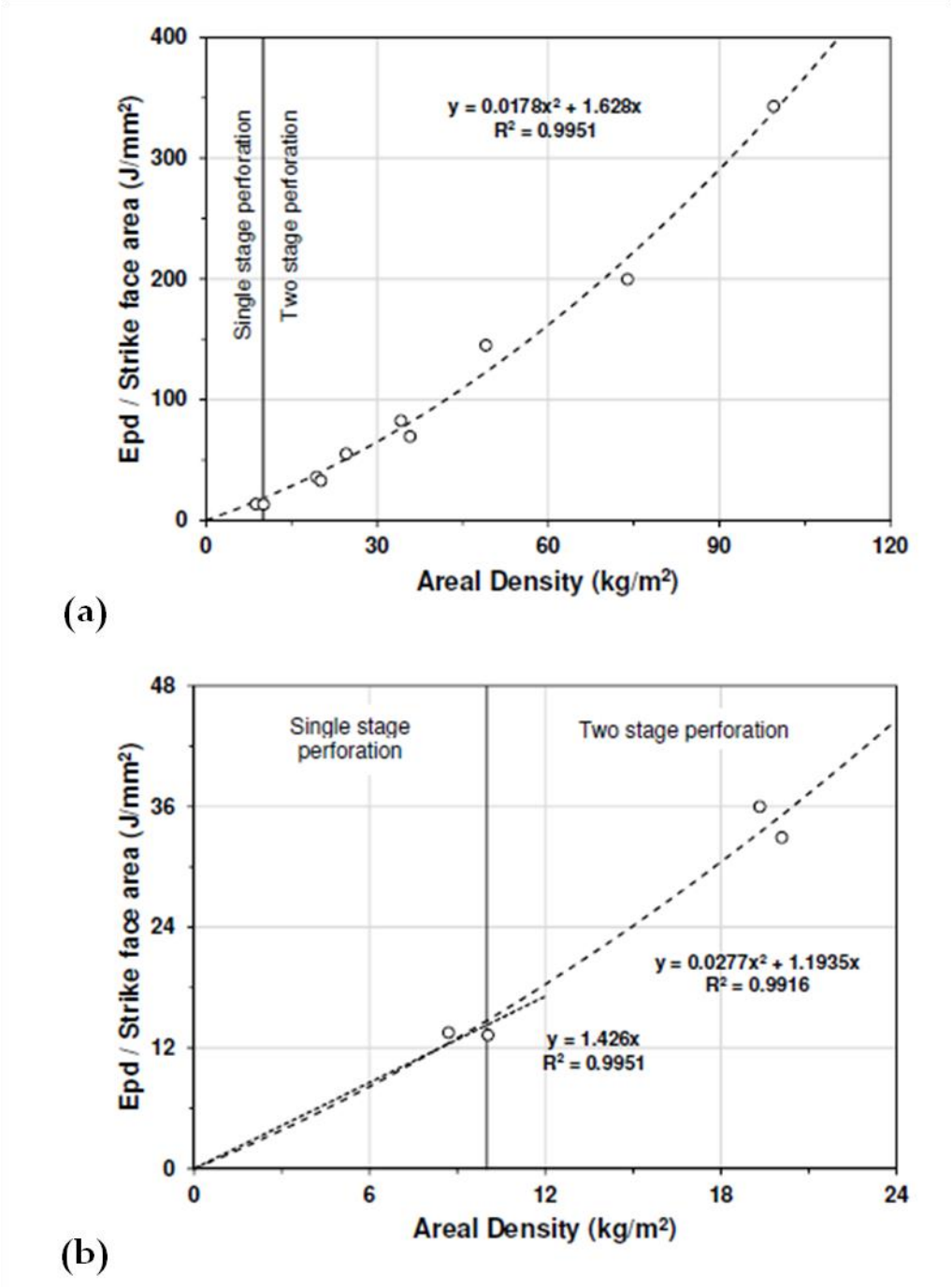

Figure 38 (a) Energy absorbed per unit strike face area versus target areal density plot for HB26 made using experimental data from FSP impact tests presented in [77]. Curve shows a non-linear trend, (b) zoomed-in section of the same plot with focus on practical body armor areal densities (≤ 24 kg/m^2) showing a linear fit to the energy absorbed per stage data as a fair assumption.

Similar expression is required for estimating E_{back}. Results from a recent study on damage characterization of 7 different types of projectiles indicates that recorded BFS from Roma Plastilina clay backing scales better with kinetic energy density of the impacting projectile than the kinetic energy itself [95]. This is highlighted in Figure 39 where kinetic energy density versus BFS has a much higher R^2 value. This implies size and depth of the BFS indent are both important factors to correlate it to the energy transferred to the clay. E_{back} can be estimated for a known BFS and impact zone size using:

$$E_{back} = \left(\frac{\pi}{4} D^2\right) \times g(BFS). \tag{A1.6}$$

where, E_{back} is the energy transferred to the clay backing in Joules, D is the diameter of the impact zone in cm, and $g(BFS)$ is the empirical relation relating the kinetic energy density with the BFS (in mm) as shown by the linear regression fit in Figure 39. Substituting equations A1.5 and A1.6 in equation A1.1 and rearranging terms, we get:

$$g(BFS) = \frac{4}{\pi D^2}[E_{K.E.} - (-aV + b)AD - E_{bd}]. \tag{A1.7}$$

Substituting terms for the kinetic energy of bullet with mass m and empirical expression of $g(BFS)$, we get:

$$BFS = \frac{3.346}{D^2}\left[\frac{mV^2}{2} + a\,AD\,V - (E_{bd} + b\,AD)\right]. \tag{A1.8}$$

With further rearrangement of terms for simplification:

$$BFS = AV^2 + BV - C \tag{A1.8a}$$

with,

$$A = \frac{1.6731m}{D^2}\ , \qquad B = \frac{3.346\ a\ AD}{D^2}\ , \qquad C = \frac{3.346}{D^2}[E_{bd} + b\ AD] \tag{A1.8b}$$

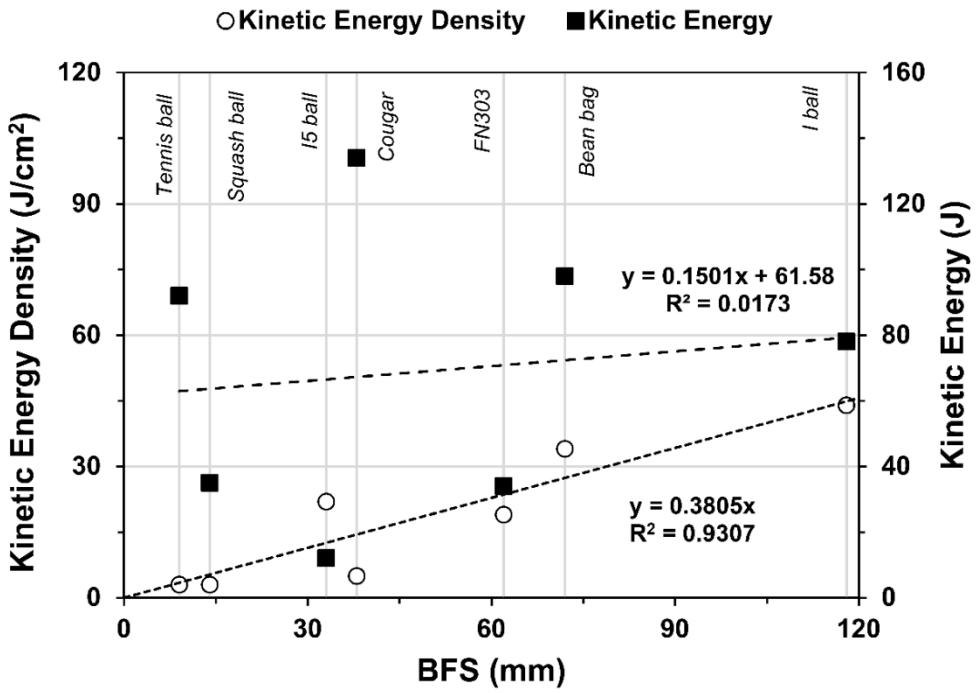

Figure 39 Relationship between a projectile's kinetic energy and kinetic energy density with the recorded BFS on Roma Plastilina clay backing post impact [95].

The increase of BFS with velocity can be analytically estimated for any particular areal density laminate of HB50 by calculating the energy transferred to the clay backing using the second order polynomial expression (equation A1.8). This scheme developed for the baseline can also be adapted for HCA to include the participation of the honeycomb in the energy absorption process. The energy balance equation for HCA is:

$$E_{K.E.} = E_{pd} + E_{hc} + E_{back} \tag{A1.9}$$

where, the additional term E_{hc} corresponds to the energy absorbed by the honeycomb. For metal based honeycombs with plastic buckling as the primary failure mode, the magnitude of E_{hc} depends on the honeycomb's crush strength σ_{cr} (in MPa) and densification strain ε_D:

$$E_{hc} = \int_0^{\varepsilon_D} \sigma_{cr}\, d\varepsilon \times A \times c \tag{A1.10}$$

where, A is the face area of the honeycomb that undergoes compression during impact in m^2 and c is the honeycomb layer thickness in m. The product of A and c gives the honeycomb volume participating in the energy absorption process. The definite integral term denotes the energy absorption capacity during compression which is equal to the area under the stress versus strain curve for the honeycomb. The magnitude of E_{hc} will depend on the velocity only when the cellular solid has significant strain rate dependence. Crush strength of the honeycomb is directly proportional to the flow stress of the base material (σ_{eq}) whose variation with strain rate can be well represented by the Johnson – Cook flow stress model:

$$\sigma_{eq} = [A + B\varepsilon^n][1 + C\dot{\varepsilon}^*][1 - T^{*m}] \tag{A1.11}$$

where, A,B,C, n and m are material constants, T^{*m} is the homologous temperature, ε is the strain, and $\dot{\varepsilon}^* = \dot{\varepsilon}/\dot{\varepsilon}_0$ is a dimensionless strain-rate given by the ratio of the present strain rate $\dot{\varepsilon}$ and the reference strain-rate $\dot{\varepsilon}_0$. If adiabatic effects are ignored, only the first two terms of the expression are considered. The strain rate is related to the impact velocity by:

$$\varepsilon = \left(\frac{v_i - v_0}{2c}\right) \tag{A1.12}$$

where, v_i is the initial impact velocity and v_o is the final velocity. The magnitude of E_{hc} will depend on the velocity only when the cellular solid has significant strain rate dependence. In such a case, the second order equation for evaluating BFS at a given velocity will need an additional velocity dependent first order term. As a result, the BFS versus velocity curve will have a different trend than that of the baseline. If the cellular solid is strain rate independent, E_{hc} will be of a constant magnitude and its addition will not change the curve's trend but its intercept, translating it parallel to the original baseline curve. The revised constants in the second order polynomial equation are given by the expression:

$$A = \frac{1.6731m}{D^2}, \qquad B = \frac{3.346\ a\ AD}{D^2}, \qquad C = \frac{3.346}{D^2}[E_{bd} + E_{hc} + b\ AD] \tag{A1.13}$$

It is to be noted that the semi-empirical relations derived here are of a phenomenological nature and do not provide explanation for the ballistic results but serve as an instrument to predict BFS values for the inserts. The relations in Equation A1.8b and A1.13 are optimal for use for practical projectile impact scenarios on baseline and HCA-P2 laminates.

Analytical model for BFS prediction:

An analytical model based on energy and momentum conservation was developed by Nguyen *et al.* [77] to describe the two-stage perforation process in thick Dyneema® laminates under FSP impact. This model estimated the energy absorbed in the first stage by characterizing it in terms of work required to produce a shear plug in the target

material. Similarly, energy absorbed in the second stage was characterized by momentum transfer and classical yarn theory for membrane tension. The model was found to provide a good agreement with experimental results from FSP tests on thick plates that demonstrated the two stage perforation process.

For the first stage, the energy to perforate the target material around the projectile perimeter is equated to the work required to produce the shear plug, where the shear area is the product of the projectile strike face circumference and the target thickness perforated in this stage. This is given by:

$$E_{pd1} = \tau_{max}\pi\, r\, {t_s}^2 = \tau_{max}\pi\, r \left(\frac{AD_1}{\rho_t}\right)^2 \quad \text{(A1.14)}$$

where, r is the projectile radius in m corresponding to initial strike face area S_1, t_s is the target thickness in m corresponding to the stage 1 areal density AD_1, ρ_t is the target material density in kg/m^3 and τ_{max} is the effective through-thickness shear strength of the laminate. It is assumed during this process there is no forward momentum transfer to the plug and plug material is considered to be ejected from the target front face. Energies associated with fiber tension and compression, delamination, fiber-matrix debonding and shock induced heating are ignored.

For the bulging stage, the target laminate is treated as a membrane with dominant failure mode considered as fiber tension. Individual plies are considered to have minimal bending resistance. Nguyen *et al.* [77] combined conservation of momentum with classical yarn theory for wave propagation to derive an expression for the projectile

velocity just before breakout to bulging. It was then used in the kinetic energy equation to get energy absorbed during bulging stage given by:

$$E_{pd2} = \frac{1}{2} m \left(1 + \frac{\beta^2 A D_2 S_2}{m}\right)^2 k_2 \tag{A1.15}$$

where, m is the projectile mass in kg. AD_2 and S_2 are identical to those used in the semi-empirical model described earlier and used here in SI metric units. β is the non-dimensional multiplier for projectile radius that accounts for the fact that the initial momentum transfer to the target just after breakout occurs over a radius larger than the projectile radius. k_2 is a material related constant that accounts for strain energy by tensile failure in load carrying longitudinal fibers in the cross-ply layup. It is given by:

$$k_2 = \frac{E_f}{\rho_f} \frac{v_f}{2} \left(2\varepsilon_{max}\sqrt{\varepsilon_{max} + {\varepsilon_{max}}^2} - {\varepsilon_{max}}^2\right) \tag{A1.16}$$

where, E_f is the fiber modulus for the target composite, ρ_f is the fiber density in kg/m^3, v_f is the fiber volume fraction in the composite and ε_{max} is the fiber failure strain. Energy absorbed by the composite can now be found similar to that in equation A1.3, by summation of equation A1.14, A1.15 and E_{bd}. BFS can then be estimated using the same scheme described in the semi-empirical model. The process to incorporate the energy absorption by the honeycomb is identical as well. The relation is again a second order polynomial of variable velocity (V).

Calculations for preliminary experimental results:

Experimental BFS results from the preliminary ballistic test for the baseline HB50 laminate of areal density 15.2 kg/m^2 were correlated to the predictions made using the semi-empirical and analytical model described here. A summary of calculations for all the significant terms required in the semi-empirical model are shown in Table 28. Average impact zone diameter size has been directly recorded from the clay backing during the preliminary test. The linear function for the ratio R was derived from the data presented in Figure 11 from the V_{50} tests on baseline inserts. It was observed that the material constant k_1 played a significant role in the analysis. Initial value was chosen as 1.42 from the slope of the energy absorbed per stage per unit strike face area versus areal density plot shown in Figure 38. This over-estimated the energy absorbed by the composite by a significant margin. This could be attributed to: (a) impacting projectile shape effects on the laminate as penetration potential of FSPs with a blunt strike face is different than ogival shaped 7.62 NATO Ball, (b) tests used to collect the data were performed with bolted edge constraints and no clay backing which are significantly

different boundary conditions than a NIJ level III ballistic test. Selecting a lower k_1 value of 0.97 provides a good correlation with the experimental data.

Table 28 Estimation of BFS for HB50 baseline using semi-empirical model and comparison with experimental values.

Description	Value			
Projectile mass	9.8 g			
Total areal density (*AD*) of HB50 laminate	15.2 kg/m^2			
Initial strike face (S_1) [22]	65 mm^2			
Deformed strike face (S_2) [22]	200 mm^2			
Energy absorbed in bullet deformation (E_{bd}) [22]	250 J			
Diameter of the impact zone, *D* (cm)	8.65			
Impact zone size (cm^2)	58.76			
Material constant for HB50 (k_1) [22]	0.97			
Projectile velocity (m/s)	780	788	804	812
Projectile kinetic energy, $E_{K.E}$ (J)	2981.2	3042.6	3167.4	3230.8
Penetration ratio for areal density, *R*	0.4628	0.4657	0.4714	0.4743
Areal density in shear, AD_1 (kg/m^2)	7.03	7.08	7.17	7.21
Areal density in bulging, AD_2 (kg/m^2)	8.17	8.12	8.03	7.99
Energy absorbed by composite in shear, Epd_1 (J)	443.5	446.3	451.8	454.6
Energy absorbed by composite in bulging, Epd_2 (J)	1584.1	1575.6	1558.6	1550.1
Energy absorbed by the composite, *Epd* (J)	2277.6	2271.9	2260.4	2254.7
$E_{back} = E_{K.E} - E_{pd}$ (J)	703.5	770.7	907.0	976.1
Calculated BFS (mm)	31.5	34.5	40.6	43.7
Actual BFS from experiments (mm)	33.0	35.0	42.4	45.3

Similarly, pertinent calculations for the analytical model are presented in Table 29. Material property values required to calculate constant k_2 were taken from [77]. Values for other parameters in the calculation are the same as those used in the semi-empirical model.

Table 29 Estimation of BFS for HB50 baseline using analytical model and comparison with experimental values.

Description	Value			
Projectile mass	9.8 g			
Total areal density (*AD*) of HB50 laminate	15.2 kg/m^2			
Initial strike face (S_1) [22]	65 mm^2			
Deformed strike face (S_2) [22]	200 mm^2			
Energy absorbed in bullet deformation (E_{bd}) [22]	250 J			
Diameter of the impact zone, *D* (cm)	8.65			
Impact zone size (cm^2)	58.76			
Total areal density (*AD*) of HB50 laminate	15.2 kg/m^2			
Material constant for HB50 (k_2) [77]	297.72 kJ/kg			
Projectile velocity (m/s)	780	788	804	812
Projectile kinetic energy, $E_{K.E}$ (J)	2981.2	3042.6	3167.4	3230.8
Penetration ratio for areal density, *R*	0.4628	0.4657	0.4714	0.4743
Areal density in shear, AD_1 (kg/m^2)	7.03	7.08	7.17	7.21
Areal density in bulging, AD_2 (kg/m^2)	8.17	8.12	8.03	7.99
Energy absorbed by composite in shear, Epd_1 (J)	411.5	416.7	427.1	432.3
Energy absorbed by composite in bulging, Epd_2 (J)	1614.5	1612.8	1609.5	1607.9
Energy absorbed by the composite, *Epd* (J)	2276.0	2279.5	2286.5	2290.1
$E_{back} = E_{K.E} - E_{pd}$ (J)	705.2	763.2	880.9	940.6
Calculated BFS (mm)	31.5	34.1	39.4	42.1
Actual BFS from experiments (mm)	33.0	35.0	42.4	45.3

Strain rate effects for the aluminum honeycomb in HCA-P2 have been neglected. The average energy absorption capacity for aluminum honeycomb is 6.5 MJ/m^3. The average face area of the honeycomb undergoing compression during impact was 35.4 cm^2. Substituting these values in equation A1.10 gives E_{hc} = 184 J. The resulting semi-empirical and analytical data curves correlates well with the experimental data points as shown in Figure 7.

Appendix 2A:

Summary of ballistic test results for V_{50} evaluation of HCA-P2 variants

Armor type	Shot number	Velocity (ft/s)	Velocity (m/s)	Penetration probability	V_{50} (m/s)
Baseline Var1	1	3157	962	1	952
	2	3032	924	0	
	3	3090	942	0	
	4	3156	962	1	
HCA-P2 Var1 insert 1	1	2997	913	0	983
	2	3131	954	0	
	3	3200	975	0	
	4	3325	1013	1	
	5	3250	990	1	
HCA-P2 Var1 insert 2	1	2959	902	0	995
	2	3360	1024	1	
	3	3272	997	0	
	4	3316	1011	1	
	5	3261	994	1	
Baseline Var2	1	2756	840	0	868
	2	2994	913	1	
	3	2943	897	1	

	4	2908	886	1	
	5	2789	850	0	
HCA-P2 Var2 insert 1	1	2849	868	1	852
	2	2810	856	0	
	3	2831	863	1	
	4	2800	853	1	
HCA-P2 Var2 insert 2	1	2746	837	1	831
	2	2703	824	0	
	3	2713	827	0	
	4	2747	837	1	
Baseline Var3	1	2731	832	1	826
	2	2670	814	0	
	3	2720	829	1	
	4	2714	827	0	
HCA-P2 Var3 insert 1	1	2746	837	1	754
	2	2702	824	1	
	3	2625	800	1	
	4	2576	785	1	
	5	2519	768	1	
	6	2392	729	0	
	7	2429	740	0	
HCA-P2 Var3 insert 2	1	2742	836	1	774
	2	2688	819	1	
	3	2619	798	1	
	4	2495	760	0	
	5	2513	766	0	
	6	2565	782	1	

Appendix 2B:

Summary of test results for the HCA-P2 variants with level IIIA liners and the level III standard plate.

Armor Type	Velocity (ft/s)	Velocity (m/s)	BFS (mm)	Penetration probability	V_{50} (m/s)
HCA-P2 Variant-3 combination	2721	829	44	0	835
	2704	824	38	0	
	2731	832	43	0	
	2742	836	-	1	

	2797	853	-	1	
HCA-P2 Variant-2 combination, insert 1	2778	847	42	0	870
	2845	867	38	0	
	2852	869	34	0	
	2919	890	29	0	
	2965	904	41	0	
HCA-P2 Variant-2 combination, insert 2	2785	849	30	0	
	2783	848	33	0	
	2769	844	31	0	
	2776	846	-	1	
	2804	855	-	1	
Level III standard insert	2786	849	47	0	-
	2724	830	38	0	
	2538	774	48	0	
	2799	853	49	0	
	2799	853	43	0	
	2806	855	53	0	

Appendix 2C:

Summary of test results for Baseline inserts from Test 4

Armor type	Shot number	Velocity (m/s)	BFS (mm)	Temp deg F	Corrected BFS (mm)
Baseline Insert 1	1	830	43.0	90	50.2
	2	775	34.9	90	42.1
	3	805	40.9	90	48.1
	4	743	32.1	90	39.3
Baseline Insert 2	1	831	49.1	100	49.1
	2	663	34.5	98	36.4
	3	755	42.4	100	42.4
	4	768	44.5	100	44.5
Baseline Insert 3	1	668	38.2	100	38.2
	2	707	37.8	100	37.8
	3	822	46.1	100	46.1
	4	849	50.8	100	50.8
	5	669	35.8	100	35.8
Baseline Insert 4	1	734	46.1	103	42.7
	2	832	52.6	103	49.2

	3	767	46.5	100	46.5
	4	888	52.6	100	52.6

Summary of test results for HCA-P2 variant-1, variant-4 and variant-5 to verify effect of honeycomb thickness on ballistic performance from Test 4.

Armor type	Shot number	Velocity (m/s)	BFS (mm)	Temp deg F	Corrected BFS (mm)
HCA-P2 Variant 1 Insert 1	1	766	29.6	90	36.8
	2	718	24.8	90	32.0
	3	869	-	90	-
	4	738	24.1	90	31.3
	5	676	21.4	90	28.6
HCA-P2 Variant 1 Insert 2	1	860	-	100	-
	2	674	29.3	100	29.3
	3	758	33.2	100	33.2
	4	785	35.0	100	35.0
HCA-P2 Variant 4 Insert 1	1	863	-	100	-
	2	652	37.0	100	37.0
	3	740	43.9	100	43.9
	4	806	44.8	100	44.8
	5	832	47.3	100	47.3
HCA-P2 Variant 4 Insert 2	1	868	-	100	-
	2	700	37.8	100	37.8
	3	780	46.0	100	46.0
HCA-P2 Variant 4 Insert 3	1	711	40.1	100	40.1
	2	863	-	100	-
	3	781	42.5	100	42.5
HCA-P2 Variant 5 Insert 1	1	867	-	100	-
	2	607	17.2	100	17.2
	3	684	21.6	100	21.6
	4	766	25.6	100	25.6
	5	797	27.7	100	27.7
	6	724	21.1	100	21.1
HCA-P2 Variant 5 Insert 2	1	864	-	100	-
	2	630	19.0	100	19.0
	3	698	23.7	100	23.7
	4	767	26.5	100	26.5
	5	790	29.7	100	29.7

	6	830	30.3	100	32.0

Summary of test results for HCA-P2 variant-6, variant-7, and variant-8 to verify effect of honeycomb type and thickness on ballistic performance from Test 4.

Armor type	Shot number	Velocity (m/s)	BFS (mm)	Temp deg F	Corrected BFS (mm)
HCA-P2 Variant-6 Insert 1	1	735	36	100	36.0
	2	884	-	100	-
	3	773	36	100	38.7
	4	885	38.5	98	41.2
HCA-P2 Variant-6 Insert 2	1	720	33.3	100	33.3
	2	888	-	100	-
	3	787	32.6	98	34.5
	4	889	38.6	98	40.5
HCA-P2 Variant-7 Insert 1	1	725	36.8	98	38.7
	2	868	-	98	-
	3	785	38.6	98	40.5
	4	890	39.8	98	47.8
HCA-P2 Variant-7 Insert 2	1	728	38.5	97	41.2
	2	878	-	97	-
	3	773	35.2	97	42.9
	4	887	-	97	-
HCA-P2 Variant-8 Insert 1	1	725	29.1	100	29.1
	2	875	-	100	-
	3	782	31.2	100	31.2
	4	891	33.9	98	35.8
HCA-P2 Variant-8 Insert 2	1	723	32.8	102	30.6
	2	878	-	102	-
	3	751	33.8	102	31.6
	4	889	-	102	-

Appendix 3

Drop weight tests for clay calibration and BFS correction factors.

NIJ 0101.06 standard mandates testing of armor for BFS measurements using Roma Plastilina® #1 clay backing that is calibrated using a drop weight test. This calibration test is used to condition the clay at a specific temperature that results in an average depth of penetration of 19 mm ± 2 mm from a steel sphere drop at 2 meters. This steel sphere must weigh 1.043 kg and have a diameter of 63.5 mm ± 0.05 mm. As clay is a viscoplastic material, calibration is mandatory to ensure standardized test process for BFS measurement and enables effective comparison between tested inserts. Data for change depth of penetration with temperature during this standard drop test has been presented [68, 96].

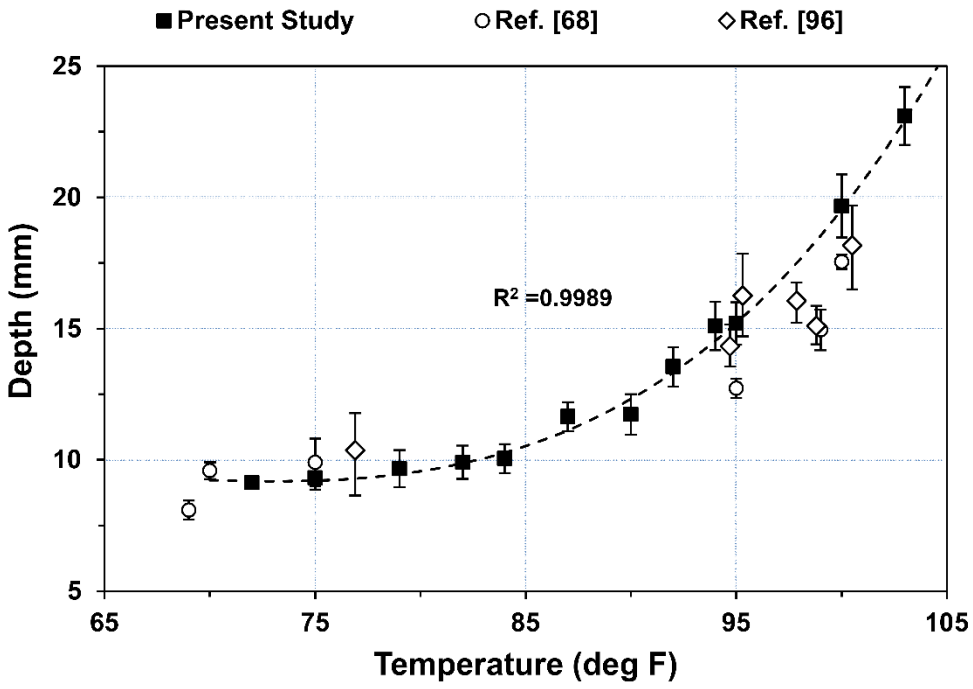

Figure 40 Plot for depth measured in clay versus its temperature from the calibration test as per NIJ 0101.06 standard. Similar data from cited references is included in the plot. Clay backing used in the present study meets the stated minimum depth criterion at 100° F.

A similar experiment was conducted to validate behavior of the clay backing used in present study. Results from the experiment are shown in Figure 40. Data from present experiment correlates well with that from the cited references. The plot indicates clay backing used in present study must be at 38°C (100°F) to meet the specified depth of penetration criterion. As found in [96], approximately 60 minutes span is available to conduct a ballistic test with the clay retaining calibration. Reduced BFS will be observed beyond this time frame. During Test 4, clay backing temperature for some inserts varied a few degrees above and below the stipulated temperature. BFS readings for these cases could be corrected to the reference temperature of 38°C if a model was available to provide the necessary corrections. Factors that govern the depth of penetration in the clay backing are kinetic energy of the dropped weight, its shape attributes and the clay temperature. It may thus be possible to evaluate the model if the relation between depth of penetration at a constant kinetic energy versus temperature is known, similar to the calibration test, by using the same dropped weight at different drop heights for a longer test duration. This experiment was conducted in the present study by conducting the steel sphere drop test from an increased height of 3.5 meters. Results from the test are shown in Figure 40. Curve from the standard test is also included.

It is observed that increase in kinetic energy causes the depth versus temperature curve to translate parallel to the original curve retaining a similar trend. Change in the kinetic energy of impact does not appear to affect the difference between depth of penetration values measured at two given temperatures. This is valid only when the impacting mass and its shape stay constant. This criterion is met if an insert is shot at a specific velocity at two different temperatures, where its average BFS diameter is fairly

constant as seen experimentally in this study. Depth differences between the two specific temperatures can then be considered as the required correction factors (within 10% error margin). They are listed in

Table 30.

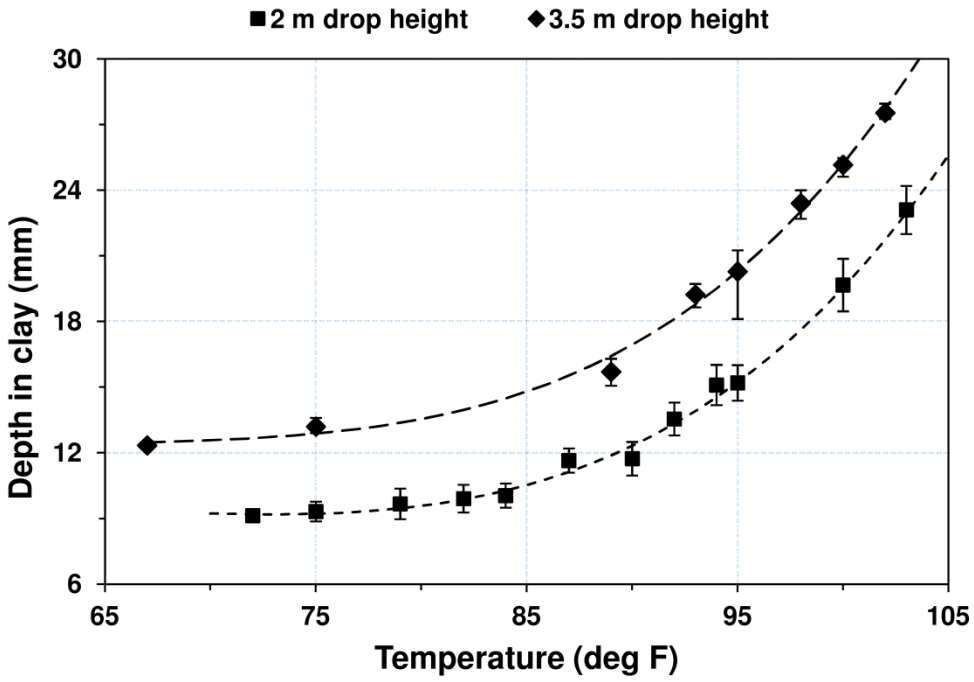

Figure 41 Drop weight calibration test conducted from different drop heights. Increase in kinetic energy appears to translate the parent curve parallel to the original trend.

Table 30 Depth difference as correction factors for BFS.

Temp F	Depth (mm)	Difference
90	12.3	7.2
97	16.8	2.7
98	17.6	1.9
99	18.5	1.0
100	19.5	0.0
101	20.6	-1.1
102	21.7	-2.2
103	22.9	-3.4

Figure 42 indicates BFS versus velocity plot for baseline insert 1 from Test 4 before (at 90°F) and after correction (at 100°F). Post corrected insert 1 data agrees well with the rest of the baseline inserts tested at the reference temperature.

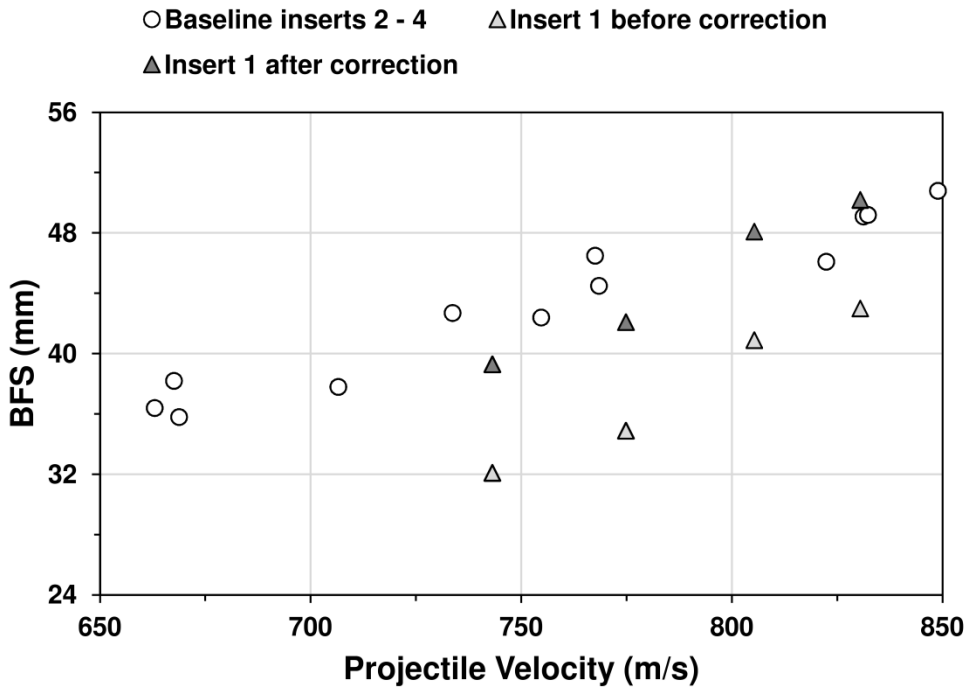

Figure 42 BFS versus velocity plot for baseline inserts from Test 4. Correction factors derived here are applied to baseline insert 1. Observed change is shown on the plot.

Appendix 4

Measurements from water-jet cut vertical cross-sections of tested inserts.

t_s: Thickness of front HB50 laminate undergoing shear plugging

t: Total thickness of HB50

S_2: Diameter of the deformed projectile in bulging stage

h_{cd}: Diameter of the honeycomb undergoing crushing and shear on impact

t_s/t: denoted by ratio R in the semi-empirical and analytical model and represents the transition from shear plugging to bulging.

Armor type	Shot#	Velocity	t	ts	S2	hc d	ts/t
Test 1 Baseline Insert 1	1	780	17	7.02	14.1	-	0.41
	2	804	17	7.11	16.76	-	0.42
	3	812	17	7.3	14.47	-	0.43
	4	788	17	7.16	15.58	-	0.42
Test 1 Baseline Insert 2	1	803	17	5.96	19.38	-	0.35
	2	792	17	5.12	21.96	-	0.30
	3	799	17	6.61	17.71	-	0.39
	4	811	17	6.82	19.54	-	0.40
Test 1 HCA-P2 Insert 1	1	810	17	6.83	18.89	65.4	0.40
	2	807	17	7.22	14.98	61.7	0.42
	3	804	17	6.78	19.2	68.3	0.40
	4	804	17	7.14	16.4	63.4	0.42
Test 1 HCA-P2 Insert 2	1	803	17	7.02	15.81	69.2	0.41
	2	814	17	6.76	14.66	63.7	0.40
	3	822	17	7.55	17.62	69.3	0.44
	4	799	17	6.78	16.14	66.2	0.40

Armor type	Shot#	Velocity	t	ts	S2	hc d	ts/t
Test 2 Baseline Variant 1	1	962	20	10.76	16.83	-	0.54
	2	924	20	9.81	12.49	-	0.49
	3	942	20	10.13	14.67	-	0.51
	4	962	20	10.67	14.92	-	0.53
Test 2 Baseline Variant 2	1	840	15.5	7.16	15.07	-	0.46
	2	913	15.5	8.37	13.52	-	0.54
	3	897	15.5	8.12	13.05	-	0.52
	4	886	15.5	7.85	14.28	-	0.51
	5	850	15.5	7.18	11.79	-	0.46
Test 2 Baseline Variant 3	1	832	14	7.02	11.58	-	0.50
	2	814	14	6.13	13.93	-	0.44
	3	829	14	6.86	12.57	-	0.49
	4	827	14	6.71	14.98	-	0.48

Armor type	Shot#	Velocity	t	ts	S2	hc d	ts/t
HCA-P2 Variant 1 Insert 1	1	766	16	6.69	18.68	60.1	0.42

	2	718	16	6.11	19.13	57.29	0.38
	3	822	16	7.35	17.63	47.14	0.46
	4	738	16	6.53	15.86	46.4	0.41
	5	676	16	6.03	16.86	55	0.38
HCA-P2 Variant 1 Insert 2	1	860	16	10.42	12.36	49.53	0.65
	2	674	16	6.79	16.1	50.56	0.42
	3	758	16	8.26	22.8	60.03	0.52
	4	785	16	8.42	16.84	57.79	0.53
HCA-P2 Variant 4 Insert 1	1	863	16	10.86	10.16	39.76	0.68
	2	652	16	7.62	15.75	51.68	0.48
	3	740	16	9.02	17.22	54.64	0.56
	4	806	16	9.36	17.77	57.5	0.59
	5	832	16	9.64	16.84	60.72	0.60
HCA-P2 Variant 4 Insert 2	1	868	16	11.42	14.9	50.67	0.71
	2	700	16	8.86	16.77	54.24	0.55
	3	780	16	10.25	17.27	59.42	0.64
HCA-P2 Variant 4 Insert 3	1	711	16	6.6	22.47	59.36	0.41
	2	863	16	9.98	17.49	58.22	0.62
	3	781	16	7.74	22.19	57.12	0.48
HCA-P2 Variant 5 Insert 1	1	867	16	10.24	10.1	51.58	0.64
	2	607	16	6.45	20.34	60.86	0.40
	3	684	16	7.81	17.21	61.38	0.49
	4	766	16	8.93	22.81	67.4	0.56
	5	797	16	9.04	16.95	60.03	0.57
	6	724	16	8.48	16.94	64.1	0.53
HCA-P2 Variant 5 Insert 2	1	864	16	10.73	9.4	44.95	0.67
	2	630	16	6.65	18.47	57.3	0.42
	3	698	16	7.92	22.4	60.47	0.50
	4	767	16	8.7	20.3	67.4	0.54
	5	790	16	8.98	17.4	61.32	0.56
	6	830	16	9.46	16.4	58.79	0.59

Armor type	**Shot#**	**Velocity**	**t**	**ts**	**S2**	**hc d**	**ts/t**
HCA-P2 Variant-6 Insert 2	1	720	16	6.56	20.1	63.34	0.41
	2	888	16	10.83	15.7	54.58	0.68
	3	787	16	8.23	18.86	61.12	0.51
	4	889	16	10.6	18.24	65.63	0.66
HCA-P2 Variant-7 Insert 1	1	725	16	7.96	20.16	63.08	0.50
	2	868	16	10.08	16.35	56.62	0.63
	3	785	16	8.65	17.26	60.02	0.54

	4	890	16	9.76	16.78	59.35	0.61
HCA-P2 Variant-8 Insert 1	1	725	16	7.62	18.79	62.95	0.48
	2	875	16	9.27	16.39	59.88	0.58
	3	782	16	8.41	23.73	62.2	0.53
	4	891	16	10.03	21	62.56	0.63

REFERENCES

[1] Ben-Dor G, Dubinsky A, Elperin T. Ballistic Impact: Recent Advances in Analytical Modeling of Plate Penetration Dynamics - A Review. Appl Mech Rev. 2005;58:355 - 71.

[2] Cheeseman BA, Bogetti TA. Ballistic impact into fabric and compliant composite laminates. Compos Struct. 2003;61:161 - 73.

[3] Tabiei A, Nilakantan G. Ballistic Impact of Dry Woven Fabric Composites: A Review. Appl Mech Rev. 2008;61:1 - 13.

[4] Qiao P, Yang M, Bobaru F. Impact Mechanics and High-Energy Absorbing Materials: Review. J Aerospace Eng. 2008;21:235 - 48.

[5] Alghamdi AAA. Collapsible impact energy absorbers: an overview. Thin Wall Struct. 2001;39:189-213.

[6] Cannon L. Behind Armour Blunt Trauma: an emerging problem. J R Army Med Corps. 2001;147:87 - 96.

[7] Dunn ES. U.S. Patent 5,349,893: Impact absorbing armor. Sep. 27, 1994.

[8] Senf H, Strassburger E, Rothenhausler H. Investigation of bulging during impact in composite armour. J Phys IV France. 1997;7:301 - 6.

[9] David NV, Gao XL, Zheng JQ. Ballistic resistant body armor: contemporary and prospective materials and related protection mechanisms. Appl Mech Rev. 2009;62:1 - 20.

[10] Bhat AR. Finite element modeling and dynamic impact response evaluation for ballistic applications. MS Thesis, Department of Mechanical and Aerospace Engineering, Oklahoma State University, USA. 2009.

[11] Gibson LJ, Ashby MF. Cellular solids: structure and properties - second edition, Cambridge University Press, Cambridge, UK. 1999.

[12] Lu G, Yu T. Energy absorption of structures and materials. 2003.

[13] Hazell PJ. Ceramic armour: Design and defeat mechanisms, Argos Press, Canberra, Australia. 2006.

[14] Dunstan S, Volstad R. Flak jackets: 20th Century Military Body Armour, Osprey Publishing Ltd., London. 1984.

[15] Armellino RA. US Patent 3,971,072: Lightweight Armor and method of fabrication. July 27,1972.
[16] Machalaba NN, Perepelkin KE. Heterocyclic Aramide Fibers - Production principles, properties and application. Journ of Indust textiles. 2002;31:189 - 204.
[17] Cunniff PM, Auerbach MA, Vetter E, Sikkema DJ. High performance "M5" fiber for ballistics/structural composites. 23rd Army Sci Conf, Orlando, Florida. 2002.
[18] Grujicic M, Glomski PS, He T, Arakere G, Bell WC, Cheeseman BA. Material modeling and Ballistic-resistance analysis of Armor-grade composites reinforced with High-performance fibers. J Mater Eng Perform. 2009.
[19] Lee BL, Walsh TF, Won ST, Patts HM, Song JW, Mayer AH. Penetration Failure Mechanisms of Armor-Grade fiber composites under impact. Journ of Comp Matl. 2000;35:1605 - 33.
[20] Cheeseman BA, Bogetti TA. Ballistic impact into fabric and compliant composite laminates. Composite Structures. 2003;61:161 - 73.
[21] Grujicic M, Arakere G, He T, Bell WC, Cheeseman BA, Yen CF, et al. A ballistic material model for cross-plied unidirectional ultra-high molecular-weight polyethylene fiber-reinforced armor-grade composites. Matl Sci and Engg. 2008;498:231 - 41.
[22] Jacobs MJN, VanDingenen JLJ. Ballistic protection mechanisms in personal armour. J Mater Sci. 2001;36:3137 - 42.
[23] Morye SS, Hine PJ, Duckett RA, Carr DJ, Ward IM. A comparison of the properties of hot compacted gel-spun polyethylene fibre composites with conventional gel-spun polyethylene fibre composites. Composites Part A. 1999;30:649 - 60.
[24] Simmelink JAPM, Mencke JJ, Marissen R, Jacobs MJN. Int. Patent WO 2005/066401: Process for making high-performance polyethylene multifilament yarn. 2005.
[25] Jacobs MJN, Beugels JHM, Blauuw M. U.S. Patent 2007/0164474 A1: Process for the manufacture of a ballistic-resistant moulded article. July 19, 2007.
[26] DSM Dyneema LP177 HB50 Brochure.
[27] Grogan J, Tekalur SA, Shukla A, Bogdanovich A, Coffelt RA. Ballistic resistance of 2D and 3D woven sandwich composites (vol 9, pg 283, 2007). Journal of Sandwich Structures & Materials. 2007;9:597-.
[28] Decker MJ, Halbach CJ, Nam CH, Wagner NJ, Wetzel ED. Stab resistance of shear thickening fluid (STF)-treated fabrics. Composites Science and Technology. 2007;67:565-78.
[29] Roberson C. Ceramic materials and their use in lightweight armour systems. Proceedings of Lightweight Armour systems symposium, Shrivenham, UK. 1995:28 - 30.
[30] Bart RK, Lindberg JC. Ceramic bodygaurds. Adv Matl and Processes inc Metal Progress. 1987;9:69 - 72.

[31] Medvedovski E. Ballistic performance of armour ceramics: Influence of design and structure. Part 1. Ceram Int. 2010;36:2103 - 15.
[32] Medvedovski E. Ballistic performance of armour ceramics: Influence of design and structure. Part 2. Ceram Int. 2010;36:2117 - 27.
[33] Karandikar PG, Evans G, Wong S, Aghajanian MK, Sennett M. A Review of Ceramics for Armor Applications. Ceram Eng Sci Proc, Daytona Beach, January. 2008;29.
[34] Mahfuz H, Zhu Y, Haque A, Abutalib A, Vaidya U, Jeelani S, et al. Investigation of high-velocity impact on integral armor using finite element method. Int J Impact Eng. 2000;24:203 - 17.
[35] Zaera R, Sanchez-Saez S, Perez-Castellanos JL, Navarro C. Modelling of the adhesive layer in mixed ceramic/metal armours subjected to impact. Compos Part A-Appl S. 2000;31:823 - 33.
[36] Fawaz Z, Zheng W, Behdinan K. Numerical simulation of normal and oblique ballistic impact on ceramic composite armours. Compos Struct. 2004;63:387 - 95.
[37] Dunn AG. U.S. Patent 4,483,020: Projectile proof vest. Nov. 20, 1984.
[38] Grujicic M, Pandurangan B, Zecevic U, Koudela KL, Cheeseman BA. Ballistic performance of Alumina/S-2 glass-reinforced polymer-matrix composite hybrid lightweight armor againt Armor Piercing (AP) and non -AP projectiles. Multidisc Model Mater Struct. 2006.
[39] Alavi Nia A, Razavi SB, Majzoobi GH. Ballistic limit determination of aluminum honeycombs - experimental study. Mater Sci Eng. 2008;488:273 - 80.
[40] Johnson GR, Cook WH. A constitutive model and data for metals subjected to large strains, high strain rates and high temperatures. Proceedings - 7th Int Symp on Ballistics, Hague, Netherlands. April 1983:541 - 7.
[41] Camacho GT, Ortiz M. Adaptive Lagrangian modelling of ballistic penetration of metallic targets. Comput Method Appl M. 1997;142:269 - 301.
[42] Johnson GR, Cook WH. Fracture characteristics of three metals subjected to various strains, strain rates, temperatures and pressures. Eng Fract Mech. 1985;21:31 - 48.
[43] Chocron S, Anderson Jr CE, Grosch DJ, Popelar CH. Impact of the 7.62-mm APM2 projectile against the edge of a metallic target. Int J Impact Eng. 2001;25:423 - 37.
[44] Buchar J, Voldrich J, Rolc S, Lisy J. Ballistic performance of dual hardness armor. Proceedings of 20th International symposium on ballistics, September, Orlando. 2002:23 - 7.
[45] Preece DS, Berg VS. Bullet impact on steel and kevlar/steel armor - computer modeling and experimental data. Proceedings of the ASME pressure vessels and piping conference - Symposium on structures under extreme loading, July 25-29, San Diego, CA. 2004.
[46] Anderson Jr CE, Burkins MS, Walker JD, Gooch WA. Time-resolved penetration of B4C tiles by the APM2 bullet. CMES. 2005;8:91-104.

[47] Hazell PJ, Edwards MR, Longstaff H, Erskine J. Penetration of a glass-faced transparent elastomeric resin by a lead-antimony-cored bullet. Int J Impact Eng. 2009;36:147 - 53.
[48] Borvik T, Dey S, Clausen AH. Perforation resistance of five high-strength steel plates subjected to small-arms projectiles. Int J Impact Eng. 2009;36:948 - 64.
[49] Niezgoda T, Morka A. On the numerical methods and physics of perforation in the high-velocity impact mechanics. World J Eng.414 - 6.
[50] Krishnan K, Sockalingam S, Bansal S, Rajan SD. Numerical simulation of ceramic composite armor subjected to ballistic impact. Compos Part B. 2010;41:583 - 93.
[51] Burger D, Rocha de Faria A, F.M. de Almeida S, C.L. de Melo F. Ballistic impact simulation of an armour-piercing projectile on hybrid ceramic/fiber reinforced composite armours. Int J Impact Eng. 2012;43:63-77.
[52] Kilic N, Ekici B. Ballistic resistance of high hardness armor steels against 7.62 mm armor piercing ammunition. Mater Des. 2013;44:35 - 48.
[53] Nsiampa N, Dyckmans G, Chabotier A. Impact of 7.62 AP ammunition into Aluminum 5083 plates. Proceedings of the 23rd International symposium on ballistics, 16-26 April, Tarragona, Spain. 2007.
[54] Schwer LE, Hacker K, Peo K. Perforation of metal plates: laboratory experiments and numerical simulations. Proceedings - 2nd Int Conf DAPS, Singapore. Nov 2006:13 -4.
[55] Kurtaran H, Buyuk M, Eskandarian A. Ballistic impact simulation of GT model vehicle door using finite element method. Theo and Appl Frac Mech. 2003;40:113 - 21.
[56] Borvik T, Langseth M, Hopperstad OS, Malo KA. Perforation of 12 mm thick steel plates by 20 mm diameter projectiles with flat, hemispherical and conical noses Part II: numerical simulations. Int J Impact Eng. 2002;27:37 - 64.
[57] Arias A, Rodriguez-Martinez JA, Rusinek A. Numerical simulations of impact behaviour of thin steel plates subjected to cylindrical, conical and hemispherical non-deformable projectiles. Eng Fract Mech. 2008;75:1635 - 56.
[58] Johnson GR, Holmquist TJ. An improved computational constitutive model for brittle materials. High Pressure Science and Technology - 1993, New York, AIP Press. 1993.
[59] Cronin DS, Bui K, Kaufmann C, McIntosh G, Berstad T. Implementation and validation of the Johnson-Holmquist ceramic material model in LS-Dyna. Proceedings of the 4th European LS-DYNA Users Conference - Material I, May 2003, Ulm, Germany. 2003:47 - 60.
[60] Ochoa OO, Reddy JN. Finite element analysis of composite laminates, Solid Mechanics and its Applications, Kluwer Academic Publishers, Boston, USA. 1992;7.

[61] Hashin Z. Failure criteria for unidirectional composites. J Appl Mech. 1980;47:329 - 34.
[62] Soldani X, Santiuste C, Cantero JL, Miguelez MH. Numerical modeling of delamination during machining of LFRP composites. Proceedings of 18th International Conference on Composite Materials, July 27-31, Edinburgh, Scotland. 2009:1 - 5.
[63] Hou JP, Petrinic N, Ruiz C, Hallet SR. Prediction of impact damage in composite plates. Compos Sci Tech. 2000;60:273 - 81.
[64] Chang F, Chang K. A progressive damage model for laminated composites containing stress concentrations. J Compos Mater. 1987;21:834 - 55.
[65] Perillo G, Vedvik N, Echtermeyer AT. Numerical analyses of low velocity impacts on composite. Advanced modelling techniques. Proceedings of the 2012 SIMULIA Community Conference, May 15-17, Providence, Rhode Island, USA. 2012:1 - 16.
[66] Cooper G, Gotts P. Ballistic trauma: a practical guide, Chapter 4: Ballistic Protection. Second Edition, Springer - Verlag London Limited. 2005:67 - 90
[67] Prather R, Swann C, Hawkins C. Backface signatures of soft body armors and the associated trauma effects. ARCSL-TR-77055 Aberdeen Proving Ground, Md: Edgewood Arsenal. 1977.
[68] Testing of body armor materials: Phase III, National Academic Press, Washington D.C., USA. 2012.
[69] Gryth D, Rocksen D, Persson J, Arborelius U, Drobin D, Bursell J, et al. Severe lung contusion and death after high-velocity behind-armor blunt trauma: Relation to protection level. Mil Med. 2007;172:1110 - 6.
[70] Bass CR, Salzar RS, Lucas SR, Davis M, Donnellan L, Folk B, et al. Injury risk in bhind armor blunt thoracic trauma. Int J Occup Saf Ergon. 2006;12:429 - 42.
[71] Viano DC, King AI. Biomechanics of chest and abdomen impact. The Biomedical Engineering Handbook: Second Edition, CRC Press LLC, Boca Raton. 2000.
[72] Prat N, Rongieras F, Sarron J-C. Contemporary body armor: technical data, injuries, and limits. Eur J Trauma Emerg Surg. 2012;38:95 - 105.
[73] Lee BL, Walsh TF, Won ST, Patts HM, Song JW, Mayer AH. Penetration Failure Mechanisms of Armor-Grade fiber composites under impact. J Compos Mater. 2000;35:1605 - 33.
[74] Bhat AR, Jayakumar B, Hanan JC. Ballistic investigation of a hybrid composite armor including an amorphous metal honeycomb layer. Compos Struct. 2015;*In Review*.
[75] Hanan JC. U.S. Patent Application 20120208041 A1: Teardrop lattice structure for high specific strength materials. Aug. 16, 2012.
[76] Bhat AR, Luo H, Mahadevan GR, Lu H, Hanan JC. Dynamic compressive behavior of Fe based amorphous metal honeycomb cellular structures. Bulk Metallic Glasses

VIII Symposium, TMS Annual Meeting and Exhibition Proceedings, San Diego, CA, USA. 2011.

[77] Nguyen L, Ryan S, Cimpoeru SJ, Mouritz AP, Orifici AC. The effect of target thickness on the ballistic performance of ultra high molecular weight polyethylene composite. Int J Impact Eng. 2015;75:174 - 83.

[78] Heisserer U, van der Werff H, Hendrix J. Ballistic depth of penetration studies in Dyneema ® composites. Proceedings of 27th International Symposium on Ballistics, Freiburg, Germany April 22-26. 2013:1936 - 43.

[79] Karthikeyan K, Russell BP, Fleck NA, Wadley HNG, Deshpande VS. The effect of shear strength on the ballistic response of laminated composite plates. Eur J Mech A-Solid. 2013;42:35-53.

[80] Gama BA, Bogetti TA, Fink BK, Yu C-J, Claar T, Eifert HH, et al. Aluminum foam integral armor: a new dimension in armor design. Compos Struct. 2001;52:381 - 95.

[81] Borvik T, Hopperstad OS, Berstad T, Langseth M. A computational model of viscoplasticity and ductile damage for impact and penetration. Eur J Mech A- Solid. 2001;20:685 - 712.

[82] Hazell PJ. Numerical simulations and experimental observations of the 5.56 mm L2A2 bullet perforating steel targets of two hardness values. J Battlefield Tech. 2003;6:1 - 4.

[83] Grujicic M, Arakere G, He T, Bell WC, Cheeseman BA, Yen CF, et al. A ballistic material model for cross-plied unidirectional ultra-high molecular-weight polyethylene fiber-reinforced armor-grade composites. Mater Sci Eng. 2008;498:231 - 41.

[84] ABAQUS – Version 6.9, User Documentation, Dassault Systems, 2010.

[85] Wierzbicki T, Bao Y, Lee Y, Bai Y. Calibration and evaluation of seven fracture models. Int J Mech Sci. 2005;47:719-43.

[86] Ivañez I, Santiuste C, Barbero E, Sanchez-Saez S. Numerical modelling of foam-cored sandwich plates under high-velocity impact. Composite Structures. 2011;93:2392 - 9.

[87] Karthikeyan K, Russell BP, Fleck NA, O'Masta M, Wadley HNG, Deshpande VS. The soft impact response of composite laminate beams. Int J Impact Eng. 2013;60:24 - 36.

[88] Lassig T, Nguyen L, May M, Riedel W, Heisserer U, van der Werff H, et al. A non-linear orthotropic hydrocode model for ultra-high molecular weight polyethylene in impact simulations. Int J Impact Eng. 2015;75:110 - 22.

[89] Russell BP, Karthikeyan K, Deshpande VS, Fleck NA. The high strain rate response of ultra high molecular-weight polyethylene: from fibre to laminate. Int J Impact Eng. 2013;60:1 - 9.

[90] Attwood JP, Khaderi SN, Karthikeyan K, Fleck NA, O'Masta M, Wadley HNG, et al. The out-of-plane compressive response of Dyneema composites. J Mech Phys Solids. 2014;70:200 - 26.
[91] Liu G, Thouless MD, Deshpande VS, Fleck NA. Collapse of a composite beam made from ultra high molecular-weight polyethylene fibers. J Mech Phys Solids. 2014;63:320 - 35.
[92] Aktay L, Johnson AF, Kroplin B-H. Numerical modeling of honeycomb core crush behaviour. Eng Fract Mech. 2008;75:2616 - 30.
[93] Dannemann KA, Lankford J. High strain rate compression of closed-cell aluminum foams. Mater Sci Eng. 2000;A293:157 - 64.
[94] Allen HG. Analysis and design of structural sandwich panels - first edition, Pergamon Press, UK. 1969.
[95] Koene B, Id-Boufker F, Papy A. Kinetic non-lethal weapons. Netherland Annual Review of Military Studies. 2008:9 - 24.
[96] Bhattacharjee D, Kumar A, Biswas I. Energy absorption and dynamic deformation of backing material for ballistic evaluation of body armor. Defence Sci J. 2013;63:462 - 6.

VITA

ADVAIT BHAT

Candidate for the Degree of

Doctor of Philosophy

Thesis: HONEYCOMB IN HYBRID COMPOSITE ARMOR RESISTING DYNAMIC IMPACT

Major Field: Mechanical and Aerospace Engineering

Biographical:

Education:

Completed the requirements for the Doctor of Philosophy in Mechanical and Aerospace Engineering at Oklahoma State University, Stillwater, Oklahoma in July, 2015.

Completed the requirements for the Master of Science in Mechanical and Aerospace Engineering at Oklahoma State University, Stillwater, Oklahoma in December, 2009.

Completed the requirements for the Bachelor of Engineering in Mechanical Engineering at University of Mumbai, Mumbai, India in 2007.

Experience:

Graduate Research Assistant (January 2008 - July 2015)
Research lab: Dr. Jay Hanan. Oklahoma State University

Graduate Teaching Assistant (January 2008 - December 2014)
Mechanical and Aerospace Engineering, Oklahoma State University.

Graduate Intern (May 2013 - August 2013)
MetCel LLC, Stillwater, Oklahoma.